INVERSE SEGREGATION AND CENTRELINE SHRINKAGE

by

SAKAE MINAKAWA

B.E., Tohoku University, Japan, 1977.

A THESIS SUBMITTED IN PARTIAL FULFILMENT OF

THE REQUIREMENTS FOR THE DEGREE OF

MASTER OF APPLIED SCIENCE

in

THE FACULTY OF GRADUATE STUDIES

Department of Metallurgical Engineering

We accept this thesis as conforming

to the required standard

THE UNIVERSITY OF BRITISH COLUMBIA

June 1984

In presenting this thesis in partial fulfilment of the requirements for an advanced degree at the University of British Columbia, I agree that the Library shall make it freely available for reference and study. I further agree that permission for extensive copying of this thesis for scholarly purposes may be granted by the Head of my Department or by his or her representatives. It is understood that copying or publication of this thesis for financial gain shall not be allowed without my written permission.

Department of Metallurgy

The University of British Columbia
2075 Wesbrook Place
Vancouver, Canada
V6T 1W5

Date: June 8, 1984

Abstract

One of the major factors controlling macrosegregation and shrinkage porosity in castings is the extent of interdendritic fluid flow which occurs during solidification. Interdendritic flow results from movement of liquid to fill the voids left by solidification and thermal shrinkage, which in the case of many alloys cast against a cold chill, results in inverse segregation. In the present investigation, inverse segregation has been examined theoretically. Quantitative values for the segregation both at and adjacent to the chill face have been determined using a mathematical model and computer calculations. The alloys considered were Al-Cu, Al-Zn and Sb-Bi, the latter being of particular significance since it expands during solidification. The model results show reasonable agreement with published data of chill face inverse segregation. In the previous models, the volume shrinkage used to calculate inverse segregation did not include the thermal contraction which, in the present model predictions, was found to have more significant role in the segregation than expected. The results from the present model differs significantly from those of the earlier models, particularly in the Al-Zn alloys.

Centreline shrinkage in a steel plate casting, associated with back flow of interdendritic liquid, was examined using the interdendritic fluid flow model combined with a heat transfer model of the system. Regions of the plate where centreline porosity should occur were predicted with the new model and compared to published experimental results of porosity in steel

plates. Excellent agreement was obtained between the predicted and experimental results. In the fluid flow model, Darcy's Law was used to determine the extent of flow in the interdendritic channels. The present results indicate Darcy's Law is valid in this application.

Table of Contents

List of Tables

List of Figures

List of Nomenclature

A	area,(cm^2)
a_E	eutectic contraction coefficient,*
Bi	Biot number,*
$\bar{C}$	mean composition of volume element,(wt%)
ΔC	amount of segregation,(wt%)
ΔC_{ij}	segregation formed during the solidification of element (i,j),(wt%)
ΔC_j	segregation in j-th column,(wt%)
C_L, C_s	compositions of liquid and solid, respectively,(wt%)
C_{LE}	composition of liquid at eutectic,(wt%)
$\Delta C_{L_{ij}}$	sum of the composition dilution effects in j-th column when i-th element solidifies,(wt%)
ΔC_{L_j}	total dilution of composition in j-th column,(wt%)
C_o	initial composition,(wt%)
C_p	specific heat,(cal/g°C)
$\bar{\bar{C}}_s$	local average composition of solid,(wt%)
C_{sE}	mean composition of cored solid at eutectic,(wt%)
D	length of plate casting,(cm)
DAS	primary dendrite arm spacing,(cm)
F	grey body shape factor,*
Fo	Fourier number,*
f_s, f_L	weight fraction solid and liquid,respectively,*
G	temperature gradient,(°C/cm)

g_E	volume fraction of eutectic,*
g_s, g_L	volume fraction of solid and liquid, respectively,*
g_r	acceleration due to gravity,981(cm/sec^2)
H_s	latent heat of solidification,(cal/g)
h	heat transfer coefficient,(cal/cm^{2}sec°C)
h_s, h_M	heat transfer coefficient from sand mold and metal to ambient air, respectively,(cal/cm^{2}sec°C)
K	permeability,(cm^2)
k	thermal conductivity,(cal/cm.sec°C)
k_a	thermal conductivity of air,(cal/cm.sec°C)
k_s, k_M	thermal conductivity of sand mold and metal, respectively,(cal/cm.sec°C)
k_0	equilibrium partition ratio,*
L	length of solid/liquid zone,(cm)
L_s	length of solid/liquid zone at steady state,(cm)
l	length of fluid flow,(cm)
l_f	capillary feeding distance,(cm)
m_s, m_L	solid and liquid masses, respectively, in a representative volume,(g)
m_{sE}, m_{LE}	m_s and m_L, respectively, at eutectic temperature,(g)
r	radius of capillary,(cm)
P	pressure,(dyn/cm^2)
P_a	ambient pressure,(dyn/cm^2)
ΔP	pressure drop due to fluid flow,(dyn/cm^2)
P_o	pressure acting due to capillary flow,(dyn/cm^2)

P_{II}	gradient of fraction solid,(1/cm)
q	heat flux,(cal/cm²sec)
R	cooling rate,(°C/sec)
s	thickness of plate casting or size of square bar casting,(cm)
T	temperature,(°C)
T*	temperature after Δt,(°C)
T_I , T_{II}	interface temperature of ingot and mold, respectively,(°C)
T_a	ambient temperature,(°C)
T_M , T_S	temperature in metal and sand mold, respectively,(°C)
T_o	initial temperature,(°C)
T_p	pouring temperature,(°C)
t	time,(sec)
V	representative volume or fluid volume to flow,(cm^3)
V_c/A_c	volume-to-area ratio of casting,(cm)
v	fluid flow velocity in a capillary,(cm/sec)
$\bar{v}$	local flow velocity of interdendritic liquid,(cm/sec)
v'	superficial flow velocity of interdendritic fluid,(cm/sec)
v_s	velocity of solidus,movement along the centerline of a plate casting,(cm/sec)
v_x	local flow velocity of interdendritic liquid in x-direction,(cm/sec)

$\Delta x, \Delta y$	element size,(cm)
Y	metallostatic head,(cm)
a	thermal diffusivity,(cm^2/sec)
β	solidification shrinkage ratio,*
δ	thickness of air gap,(cm)
ϵ	emissivity,*
μ	viscosity,(poise)
ν_L, ν_S	specific volume of liquid and solid, respectively,(cm^3/g)
ρ	density,(g/cm^3)
$\overline{\rho}$	local mean density of solid and liquid,(g/cm^3)
ρ_o	initial density of liquid,(g/cm^3)
ρ_L, ρ_S	density of liquid and solid, respectively,(g/cm^3)
σ	solid density of eutectic composition,(g/cm^3)
	1.37×10^{-12}($cal/cm^2 sec\,^\circ K^4$)
τ	tortuosity factor,*

Note: * is dimensionless

Acknowledgement

I wish to express my sincere gratitude to Prof. Fred Weinberg and Dr. Indira V. Samarasekera for their invaluable advice, guidance and immense encouragement throughout the course of this investigation.

Thanks are also extended to my fellow graduate students for their voluntary assistance and co-operation. The assistance of faculty members in the Department of Metallurgical Engineering, University of British Columbia is greatly appreciated.

I am grateful to RIKEN Corporation, Tokyo, Japan, for providing me with this opportunity and financial support.

I will not be doing justice to myself without acknowledging hard time and sacrifices which my wife, Yuko, and my daughter, Momoko, had to stand during the course of the present study.

PART - A

INVERSE SEGREGATION IN BINARY ALLOYS

A-I. INTRODUCTION AND LITERATURE REVIEW

1.1 Introduction

During the long industrial history of foundry technology, the casting process has been considered from an empirical point of view rather than theoretically. This can be attributed to the complexity of the casting process which has discouraged basic investigations of the process. For example, the solidification of multiphase systems is heterogeneous, and occurs under unsteady state and non-equilibrium conditions. During solidification of simple binary alloys, solid of one composition forms from liquid of another composition. This occurrence makes it impossible to cast homogeneous alloys with uniform structure and properties. Recently mathematical modelling of the solidification process has enabled calculations to be made which give the temperature distribution in the solid and liquid during non-equilibrium solidification. With computers, these calculations can be done reasonably, quickly and cheaply. The results of the calculation have been shown to agree well with the corresponding temperature measurements in laboratory experiments and in industrial situations.

The major defects in castings are macrosegregation and shrinkage. Both have a very strong influence on the quality of the castings. It is generally recognized that these defects are

largely related to fluid flow during solidification, particularly interdendritic flow resulting from solidification and thermal shrinkage.

The occurence of inverse segregation, in which the solute gradient distribution is opposite to that predicted by the equilibrium phase diagram during solidification, has long interested metallurgists. Inverse segregation has been examined by a number of researchers. It is generally accepted that this type of segregation is due to the back flow of solute rich interdendritic liquid to fill the void created by solidification and thermal contractions during solidification.

1.2 Previous Models for Chill Face Inverse Segregation

Scheil was the first person to derive precise analytical expressions for the amount of inverse segregation which occurs at the chill face during solidification. For a typical binary eutectic alloy system, the segregation (ΔC) is given by:

$$\Delta C = \overline{C} - C_o \tag{A-1}$$

with

$$\overline{C} = \frac{\frac{m_{LE}C_{LE}}{a_E} + m_{SE}C_{SE}}{\frac{m_{LE}}{a_E} + m_{SE}} \tag{A-2}$$

Kirkaldy and Youdelis[2] extended the Scheil equation (A-2)

to determine the solute concentration profile both at the chill face and in the body of the metal as a function of distance from the chill face for a unidirectionally solidified ingot. A representative volume, V, is related to mass and specific volumes of liquid and solid as:

$$V = \nu_S m_S + \nu_L m_L \tag{A-3}$$

On the assumption that no contraction void forms, and that V is constant, equation (A-3) reduces to,

$$dm_L = - a\, dm_S \tag{A-4}$$

where

$$a = \frac{\nu_S}{\nu_L} + \frac{m_L}{\nu_L}\frac{d\nu_L}{dm_S} \tag{A-5}$$

The solute mass balance for incremental solidification in the volume is given by:

$$d(m_L C_L) = -C_S dm_S + \left\{ C_L dm_S \left(\frac{\nu_L - \nu_S}{\nu_L}\right) - C_L m_L \frac{d\nu_L}{\nu_L} \right\} \tag{A-6}$$

where the change of solute mass in the liquid is equated to the change of solute mass in the solid plus the solute mass transported into the volume by contraction. The contraction contribution is made up of two terms: contraction due to the solid/liquid phase change, and contraction due to the specific volume change of the liquid. Note that thermal contraction is neglected in this model. Combining equations (A-4) to (A-6) gives the basic differential equation;

$$\frac{dm_L}{m_L} = - a \frac{dC_L}{AC_L} \tag{A-7}$$

where

$$A = 1 - \frac{C_S}{C_L} \tag{A-8}$$

The integration of equation (A-7) gives m_L which when substituted into equation (A-4) gives a value for m_s. The change of the mass in a cored crystal is related to that in the remaining liquid as:

$$d(m_S C_S) = C_S dm_S \tag{A-9}$$

Combining equations (A-4) and (A-7) with equation (A-9) yields:

$$d(m_S C_S) = \frac{1-A}{A} m_L dC_L \tag{A-10}$$

Accordingly, the substitution of $m_s C_s$, calculated by the integration of equation (A-10), together with m_L and m_s into equation (A-2) will give the maximum inverse segregation at the chill face.

For the Al-Cu system, the temperature dependence of the specific volumes of the solid and liquid under equilibrium conditions were compiled by Sauerwald[3]. These values are shown in Fig 1 along with constitutional phase diagram of the alloy. Using this data, Scheil[1] calculated the maximum segregation at the chill face for a unidirectionally solidified ingot. The calculated values were found to be in excellent agreement with measured values of the solute concentration at the chill face over the entire composition range examined.

The above theory was also applied to the Al-Zn and Sb-Bi alloys by Youdelis et al[4,5] using the specific volume data reported by Prezel and Schneider[6]. Again the theoretical values

of the chill face concentration agreed well with the experimental measurements. In the Al-Zn alloy the scatter of the experimental data is large, making the comparison between theory and experiment less defined than in other systems. Of particular interest in comparing theory and experiment are the results for the Sb-Bi alloy. In this system solidification is accompanied by volume expansion at the high Bi concentrations and contraction at low Bi values. The change from positive to negative inverse segregation, corresponding to the transition from expansion to contraction, occurs at approximately 30%Bi.

In the Scheil and Youdelis development of the mathematical formulation of inverse segregation, the following assumptions were made.

1) The specific volume and composition of the primary solidified metal are constant.
2) The thermal contraction during solidification is negligible.

These assumptions are invalid or only approximately valid for the following reasons. The model is only applicable to systems with negligible solid solubility to comply with assumption (1) and for alloys with short freezing ranges to comply with assumption (2). Note that, with complete coring in the solid, the final solidification occurs at the eutectic temperature, not at the solidus temperature.

1.3 Inverse Segregation away from the Chill Face (positional Segregation)

Assuming linear mass distribution of liquid in the solid/liquid mushy zone, and a specific gradient of liquid composition in the direction of solidification, Kirkaldy and Youdelis[2] have extended Scheil's analysis to the calculation of the positional variation of inverse segregation.

At the chill face, during solidification, interdendritic liquid flows into the elemental volume with no outward flow. Away from the chill face interdendritic liquid flows both into and out of the elemental volume to take up volume change. To account for the outward fluid flow the equation for the solute mass balance, equation (A-6), must be rewritten by adding a term due to liquid flow out at the position L:

$$d(m_L C_L) = - C_S dm_S + \left\{ C_L dm_S \left(\frac{\nu_L - \nu_S}{\nu_L} \right) - C_L m_L \frac{d\nu_L}{\nu_L} \right\} - m_L \frac{\partial C'_L}{\partial L} dS \qquad \text{(A-11)}$$

where $\partial C'_L / \partial L$ is the mean liquid concentration gradient and S is the inward flow distance past point L due to contraction in inner regions. Equation (A-6) was replaced with equation (A-11) and the positional segregation profiles for Al-10%Cu and Al-15%Cu were calculated in the similar manner to the calculation of the maximum segregation at the chill face as described in the previous section. With this theory, calculations of the positional segregation gave results which agreed well with

experimentally measured values of the segregation as a function of position from the chill face.

Prabhakar and Weinberg[7] questioned the conclusions arrived at by Kirkaldy and Youdelis[2] on the basis of the accuracy of their measurements. Prabhakar and Weinberg[7] carried out some careful inverse segregation measurements using radioactive tracer techniques and showed that the maximum inverse segregation at the chill face is highly dependent of casting conditions, including the superheat of the melt when cast. With superheat temperature greater than 40°C, the concentration at the chill face drops rapidly with increasing superheat for a copper chill. With a stainless steel chill which has a lower thermal conductivity than copper, the inverse segregation is higher at higher superheats when compared to the copper chill, but also drops with increased superheat. Moreover, there was no indication of inverse segregation in the region well away from the chill face as reported by Kirkadly and Youdelis[2]. These results indicate that various casting parameters, not included in the theoretical model, can strongly influence the extent of interdendritic fluid flow during solidification and accordingly, the inverse segregation.

Based on the concept that all solute macrosegregation results from interdendritic fluid flow of solute rich liquid to feed solidification shrinkage and thermal contraction, the Scheil-Youdelis model was extended by Flemings et al[8-11] to account for a wide range of segregation effects. This included

centerline segretation, banding, under-riser positive segregation, and the negative cone of segregation as well as inverse segregation. Conservation of solute mass in the volume element during solidification requires that:

$$\frac{\partial}{\partial t}(\bar{\rho}\bar{C}) = -\nabla(\rho_L g_L C_L \vec{v}) \tag{A-12}$$

Conservation of total mass in the volume element gives,

$$\frac{\partial \bar{\rho}}{\partial t} = -\nabla(\rho_L g_L \vec{v}) \tag{A-13}$$

Combining equations (A-12) and (A-13),

$$\frac{\partial}{\partial t}(\bar{\rho}\,\bar{C}) = C_L \frac{\partial \bar{\rho}}{\partial t} - \rho_L g_L \vec{v}\,\nabla C_L \tag{A-14}$$

The change in solute mass of the volume element is the sum of the changes in the liquid and solid phases;

$$\frac{\partial}{\partial t}(\bar{\rho}\,\bar{C}) = \frac{\partial}{\partial t}(\bar{C}_S \rho_S g_S + C_L \rho_L g_L) \tag{A-15}$$

Similarly, the change in total mass of the volume element is,

$$\frac{\partial \rho}{\partial t} = \frac{\partial}{\partial t}(\rho_S g_S + \rho_L g_L) \tag{A-16}$$

Assuming local equilibrium at the solid/liquid interface, no diffusion in the solid, and a constant solid density, gives:

$$\frac{\partial}{\partial t}(\bar{C}_S \rho_S g_S) = k_o C_L \rho_S \frac{\partial g_S}{\partial t} \tag{A-17}$$

and

$$dg_S = -dg_L \tag{A-18}$$

Substituting equations (A-17) and (A-18) in equation (A-15), and combining it with equations (A-16) and (A-14) gives the final partial differential equation;

$$\frac{\partial g_L}{\partial C_L} = -\left(\frac{1-\beta}{1-k_o}\right)\left(1+\frac{\bar{v}\nabla T}{R}\right)\frac{g_L}{C_L} \tag{A-19}$$

For one dimensional problem, that is unidirectional

solidification, equation (A-19) is rewritten to:

$$\frac{\partial g_L}{\partial C_L} = -\left(\frac{1-\beta}{1-k_o}\right)\left(1+\frac{v_x G}{R}\right)\frac{g_L}{C_L} \qquad \text{(A-20)}$$

Macrosegregation is defined for a binary eutectic system as,

$$\bar{C} = \frac{\rho_S \int_o^{1-g_E} C_S \, \partial g_S + \rho_{SE} g_E C_{LE}}{\rho_S(1-g_E) + \rho_{SE} g_E} \qquad \text{(A-21)}$$

$$\Delta C = \bar{C} - C_o$$

which is analogous to Scheil's expression, equation (A-1) and (A-2). Macrosegregation can now be calculated with equation (A-21) and equation (A-19) or (A-20).

Two limiting cases can be easily studied. For steady state,

$$\frac{v_x G}{R} = \frac{\beta}{1-\beta} \qquad \text{(A-22)}$$

Substituting equation (A-22) into equation (A-20) and integrating yields,

$$g_L = \left(\frac{C_L}{C_o}\right)^{-\frac{1}{1-k_o}} \qquad \text{(A-23)}$$

The other limiting case can be defined at chill face where,

and similarly,

$$g_L = \left(\frac{C_L}{C_o}\right)^{-\frac{1-\beta}{1-k_o}} \qquad \text{(A-24)}$$

Assuming a constant partition ratio, k_o=0.172, for Al-4.5%Cu, and taking the value for solidification shrinkage as β=0.055 Flemings el al[8] calculated the amount of segregation as:

ΔC = 0.43% at chill face

$\Delta C = 0$ at steady state

The calculated inverse segregation at the chill face agrees with the experimental values reported by Scheil[1] and the calculated segregation at steady state with the results of Prabhakar and Weinberg[7].

Note that, if the solidification shrinkage is defined by:

$$\beta = \frac{\rho_S - \rho_L}{\rho_S} = \frac{\nu_L - \nu_S}{\nu_L} \qquad \text{(A-25)}$$

as Flemings et al[8] did, the values of β obtained from Fig 1 are negative in the alloys containing more than 9%Cu. When a negative value of β is adopted to above theory, the resulting segregation at the chill face is also negative, which does not agree with positive inverse segregation reported by Scheil[1] and Kirkaldy et al[2]. To validate the model of Flemings et al[8,9], β must always be positive, therefore, the definition of β is not valid for the Al-Cu system.

1.4 Present Objectives

In the segregation models thus far reviewed, the solidification shrinkage is a critical variable. It is believed that this is not clearly defined in the models, and the values adopted to calculate the inverse segregation are incorrect. In addition other assumptions made in the theory are not entirely satisfactory. In order to clarify these problems and to predict inverse segregation in a unidirectionally solidified ingot

precisely, a new model, with minimum assumptions, was developed.

A-II. MODELING PROCEDURE

2.1 Mathematical Formulation

In a unidirectionally solidified ingot three dimensional crystal growth occurs since a dendrite grows three dimensionally because of microsegregation between dendrites and the difference of thermal diffusivities in solid and liquid. To simplify this complex problem, it is assumed that the primary dendrite has a pyramid shape without secondary or higher order dendrite branches. The following assumptions are also made in the mathematical formulation;

1) No surface exudation occurs at the chill face.
2) There is no diffusion in the solid during solidification.
3) Residual interdendritic liquid is completely homogeneous in the plane perpendicular to the growth direction.
4) Local equilibrium conditions exist at the solid/liquid interface.
5) The dendrite shape does not change during solidification.
6) The microsegregation is not affected by interdendritic fluid flow.
7) No shrinkage porosity occurs during solidification.

This requires low gas levels and unrestricted flow of liquid through the dendrite channels.

Under these conditions, the first small amount of solid to form is of composition $k_o C_o$ at the liquidus temperature. During subsequent solidification, solute is enriched in the residual liquid which leads to higher solute concentrations in the solid as solidification progresses. Since diffusion in the solid is assumed negligible, the solute distribution in the solid does not change after solidification occurs.

A quantitative solute mass balance can be expressed by equating the amount of solute rejected from the solid/liquid interface to the solute increase in the liquid. This balance is

$$(C_L - C_S)\, df_S = f_L dC_L \qquad \text{(A-26a)}$$

since $C_s = k_o C_L$ and $f_L = 1 - f_s$:

$$\frac{dC_S}{C_S} = (1-k_o)\,\frac{df_S}{1-f_S} \qquad \text{(A-26b)}$$

Integrating equation (A-26b) from $C_s = k_o C_o$ at $f_s = 0$ yields the solid composition as a function of fraction solid

$$C_S = k_o C_o (1-f_S)^{k_o - 1} \qquad \text{(A-27a)}$$

or in terms of liquid composition and fraction liquid,

$$C_L = C_o f_L^{\,k_o - 1} \qquad \text{(A-27b)}$$

Equations (A-27) have been derived by Scheil[12] and Pfann[13], are called the Scheil equation or Pfann equation. The Scheil equation has been used to predict microsegregation for normal

conditions of casting and ingot solidification in binary alloys by Brody et al[14] and Bower et al[15]. They reported a good correlation between the equation and experimental results.

At the initial stages of solidification, the solid/liquid region can be represented schematically by solid pyramids projecting into the liquid as shown in Fig 2a. Following the above discussion, the microsegregation is governed by equation (A-27) which give the solid and liquid composition profiles along the chill face as shown in Fig 2b. When the dendrite tip reaches L, the fraction solid in the volume element away from the chill face (f_s') can be related to that in the volume element adjacent to the chill face (f_s) by,

$$f_S' = \frac{L-x}{L} f_S \qquad \text{(A-28)}$$

and the composition profile is given by the Scheil equation,

$$C_S = k_o C_o \left(1- \frac{L-x}{L} f_S\right)^{k_o-1} \qquad \text{(A-29a)}$$

and

$$C_L = C_o \left(1- \frac{L-x}{L} f_S\right)^{k_o-1} \qquad \text{(A-29b)}$$

Fig 2c shows the distribution of interdendritic liquid composition in the growing direction calculated from equation (A-29b). It can be seen that the flow of solute enriched liquid to feed shrinkage results in inverse segregation.

The next step is to establish the amount of fluid flow, which is related to the amount of volume contraction. As described in the previous papers[5,9], the volume change occuring

in the process of solidification is made up of three mechanisms.

1) The change due to the liquid/solid phase change.
2) The change due to the density change in the residual liquid associated with composition changes.
3) Thermal contraction associated with temperature changes.

The first two volume changes can be calculated from the equations for microsegregation, equations (A-27) and (A-29). The thermal contraction is determined by the temperature drop.

2.1.1 Alloy Densities

The calculation of the total amount of contraction due to solidification and temperature changes requires accurate information of the densities of the liquid and solid alloys as a function of both composition and temperature. The data reported by Sauerwald[3] (see Fig 1) and Prezel et al[6] are not applicable in the present analysis since the densities they gave assume that the alloy composition at a given temperature are defined by the equilibrium phase diagram, which is not the case. This is the reason that the previous models[1,2,8] were forced to neglect thermal contraction during solidification.

The only reliable data which can be used in the present case are the published values for the temperature dependence of the density for pure metals. Fig 3 shows the temperature dependence of the densities of copper and aluminium compiled by

Smithells[16] and Elliot et al[17]. The corresponding densities for zinc, antimony and bismuth are shown in Fig 4. Provided that a binary exists as a simple mixture of each component, the density of the alloy can be determined from the percentage of the components in the alloy and the components densities at a given temperature. Calculated values of alloy densities for the Al-Cu system using the component densites are compared to those measured directly or compiled by Bornemann et al[18] and Smithels[16] in Table I. For both solids and liquids excellent agreement is obtained between the calculated densities determined from the constituents and the direct measurements with differences of less than 5% at most.

Similar comparisons were made for the Al-Zn and Pb-Sn systems using the data of Bornemann et al[19] and Thresh et al[20] (Table I). Very good agreement is again evident with errors, less than 1.6% and 1.2% in the Al-Zn and the Pb-Sn systems, respectively. These errors are negligible in the present case.

2.1.2 Shrinkage Along The Chill Face

Consider the representative volume adjacent to the chill face (Fig 2a). The solid/liquid interface is plane and the solidification advances unidirectionally because of the microsegregation discussed previously. In the numerical calculation, the volume was subdivided into n elements. When the i-th element is solidified, composition of the remaining

liquid is:

$$C_{Li} = C_o(1-\frac{i}{n})^{k_o-1} \qquad \text{(A-30a)}$$

and the average solid composition of the i-th element is:

$$\bar{C}_{Si} = \int_{i-1}^{i} C_S di = nC_o\left\{(1-\frac{i-1}{n})^{k_o} - (1-\frac{i}{n})^{k_o}\right\} \qquad \text{(A-30b)}$$

until C_{L_i} reaches the eutectic composition. The corresponding temperature of the representative volume (T_{L_i}) can be obtained from the phase diagram as the liquidus temperature for the composition C_{L_i}. Once the eutectic composition is reached, no solute rejection occurs at the solid/liquid interface. From the discussion in the previous section, the density of each element is calculated for the average solid composition ($\bar{C}_{s_i}$) or liquid composition (C_{L_i}) at temperature T_{L_i}. To calculate the volume change in each element, a constant mass within the element is assumed. Then the shrinkage ratio in each element is:

$$SH_i = \frac{\rho_i - \rho_o}{\rho_i} \qquad \text{(A-31)}$$

and the total shrinkage of the whole volume is:

$$\beta_i = \sum_{i=1}^{n} SH_i \qquad \text{(A-32)}$$

The shrinkage formed during the solidification of the i-th element is:

$$\Delta\beta_i = \beta_i - \beta_{i-1} \qquad \text{(A-33)}$$

2.1.3 Segregation in the First Column Adjacent To The Chill Face

Consider the system shown in Fig 5. If the number of subdivision in the x and y directions are equal then the assumption (3) dictates that the solidification proceeds one element by one element in both directions. The growth of the dendrite in the x direction results from the unidirectional heat transfer and the growth in y direction from the microsegregation expressed by equation (A-27).

The first column in Fig 5 coresponds to the representative volume discussed in the previous section. The shrinkage formed in the first column is completely fed by the liquid in the second column. During the solidification of the i-th element in column 1, the liquid composition in column 2 increases from $C_{L_{i-2}}$ to $C_{L_{i-1}}$. Taking the average for the liquid composition in column 2, the segregation caused by the feeding flow during this period is:

$$\Delta C_{L_{i,1}} = \left(\frac{C_{L_{i-2}} + C_{L_{i-1}}}{2} - C_o \right) \Delta\beta_i \qquad \text{(A-34)}$$

and the final segregation after complete solidification of the first column is:

$$\Delta C_1 = \sum_{i=1}^{n} \Delta C_{L_{i,1}} \qquad \text{(A-35)}$$

2.1.4 Positional Segregation

Based on the assumption that shrinkage due to solidification and thermal shrinkage is completely fed with residual liquid, interdendritic fluid flow should occur continuously during solidification. The maximum segregation occurs at the chill face since the liquid required to feed shrinkage is concentrated in solute and there is no liquid flow across the chill face (note that we neglect surface exudations). At an interior position of the ingot, the composition of liquid flowing out of the elemental volume is higher than that of liquid flowing in. Accordingly, the fluid flow across the volume element away from the chill face dilutes the liquid concentration in the volume, decreasing the amount of segregation. Fig 6a shows the feeding sequence schematically. The system is subdivided into thin columns in which the interdendritic liquid is assumed to be completely homogeneous. The dotted line in Fig 6a denotes the actual location of solid/liquid interface. Note that the ratio of length to width for the dendrite remains unchanged on the basis of the assumption that dendrite shape does not change during solidification. The corresponding profile of liquid composition in the solidifying direction is shown in Fig 6b. Fig 7 summarizes the occurance of all the interdendritic fluid flow in the model with 10X10 subdivisions by the time the position L reaches eutectic temperature, that is when the entire model volume has solidified. Each dotted line denotes the actual

location of solid/liquid interface, and the digit in each element the number of columns whose shrinkages cause fluid flow across a particular column at the corresponding location of the interface. The number 5 appearing at (5,6), for example, means that the shrinkages in five columns, 1-5, induce the fluid flow across column 6 because of the fluid flow to feed shrinkages in elements (9,1),(8,2),(7,3),(6,4) and (5,5). Thus the fluid inflow to feed its own shrinkage is not included in this figure.

When the element (i,j) solidifies, (j-1) fluid flows will occur across the j-th column, which are induced by the flows to feed shrinkages in the column (j-1),(j-2),(j-3), - - - - , which is depicted in Fig 8 (Note this description applies for $i+j \leq 11$). Then, the liquid compositions increase from $C_{L_{i-1}}$ to C_{L_i} in the j-th column and from $C_{L_{i-2}}$ to $C_{L_{i-1}}$ in the (j+1)-th column. Taking the averages for the compositions, the liquid to flow out of the column j is $(C_{L_{i-1}} + C_{L_i})/2$ and the liquid to flow into is $(C_{L_{i-2}} + C_{L_{i-1}})/2$ so that the difference between them is given by $(C_{L_i} - C_{L_{i-3}})/2$. Since the microsegregation is not affected by fluid flow, the solidification shrinkages formed in inner columns are the same as that in the first column calculated by equation (A-33). The dilution effect of the above flow induced by the shrinkage in the (j-1)-th column in which (i+1)-th element solidifies is:

$$\Delta C_{L_{i/i+1}} = \left(\frac{C_{L_i} - C_{L_{i-2}}}{2} - C_o \right) \Delta\beta_{i+1} \qquad \text{(A-36)}$$

The sum of dilution effects for (j-1) flow occurances is:

$$\Delta C_{L_{i.j}} = \left(\sum_{i=i+1}^{i+j} \Delta\beta_i \right) \left(\frac{C_{L_i} - C_{L_{i-2}}}{2} - C_o \right) \qquad \text{(A-37)}$$

When the element (5,4) solidifies in Fig 7 for example, the shrinkages in the first, second and third columns will cause fluid flow across the column 4. The composition difference of the liquid flowing into and out of the column 4 is $(C_{L_5} - C_{L_3})/2$ and the sum of dilution effects is:

$$\Delta C_{L_{5,4}} = (\Delta\beta_6 + \Delta\beta_7 + \Delta\beta_8) \left(\frac{C_{L_5} - C_{L_3}}{2} - C_o \right)$$

This kind of dilution flow continues until the whole column solidifies completely, therefore, the total dilution effect for the j-th column is given by:

$$\Delta C_{L_j} = \sum_{i=1}^{10} \Delta C_{L_{i,j}} \qquad \text{(A-38)}$$

Since the feeding flow into a column to compensate its own shrinkage increase the composition of the column by the an amount equal to the increase in the first column, the resulting segregation in the j-th column is:

$$\Delta C_j = \Delta C_1 - \Delta C_{L_j} \qquad \text{(A-39)}$$

2.1.5 The Length of Inverse Segretation Zone

On the assumption that the local equilibrium conditions exist at the liquid/solid interface, the temperature at a dendrite tip corresponds to the liquidus temperature of the alloy. Hence using the dendrite tip temperature, the steady state length of solid/liquid zone, L_s, can be defined as the distance between liquidus isotherm and the chill face when the metal at the chill face reaches the eutectic temperature. The value of L_s can be calculated numerically. The heat transfer equation is given by:

$$\frac{\partial T}{\partial t} = \frac{k}{\rho C_p} \frac{\partial^2 T}{\partial x^2} \qquad \text{(A-40)}$$

for a semi-infinite mold and ingot. During solidification the metal shrinks from the copper chill producing an air gap which lowers the heat transfer between the metal and mould. The heat transfer coefficient through the air gap can be determined from the following expression:

$$h = \frac{k_a}{\delta} + \sigma F \frac{(T_I + 273)^4 - (T_{II} + 273)^4}{T_I - T_{II}} \qquad \text{(A-41)}$$

The latent heat of solidification is taken to be released uniformly between the liquidus and solidus temperatures. Values for the thermal properties used in the numerical calculation are listed in Table II.

2.2 Computer Programming

Based on the mathematical formulation and information discussed in the previous chapter, calculations of segregation were performed numerically with a computer. Fig 9 shows the flow chart for the calculation of inverse segregation at and adjacent to the chill face.

To calculate the length of the inverse segregation zone, the partial differential equation for heat transfer, equation (A-40), was solved implicitly with the finite difference method. The nodal equations for internal nodes are:

$$\frac{T_j^* - T_j}{\Delta t} = \frac{k}{\rho C_p} \frac{T_{j-1}^* - 2T_j^* + T_{j-1}^*}{(\Delta x)^2} \qquad \text{(A-42)}$$

and for surface half node:

$$\rho C_p \frac{\Delta x}{2} \frac{T_j^* - T_j}{\Delta t} = k \frac{T_{j+1}^* - T_j^*}{\Delta x} + h(T_{II}^* - T_j^*) \qquad \text{(A-43)}$$

At each time step, the Gauss-Jordan elimination method was applied to solve the tridiagonal matrix. The actual calculation sequence is shown in Fig 10.

A-III. RESULTS AND DISCUSSION

The mathematical model established in the previous chapter was applied to the calculation of inverse segregation in Al-Cu, Al-Zn and Sb-Bi systems.

3.1 The Aluminium Copper System

The Al-Cu system is a typical eutectic alloy with nearly linear liquidus and solidus lines in the phase diagram (Fig 1). The lines are assumed to be linear in the calculation giving a constant partition ratio during solidification.

3.1.1 Volume Change during Solidification

It is seen in Fig 1 that expansion instead of contraction at liquid/solid phase change appears over most stages of solidification of the Al-Cu alloy. The calculated results of volume change for Al-10%Cu, Fig 11, also reveal this phenomena clearly, where the solid line denotes the sequence of volume change in each solidified element and the dotted line in the residual liquid. Here the equilibrium partition ratio was taken to have a constant value, k_o =0.171. Each element with less than eutectic composition shows expansion during solidification. The

volume expansion ratio increases with an increase of concentration because the volume change is highly dependent on the difference in copper concentration in the liquid and solid. On the other hand, we can observe volume contraction during eutectic solidification because no composition change takes place during solidification after the eutectic composition is reached. The total shrinkage of the whole representative volume is also plotted as a dot dashed line in Fig 11. Of particular importance here is that, even in the solidification process of the region with composition less than the eutectic, where solidification expansion occurs, the total shrinkage ratio for the whole system continues to increase almost steadily. This phenomena can be attributed to the increase in liquid density as a result of solute enrichment in the residual liquid, and to thermal contraction which is observed in Fig 11 as the slight increase of the shrinkage in each element after its solidification. Hence we can conclude that, even though the volume expansion occurs during the liquid/solid phase transformation, the sum of the contraction due to the solute concentration in the liquid and the temperature drop is always greater than the expansion.

Fig 12 shows the calculated results of volume change of each element in Al-5%Cu alloy together with the composition profile of remaining liquid. Note that the volume contraction follows the liquid /solid phase transformation in the beginning of solidification, decreasing with increase of alloy composition. The volume change eventually reverses from

contraction to expansion between elements 4 and 5. The corresponding composition of the reversal point is found to be approximately 7%Cu which is less than the critical value of 9%Cu, obtained by Sauerwald[3].

The calculated total shrinkage ratios are plotted against the alloy composition in Fig 13. These can be compared with the volume change ratios at the liquid/solid phase change obtained from the specific volume data of Fig 1, also shown in Fig 13. The total shrinkage ratio, differing from the local volume change, is always positive with values ranging between 5.2% for Al-25%Cu to 7.2% for nearly pure Al. The abrupt increase in the total shrinkage ratio near pure Al results from the thermal contraction. Neglecting this volume contraction as was done in the previous investigation[1,2,8] would clearly result in a significant error in the calculated values of shrinkage and segregation.

3.1.2 Segregation at the Chill Face

Segregation profiles of the alloys can now be calculated using the complete volume changes discussed above. Positional inverse segregation profiles resulting from these calculations are given in Fig 14 for Al-Cu alloys as functions of fractional distance from the chill face. The initial slopes of the curves decrease with increasing alloy composition. The maximum segregation is obtained at the chill face. The calculated

inverse segregation at the chill face of the Al-Cu alloys as a function of composition is shown by the solid line in Fig 15. As the concentration of copper in the alloy increases, the chill face inverse segregation increases rapidly to a peak value at about Al-12%Cu, then decreases to zero at the eutectic composition. Also plotted in Fig 15 are the experimental measurements by Scheil[1] and Kirkaldy et al[2] and theoretical predictions by Scheil[1] and Flemings et al[8]. The agreement of the model predictions with the experimental values is excellent for copper concentrations less than 15%. At concentrations above 15% the calculated results are greater than the experimental values.

3.1.3 Positional Segregation

The length of the solid/liquid zone adjacent to the chill face is dependent on the rate of heat extraction from the metal at the chill face. This in turn can be markedly influenced by the presence of an air gap between the metal and the chill surfaces due to the contraction of the metal. The length of the solid/liquid region is defined as the distance between the liquidus and the chill at the moment when the metal at the chill face reaches the eutectic temperature. The calculated zone length is plotted in Fig 16 as a function of the width of air gap for three melt superheats, as indicated. The length of the solid/liquid zone is observed to increase rapidly with small

increases in the air gap. The length goes from nearly zero to 15mm with the formation of a small gap of 10μm with a superheat of 40°C. The rate of increase is highest with the lowest melt superheat.

There are relatively few reliable measurements of the length of the solid/liquid region, particularly with the length being very sensitive to the solidification conditions. Reliable measurements have been reported by Prabhakar and Weinberg[7] using radioactive tracer techniques to measure the inverse segregation. Their results show that the length of solid/liquid region with 41°C superheat is approximately 5mm for Al-10%Cu. It is indicated from Fig 16 that there was an air gap of 3μm between the alloy and the chill in their measurements.

Inverse segregation adjacent to the chill face (positional segregation) calculated from the present theory for Al-10%Cu is shown in Fig 17. For comparison the results reported by Prabhakar et al[7] and the theoretical prediction of Kirkaldy et al[2] are also shown. The inverse segregation calculated from the present theory is a little lower than the experimental results of Prabhakar et al. The results by Kirkaldy et al deviate further from the experimental results near the chill and maintain a positive value after 5mm when the measured value is zero. Inverse segregation is reported by Kirkaldy et al well away from the chill face, differing from the results of the present model and the experimental results of Prabhakar et al.

Prabhakar and Weinberg[7] have also found that with melt

superheats above 40°C the concentration at the chill face drops rapidly with increasing superheat against a copper chill. This occurance can be accounted for from the results given in Fig 16. The superheat reduces the thickness of air gap at mold/metal interface which lowers the length of the solid/liquid region. It is quite difficult to measure the chill face segregation properly within a very narrow inverse segregation zone.

3.2 The Aluminium Zinc System

The phase diagram of the Al-Zn alloy system is shown in Fig 18. In this case the solidus and liquidus lines cannot be assumed to be linear. To apply the segregation model to this system, the phase diagram was divided into nineteen portions, every 5% along liquidus. The solidus and liquidus lines were assumed to be linear in each portion giving a constant partition ratio.

The calculated total shrinkage ratio is plotted as a function of composition in Fig 19. The shrinkage ratio decreases with increase of composition in the low alloy region, then increases slightly as it approaches the eutectic composition. The increase of total shrinkage near pure Al, which is much more prominent than that in Al-Cu (Fig 12), is also caused by the thermal shrinkage. In the region between 10% to 40%Zn, the decline of shrinkage is markedly accelerated.

Fig 20 shows the calculated results of volume change for Al-10%Zn. Similar to the Al-Cu alloy, the reversal from shrinkage to expansion in volume change during liquid/solid transformation is observed in the low composition region. This critcial point lies between the elements 7 and 8. However, independent of shrinkage or expansion during the solidification of each element, the total shrinkage keeps increasing steadily until the solid/liquid reaches the final part of solidification. During the solidification of the final element, the shrinkage for both, each element and their total, are significantly raised. This occurrence can be accounted for by the large thermal shrinkage resulting from the long freezing range of the element 10. The liquid composition in this element increases from 31% to 95%Zn because of the solute rejection away from the solid/liquid interface during its solidification and so the temperature of the system, as seen in the same figure, is required to drop from 600°C to 382°C. Considering that the interdendritic fluid to feed shrinkage is solute enriched during solidification and has the highest composition (eutectic) at the end of solidification, the shrinkage formed at the late stage of solidification makes far more contribution to macrosegregation than that at the initial stage.

Fig 21 summarizes the temperature profiles in various compositions of Al-Zn. It can be clearly seen that the thermal contraction at the end of solidification rapidly decreases with increase of composition in the low alloy region. If we neglect this thermal contraction as Youdelis et al[4] did, the resulting

segregation for low alloy Al-Zn must be far less than that calculated in the present work.

The rapid decrease in the total shrinkage observed in Fig 19 can be attributed to the decrease in thermal contraction, proving that the thermal contraction plays an important role in shrinkage and macrosegregation in Al-Zn alloy. The inverse segregation at the chill face, is plotted against composition in Fig 22. Unlike the smooth curve for Al-Cu alloy, the curve for Al-Zn consists of a rise and fall in composition up to 40%Zn, followed by a slow progressive decrease in composition to the eutectic. The decline of the inverse segregation after the peak at 20%Zn is due to the accelerated decrease in total shrinkage. The progressive slower decrease in segregation after 40%Zn is due to a nearly constant and very low shrinkage ratio (Fig 19). Also plotted in Fig 22 are experimental and theoretical results by Youdelis and Colton[4]. The present model prediction agrees with the reported results in the region up to 23%Zn even though thermal contraction was neglected in the previous investigation. Beyond 23%Zn there is a strong discrepancy between the present results and the results of Youdelis and Colton[4]. It should be noted that there is considerable scatter in the reported data which makes the comparison with the measured results and the models only approximate. As has been demonstrated earlier, the inverse segregation is very sensitive to the casting conditions.

3.3 The Antimony Bismuth System

This alloy is unique in that both metals expand during solidification (see Fig 4). The phase diagram for the Sb-Bi system is shown in Fig 23. There is complete solid solubility of Bi in Sb over the enitre composition range, differing from the other two systems investigated. Following the same procedure used in the Al-Zn system with non linear solidus and liquidus lines, the phase diagram was divided into twenty sections, each of 5%Bi, and the solidus and liquidus lines assumed linear in each section with a constant partition ratio.

The total shrinkage ratio for Sb-Bi, as a function of alloy composition is given in Fig 24. Two different shrinkage sequences are clearly observed, one region between zero and 30%Bi where the shrinkage ratio decreased rapidly, and above 30%Bi where the shrinkage decreases slowly. The abrupt increase in the shrinkage near pure Sb is attributed to the thermal contraction during solidification, which shifts the negative value of shrinkage for the pure Sb to the positive side.

The detailed volume change and temperature profile for Sb-10%Bi is shown in Fig 25. The solid line denotes the volume change in each solidified element and the dotted line the volume change in residual liquid. Every element shows extensive volume expansion on solidification except for the last element whose volume expansion is compensated by the thermal contraction. Although the remaining liquid continues to shrink during

solidification because of the density change due to solute concentration and a slight temperature drop, the whole volume expands steadily until the solid/liquid interface reaches the final element to solidify. The volume expansion as a total system must cause the interdendritic flow of solute enriched fluid to move away from the volume elememt resulting in normal segregation. On the other hand, the contraction occurs during the solidification of the last element reversing the flow. The temperature profile shown in Fig 25 indicates that the temperature drops from 530°C to 271°C during solidification, which results in a marked contraction, as clearly observed in the volume change. This thermal contraction at the late stage of solidification reverses the total shrinkage from expansion to contraction, which results in extensive macrosegregation since the interdendritic fluid which feeds the shrinkage has the maximum composition, 100%Bi, at the end of solidification.

The calculated inverse segregation profile at the chill face for the Sb-Bi alloy is shown in Fig 26, as well as the experimental and theoretical results reported by Youdelis[5]. Maximum segregation at the chill face was observed at 13%Bi, and minimum segregation at 70%Bi. The reversal from inverse segregation at the chill face to normal segregation occurs at approximately 30%Bi. The present results agree reasonably well with the experimental results, considering the uncertainity of the measured data.

Comparing the segregation profile with the total shrinkage

ratio (Fig 24) shows the composition in the segregation profile at which the segregation is reversed (30%Bi) does not coincide with the point at which the shrinkage ratio is zero (20%Bi). Between 20% and 30%Bi, there is expansion associated with solidification and yet inverse segregation is observed which is anomalous. This can be accounted for by the volume change and temperature sequence for Sb-20%Bi which is found to have an almost zero solidification shrinkage ratio. In Fig 27, similar distribution of volume change to that of Sb-10%Bi (Fig 25) can be observed with large expansion at freezing of each element and slight decrease of total shrinkage during solidification. The integrated negative shrinkage is made up by the thermal contraction due to the temperature drop at the late stage of solidification. The same thing must occur during the solidification of Sb-Bi alloy up to 30%Bi. It can be now confirmed that, even though the total shrinkage ratio is zero or negative, the positive segregation resulting from the thermal contraction at the late stage of solidification always overcomes the negative segregation formed at the primary stage in the Sb-Bi alloy with 20% to 30%Bi. Again it is reminded that the residual liquid is enriched in solute by the advance of the solid/liquid interface. Of particular importance is that, in order to calculate the macrosegregation in the alloy accurately, it is essential to obtain the information of volume change over the entire solidification process as well as the total volume change. The behaviour of interdendritic fluid flow at the late stage of solidification controls the overall segregation.

3.4 Examination Of Previous Model Predictions

In the discussion of the present computer calculated results it has been pointed out that the thermal contraction plays a much more significant role in the formation of inverse segregation than is generally accepted. This is particularly the case for the Al-Zn and Sb-Bi alloys at low compositions. Previous calculations did not include thermal contraction in the models[1,2,8-11]. Without thermal contraction the calculations will give low values for the inverse segregation.

To clarify the contradictions found in the comparison of present work with the previous calculations, calculations of chill face inverse segregation values were repeated using the models and assumptions used previously[1,2,4,5]. The repeated calculations for the three alloy systems did not coincide with the published curves, as shown in Appendix A. It is not clear what is the cause of the discrepancy.

A-IV. CONCLUSIONS

The present results show inverse segregation observed near the chill face is governed by the back flow of solute enriched liquid through dendrite channels resulting from volume contraction during solidification. A mathematical model is developed which quantitatively determines the inverse segregation at the chill face, and adjacent to the chill face. The model includes the effect of thermal contraction due to the temperature changes as well as contraction due to composition changes. Comparing the values of segregation determined from the model for the Al-Cu, Al-Zn and Sb-Bi alloys with experimental values shows reasonable agreement between the predicted and observed values.

The following conclusions have been reached.

1) A binary alloy may be considered as a simple mixture of the two componets in order to determine the density of both solid and liquid.
2) The volume change during solidification consits of three parts.
    a). The volume change due to the liquid/solid phase transformation.
    b). Contraction in the residual liquid due to solute concentration.
    c). Thermal contraction due to temperature changes.

3) Volume expansion occurs over most stages of solidification in both the Al-Cu and Al-Zn systems due to liquid/solid change but this is compensated for by the other two effects producing a net contraction.

4) Thermal contraction plays a significant role in the inverse segregation of Al-Zn and Sb-Bi in low alloy composition regions since large temperature drops occur in the last stage of solidification.

5) To calculate macrosegregation it is essential to know the volume change over the entire solidification process since the behaviour of interdendritic fluid flow at the late stage of solidification controls the overall segregation.

6) The solidification shrinkage ratio of an alloy is a function of the volume change on solidification, compositional changes in the liquid and temperature changes, all of which must be considered in any signficant model for segregation.

7) The length of solid/liquid region adjacent to the chill face is highly sensitive to the contact thermal resistance at mold/metal interface associated with the formation of an air gap at the chill face.

Table I - The comparison of alloy densities with those calculated from data for pure metals

Alloy	Temp(°C)	ρ-solvent[1]	ρ-solute[1]	ρ-mean	ρmeasured	Error(%)
Al-4.5%Cu	20	2.70	8.93	2.82	2.75[2]	2.5
Al-4.5%Cu	800	2.34	8.15	2.45	2.45[3]	0
Al-4.5%Cu	1000	2.29	7.99	2.40	2.40[3]	0
Al-8%Cu	20	2.70	8.93	2.92	2.83[2]	3.2
Al-10%Cu	800	2.34	8.15	2.60	2.55[3]	2.0
Al-10%Cu	1000	2.29	7.99	2.53	2.50[3]	1.2
Al-12%Cu	20	2.70	8.93	3.04	2.93[2]	3.8
Al-20%Cu	1000	2.29	7.99	2.84	2.75[3]	3.3
Al-40%Cu	800	2.34	8.15	3.62	3.45[3]	4.9
Al-80%Cu	1200	2.25	7.84	5.76	5.60[3]	2.9
Al-5%Zn	700	2.36	6.45	2.45	2.45[4]	0
Al-5%Zn	900	2.31	6.35	2.39	2.40[4]	0.4
Al-10%Zn	700	2.36	6.45	2.54	2.55[4]	0.4
Al-10%Zn	900	2.31	6.35	2.49	2.45[4]	1.6
Al-20%Zn	700	2.36	6.45	2.74	2.70[4]	1.5
Al-40%Zn	700	2.36	6.45	3.24	3.20[4]	1.5
Pb-5%Sn	315	10.68	6.91	10.36	10.40[5]	0.4
Pb-10%Sn	300	10.70	6.92	10.09	10.15[5]	0.6
Pb-20%Sn	275	10.73	6.94	9.58	9.70[5]	1.2
Pb-40%Sn	235	10.78	6.97	8.73	8.80[5]	0.8

Note: 1. Smithells[16] and Elliot et al[17]
2. Smithells[16]
3. Bornemann et al[18]
4. Bornemann et al[19]
5. Thresh et al[20]

Table II - The thermal properties employed for the calculation of temperature distribution

	Al-10%Cu	Cu mold
thermal conductivity, k(cal/cm.s.°C)	0.43	0.94
specific heat, Cp (cal/g.°C)	0.259	0.093
density, ρ (g/cm^3)	variable	8.89
latent heat of solidification, Hs (cal/g)	93.0	-
emissivity, ϵ	0.18	0.18
thermal conductivity of air gap, ka	1.0×10^{-4} cal/cm.s.°C	
shape factor through air gap	0.10	

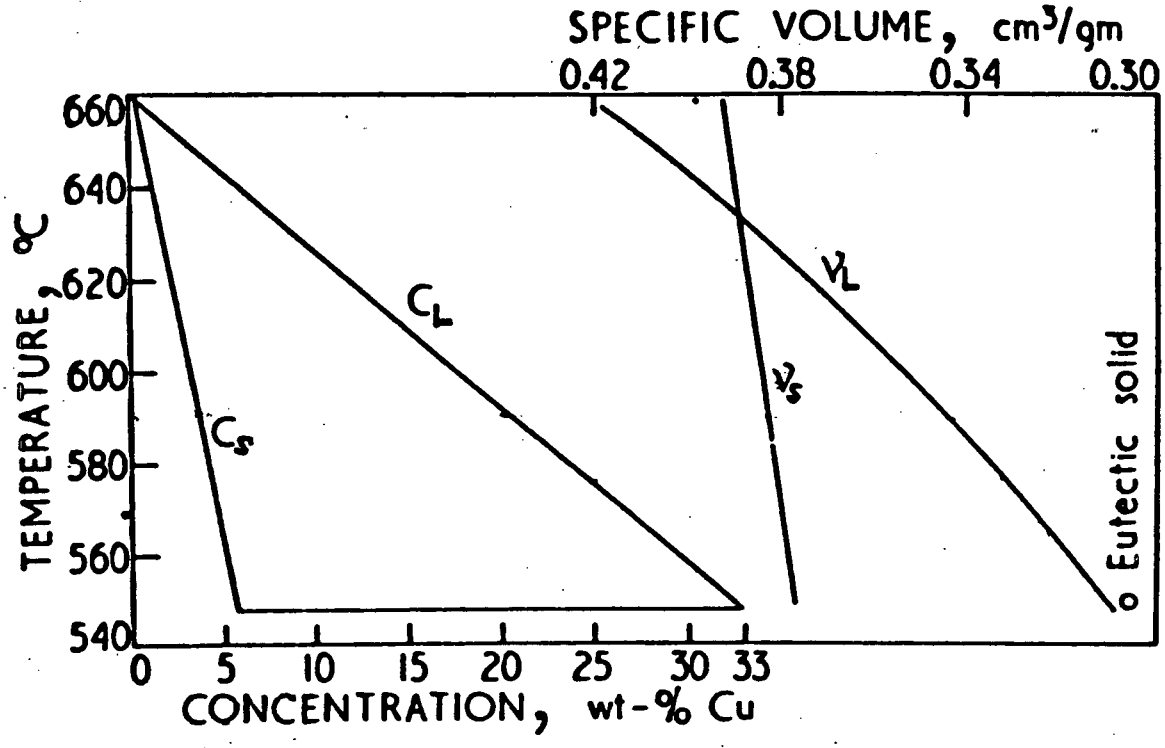

Figure 1 - Equilibrium phase diagram and specific volume for the Al-Cu alloys

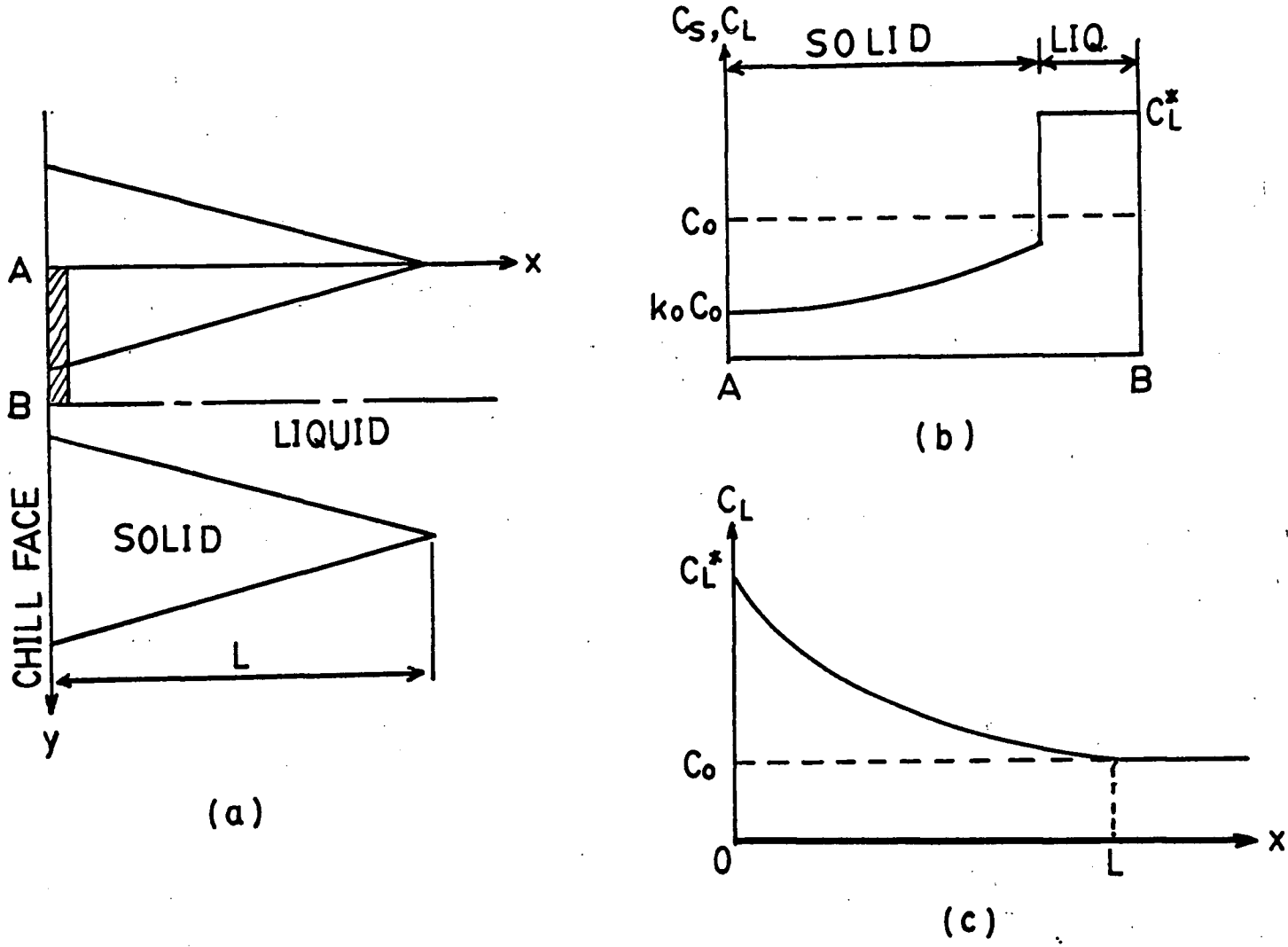

Figure 2 - Schematic description of solidifying zone; (a) dendrite morphology, (b) solid and liquid compositions along chill face, and (c) composition of interdendritic liquid

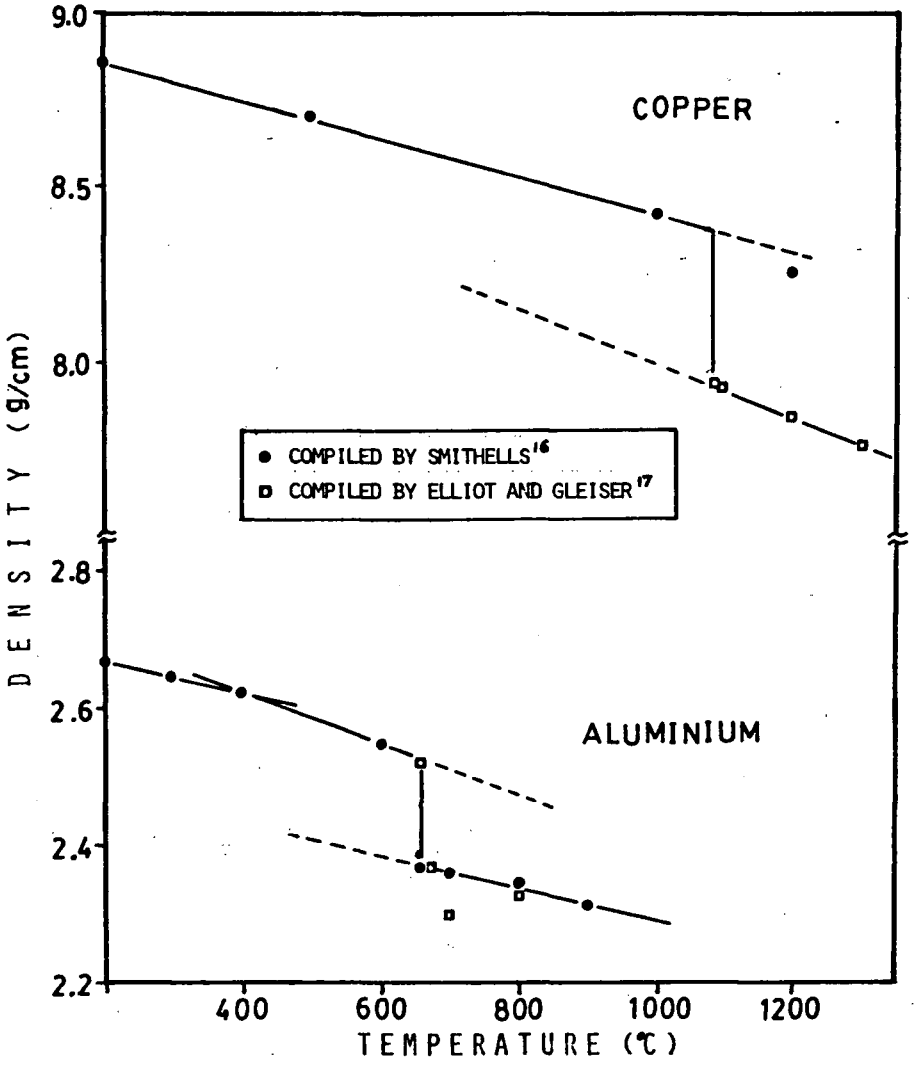

Figure 3 - Densities of copper and aluminium vs temperature

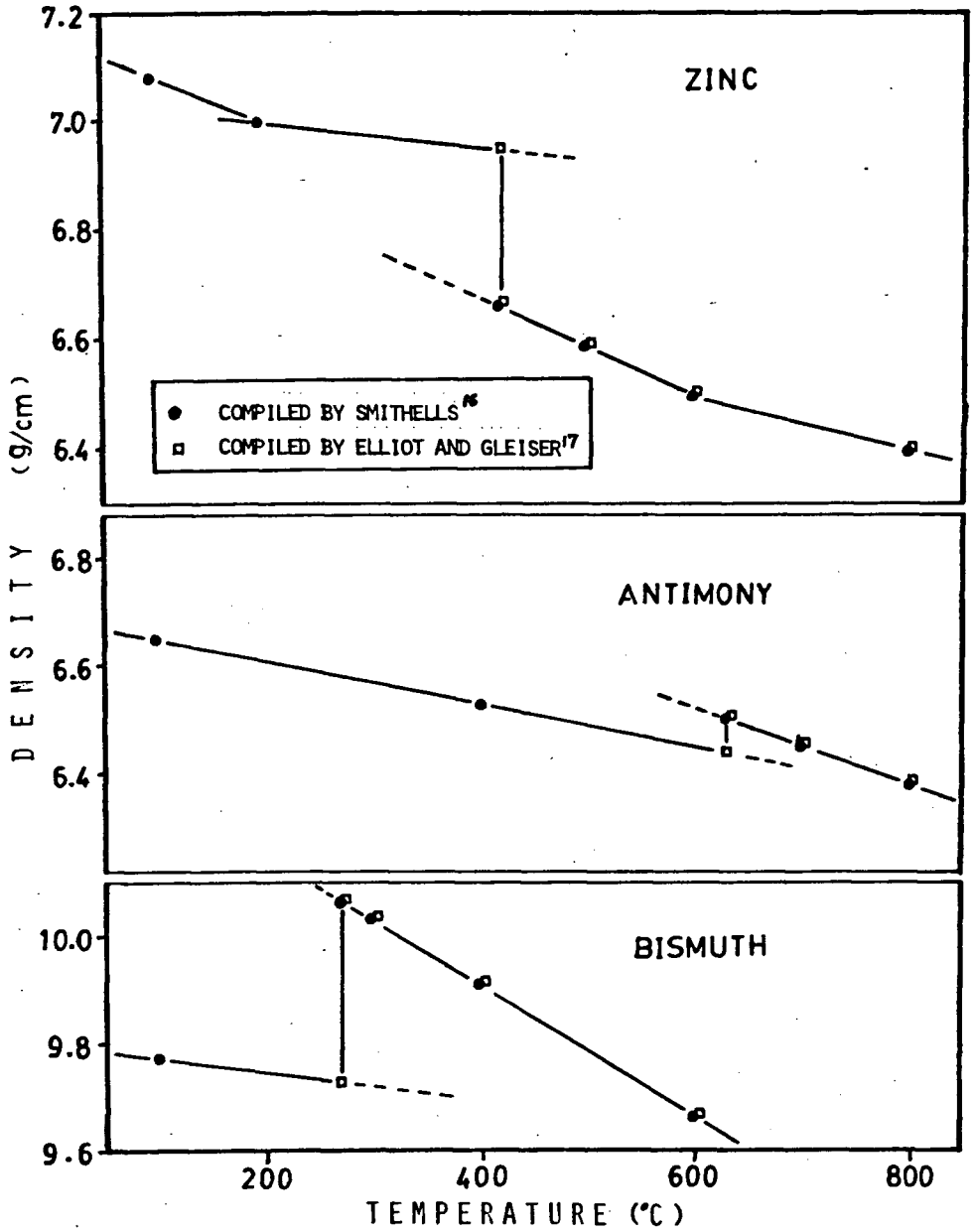

Figure 4 - Densities of Zinc, Aluminium and Bismuth vs temperature

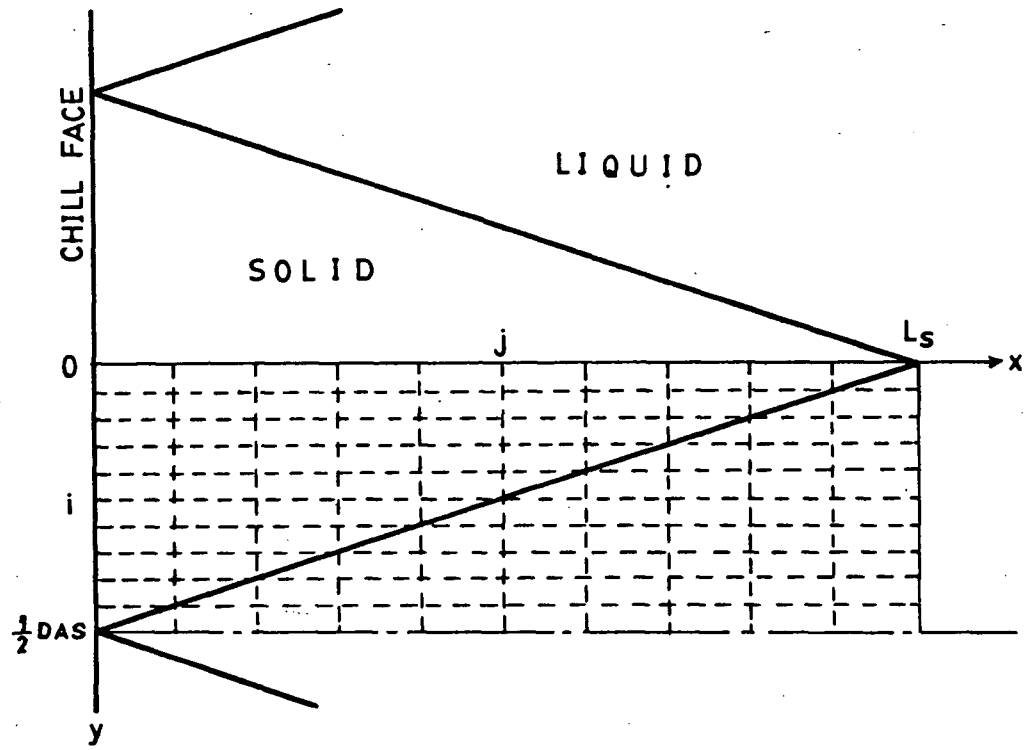

Figure 5 - Schematic configuration of the model investigated and the subdivision for the numerical simulation

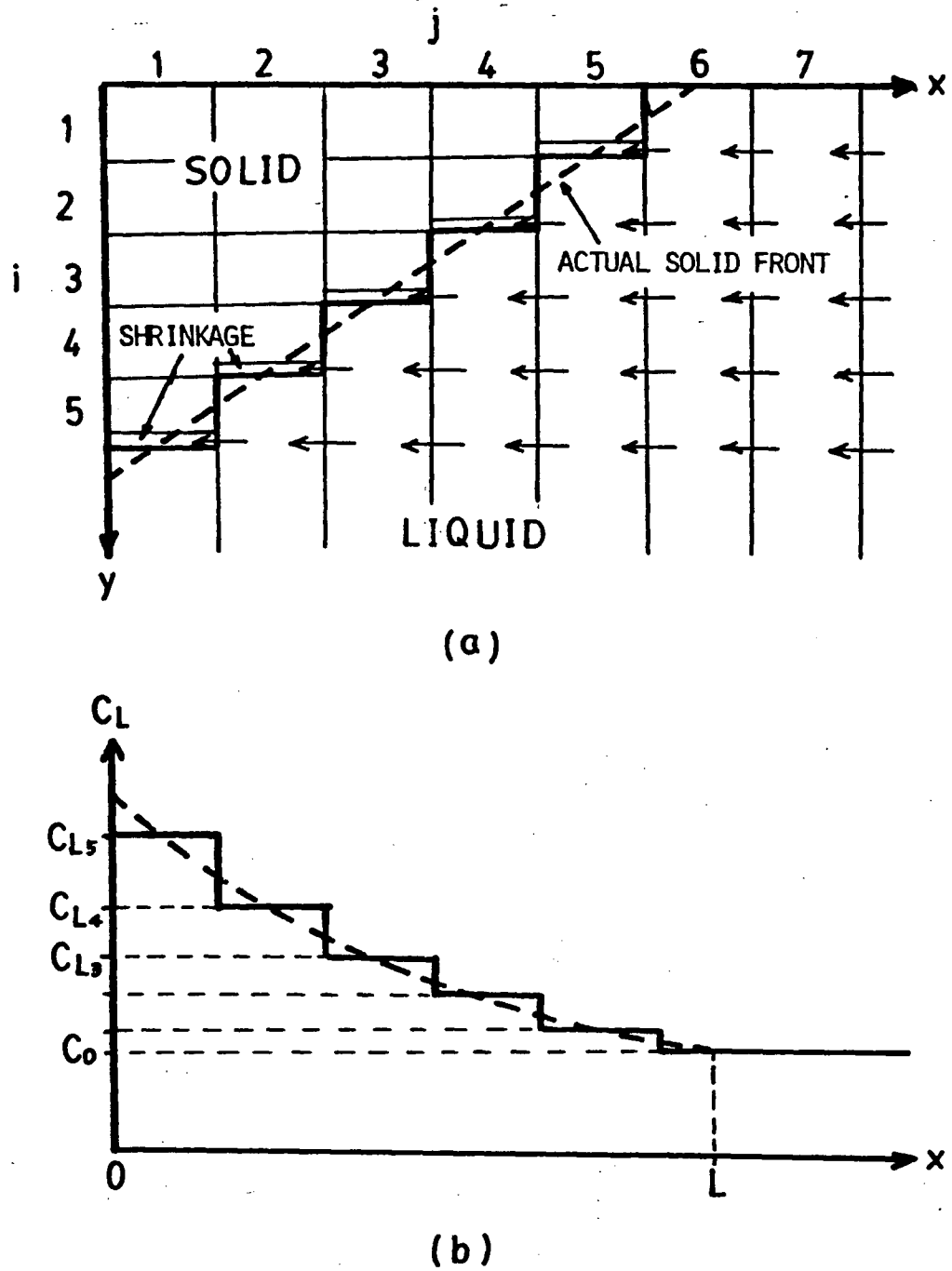

Figure 6 - Schematic configuration of the feeding sequence; (a) Fluid flow, and (b) profile of the liquid composition

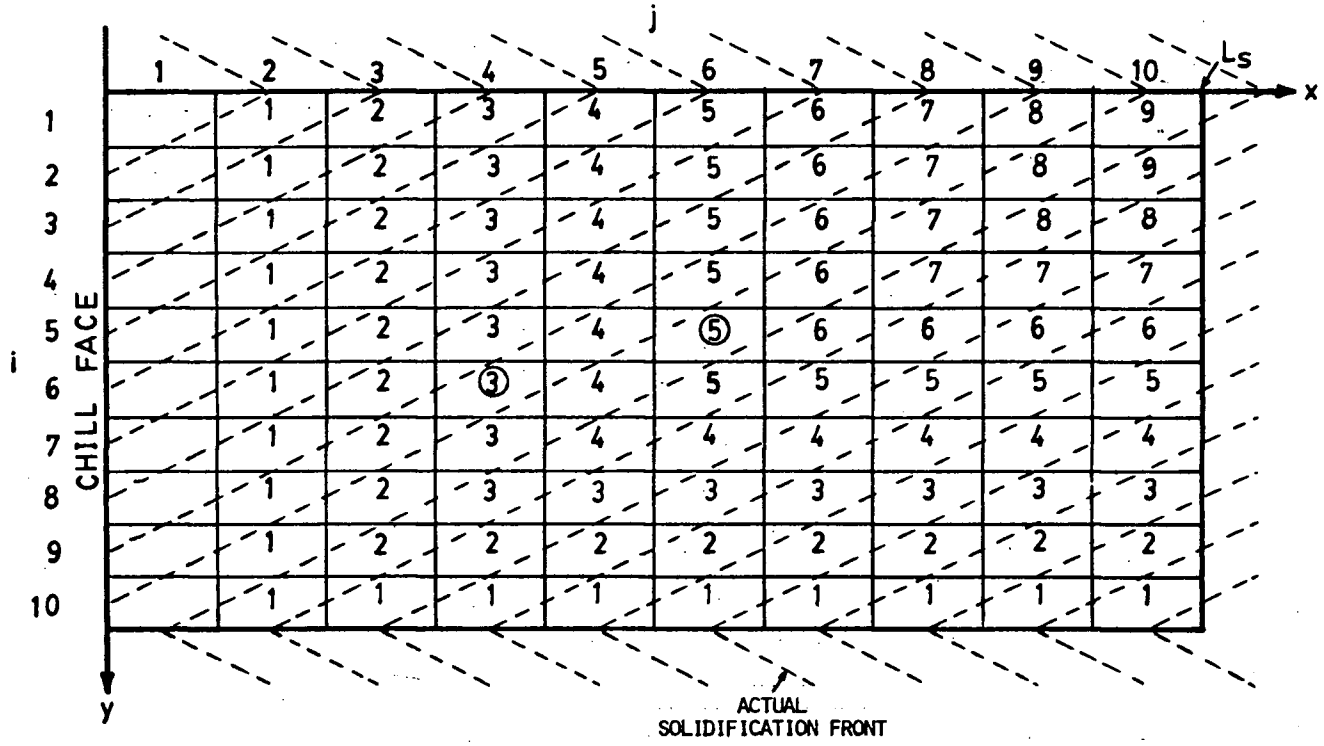

Figure 7 - Summary of the fluid flow induced by the shrinkage during the solidification of the model with 10X10 subdivisions

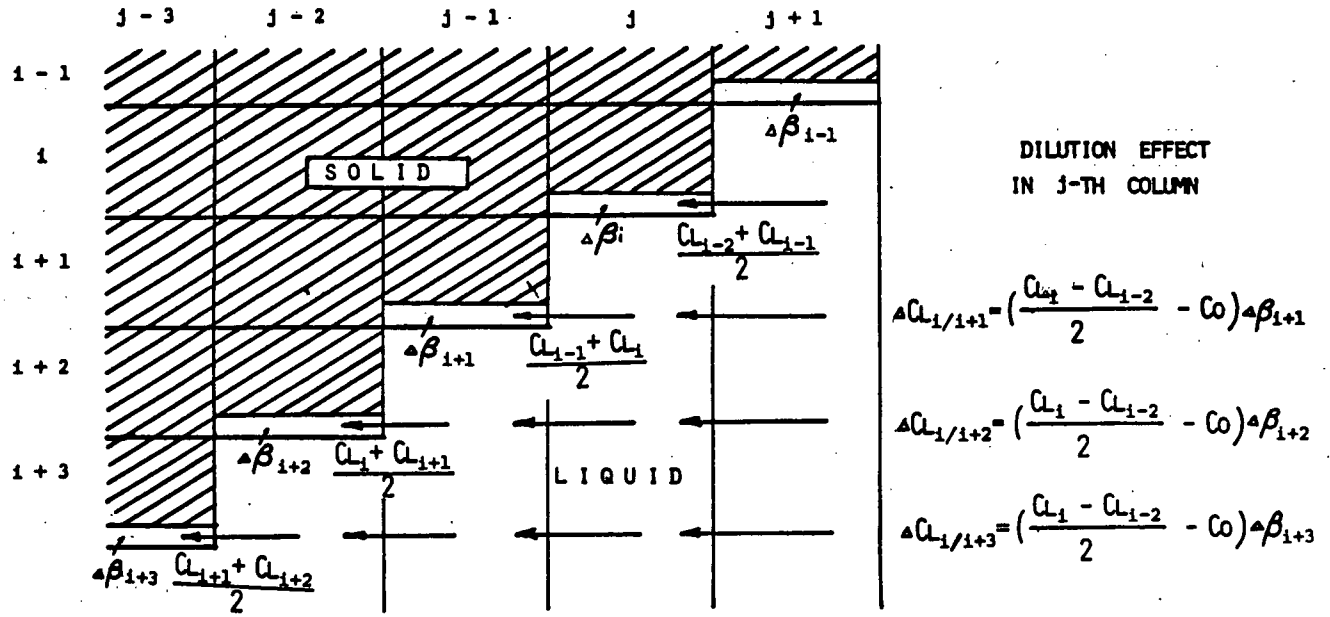

Figure 8 - Schematic description of the dilution effect of the interdendritic fluid flow during solidification

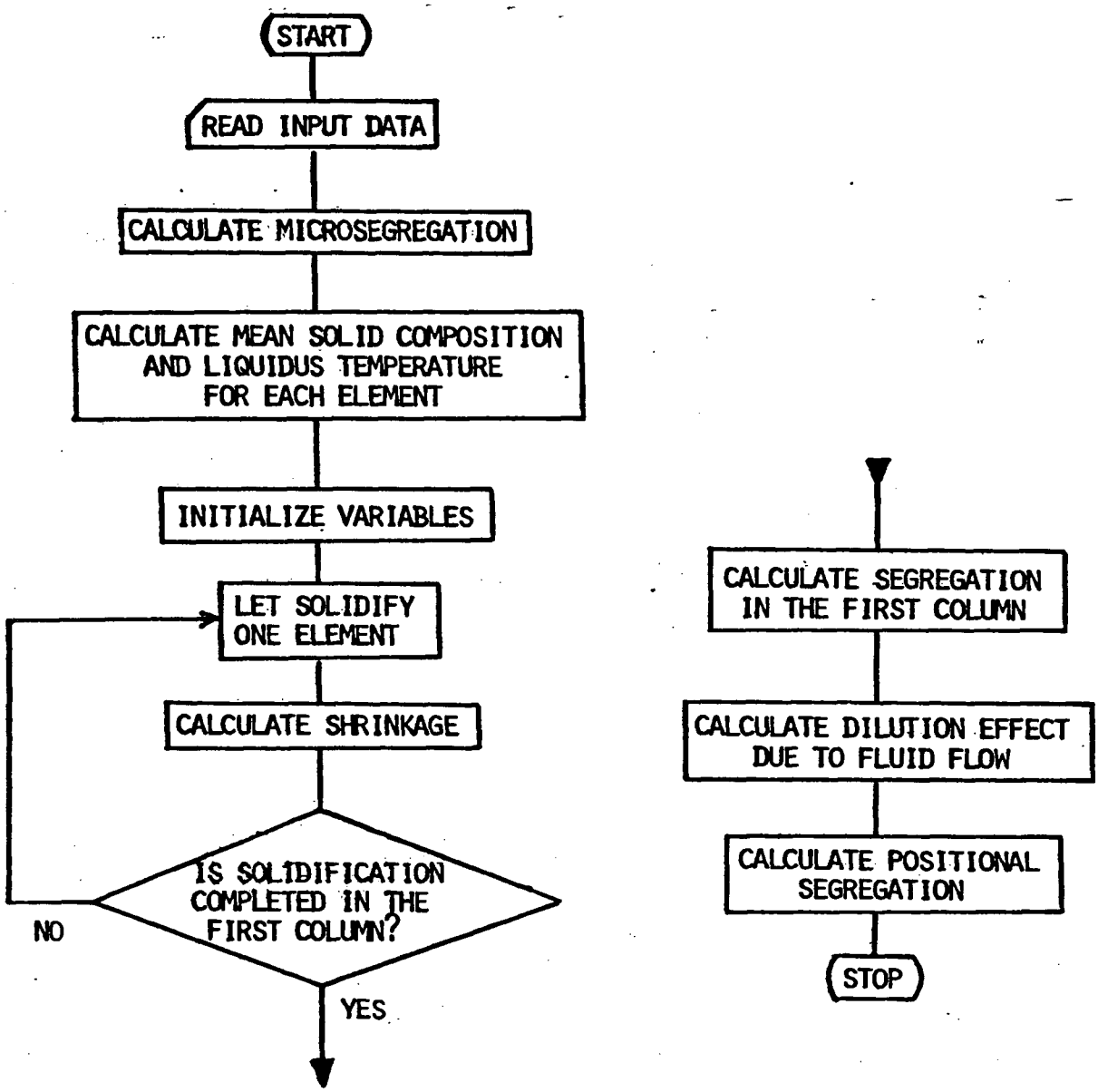

Figure 9 - Flow chart for the calculation of inverse segregation

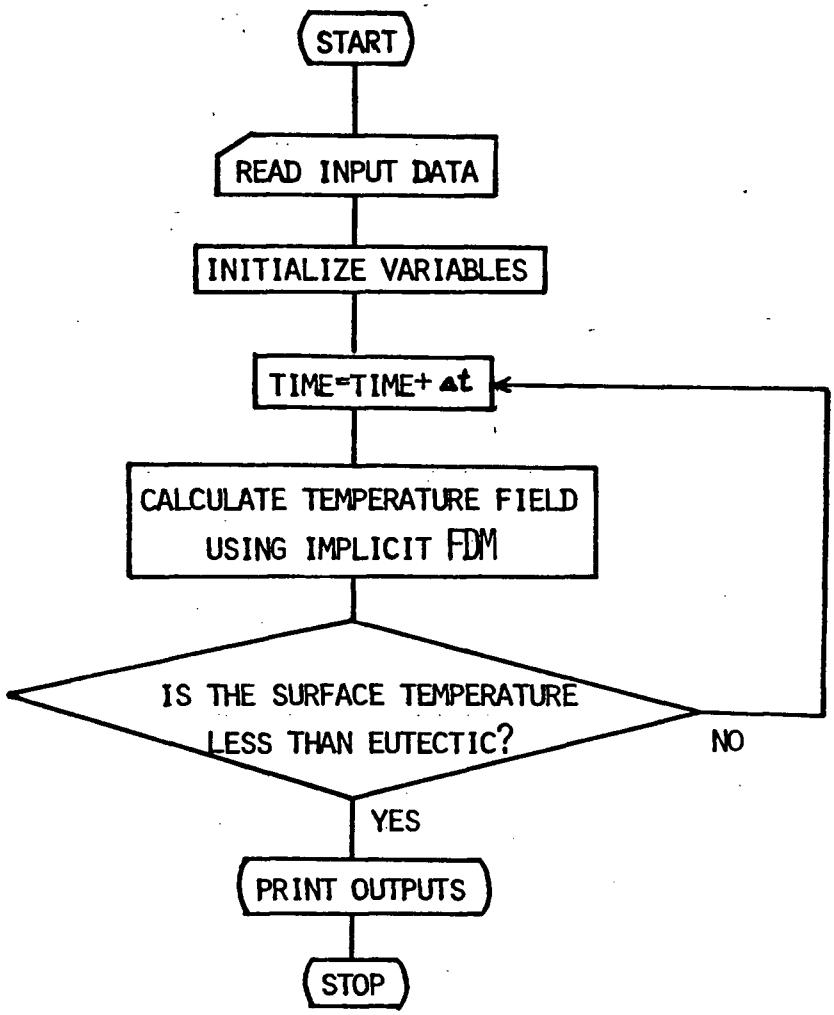

Figure 10 - Flow chart for the calculation of the length of solid/liquid zone adjacent to the chill face

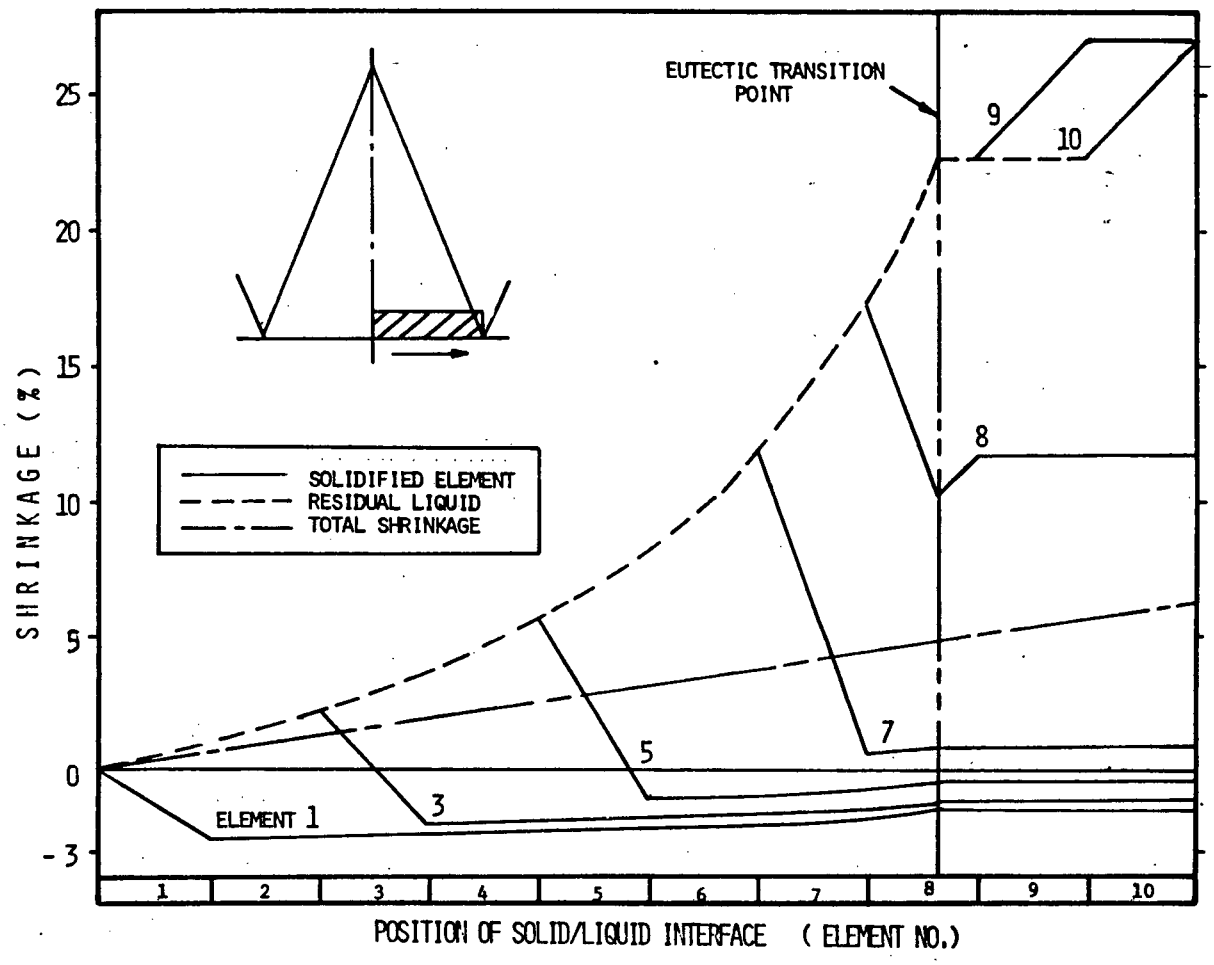

Figure 11 - Calculated volume change during solidification of Al-10%Cu. The number on the curve denotes each element solidified.

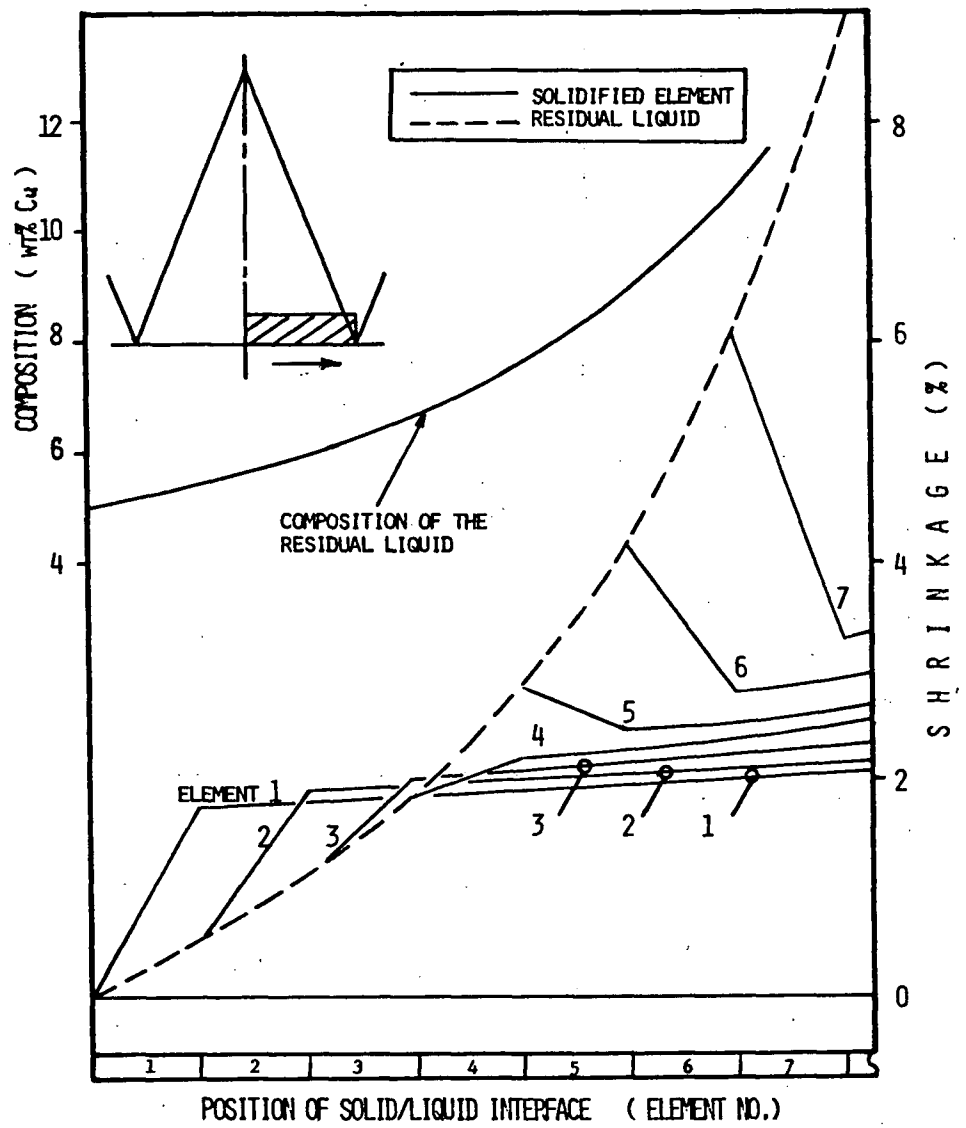

Figure 12 - Calculated volume change and liquid composition in the representative volume for Al-5%Cu. The number on the curve denotes each element solidfied.

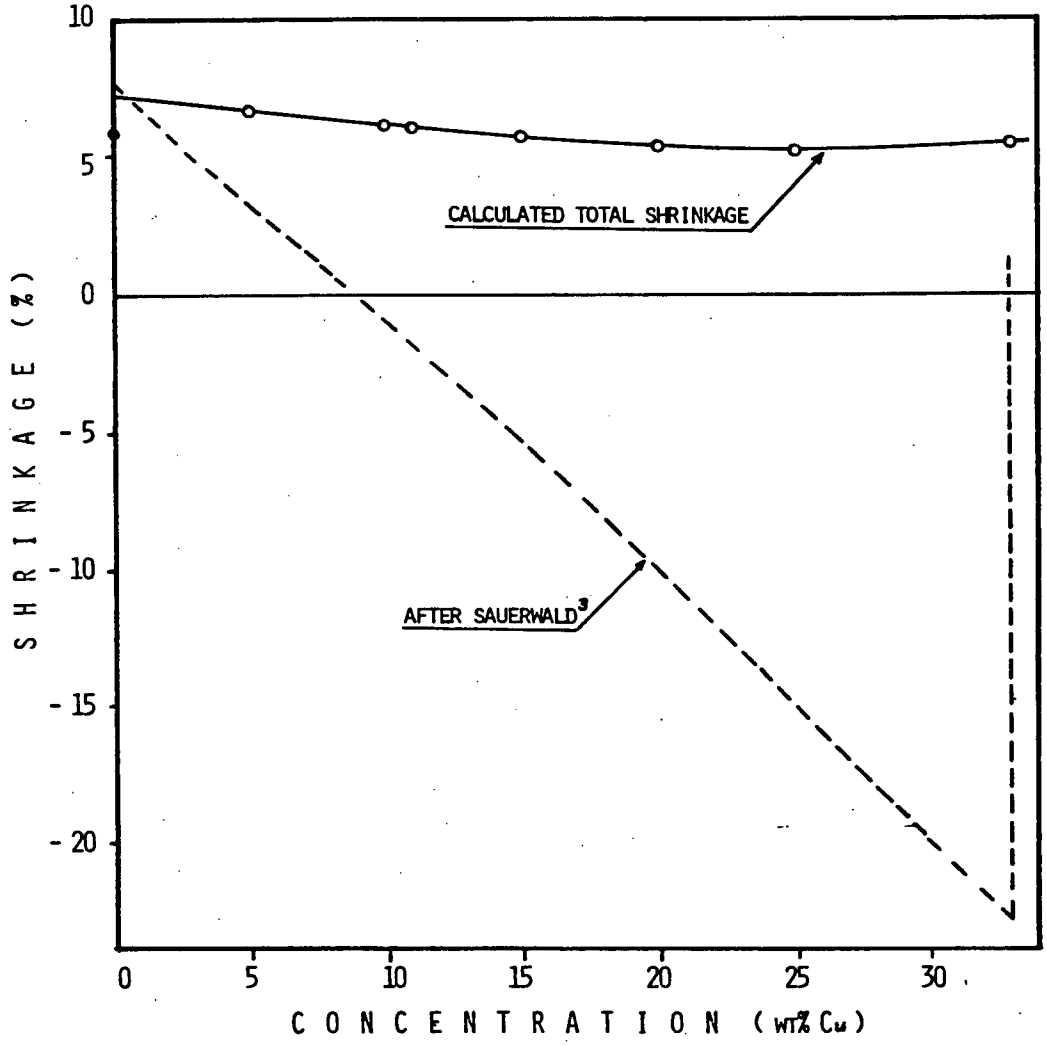

Figure 13 - Solidification shrinkage ratio vs composition of the Al-Cu alloys. The dotted line was derived from Fig 1.

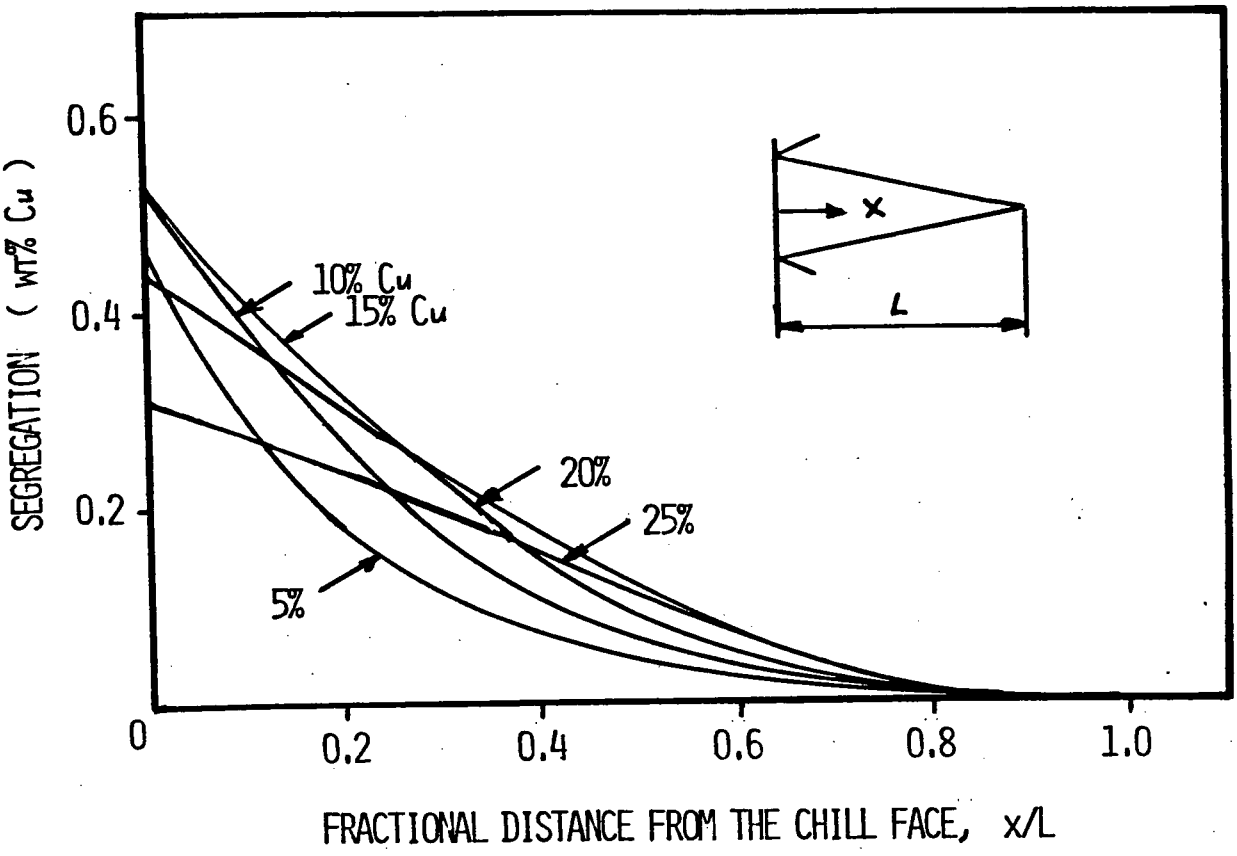

Figure 14 - Positional segregation profiles for various compositions of the Al-Cu alloys

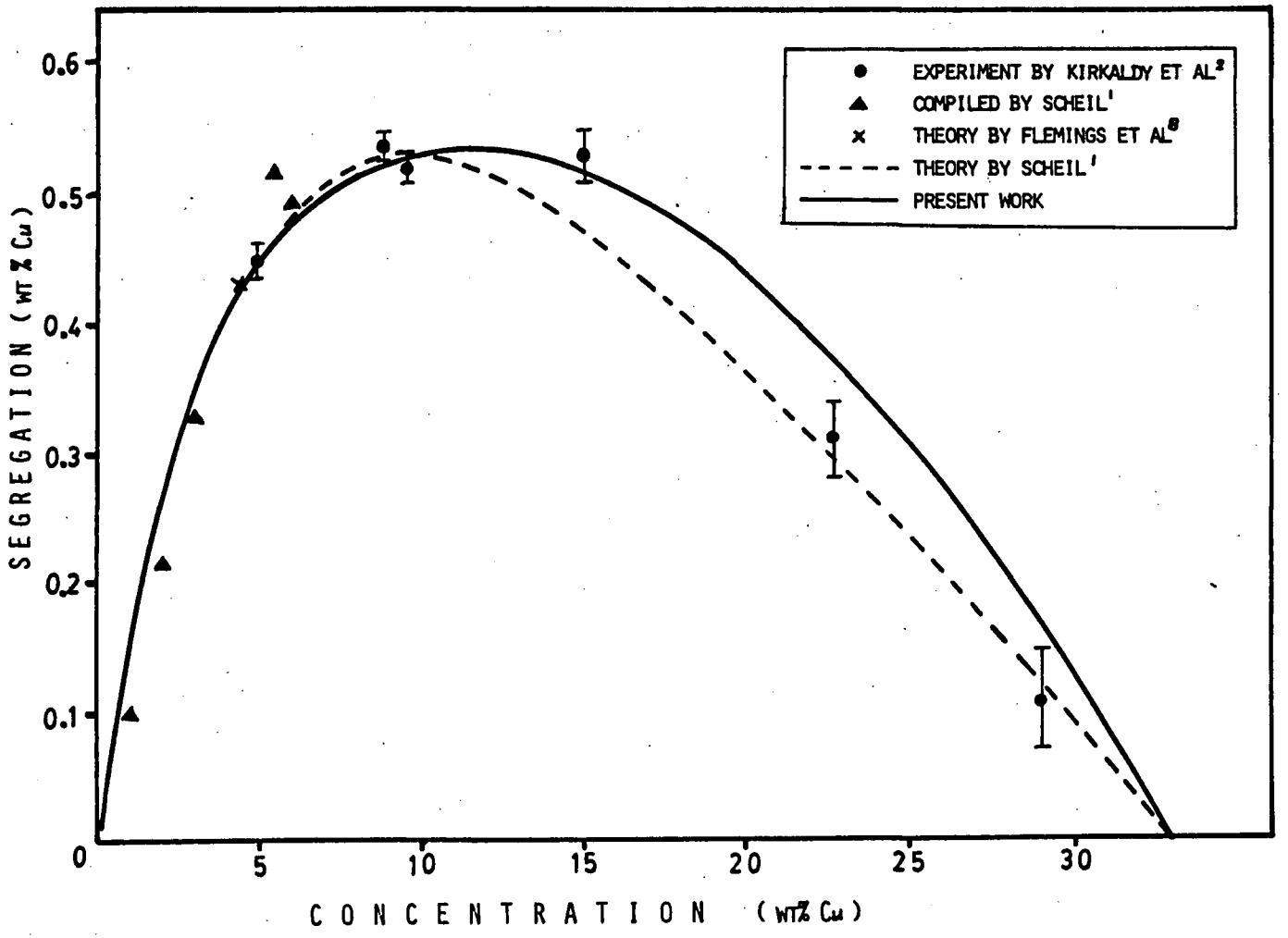

Figure 15 - Comparison of the inverse segregation at the chill face for the Al-Cu alloys

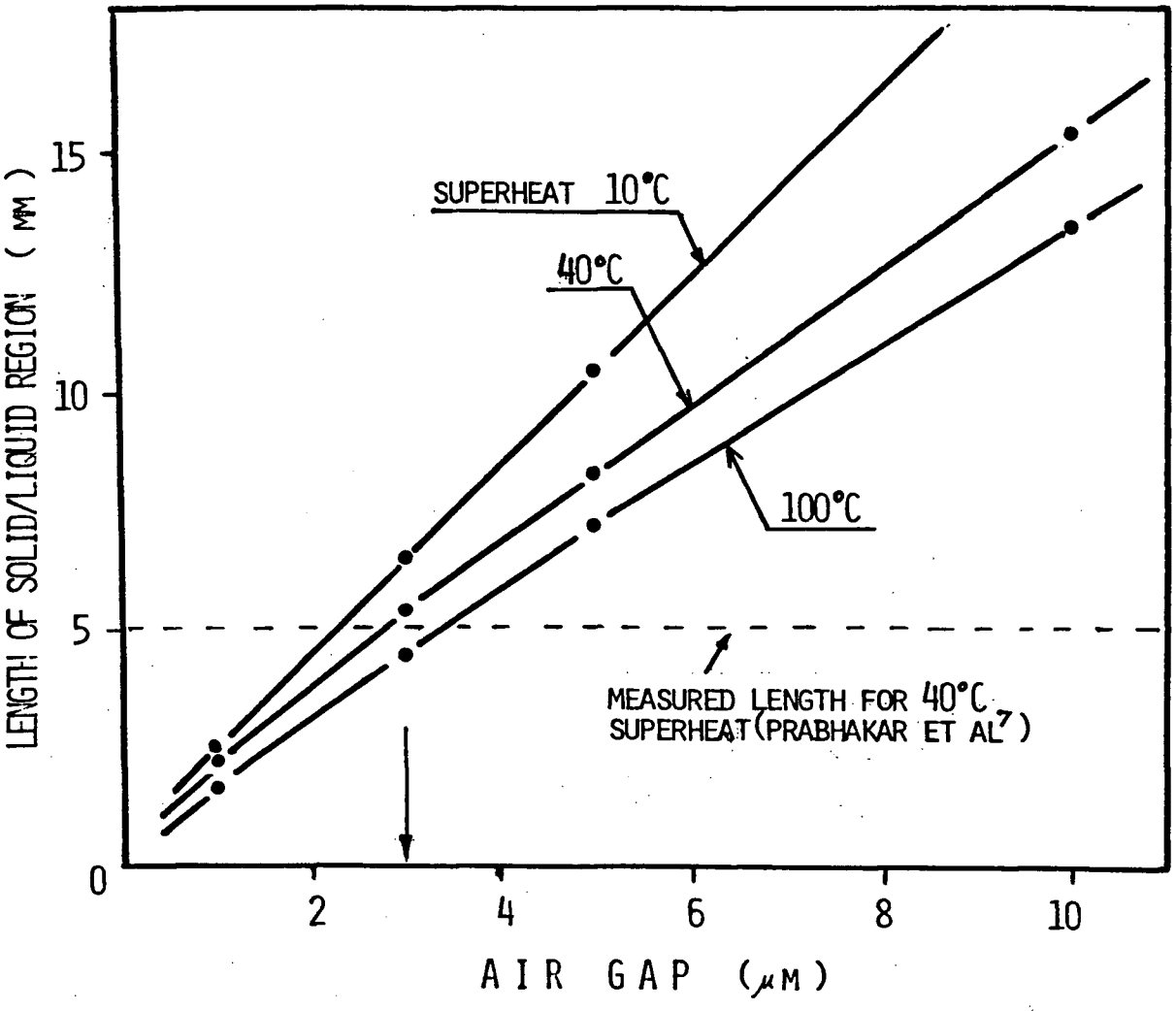

Figure 16 - Effect of air gap at the metal/mold interface on the length of solid/liquid zone adjacent to the chill face

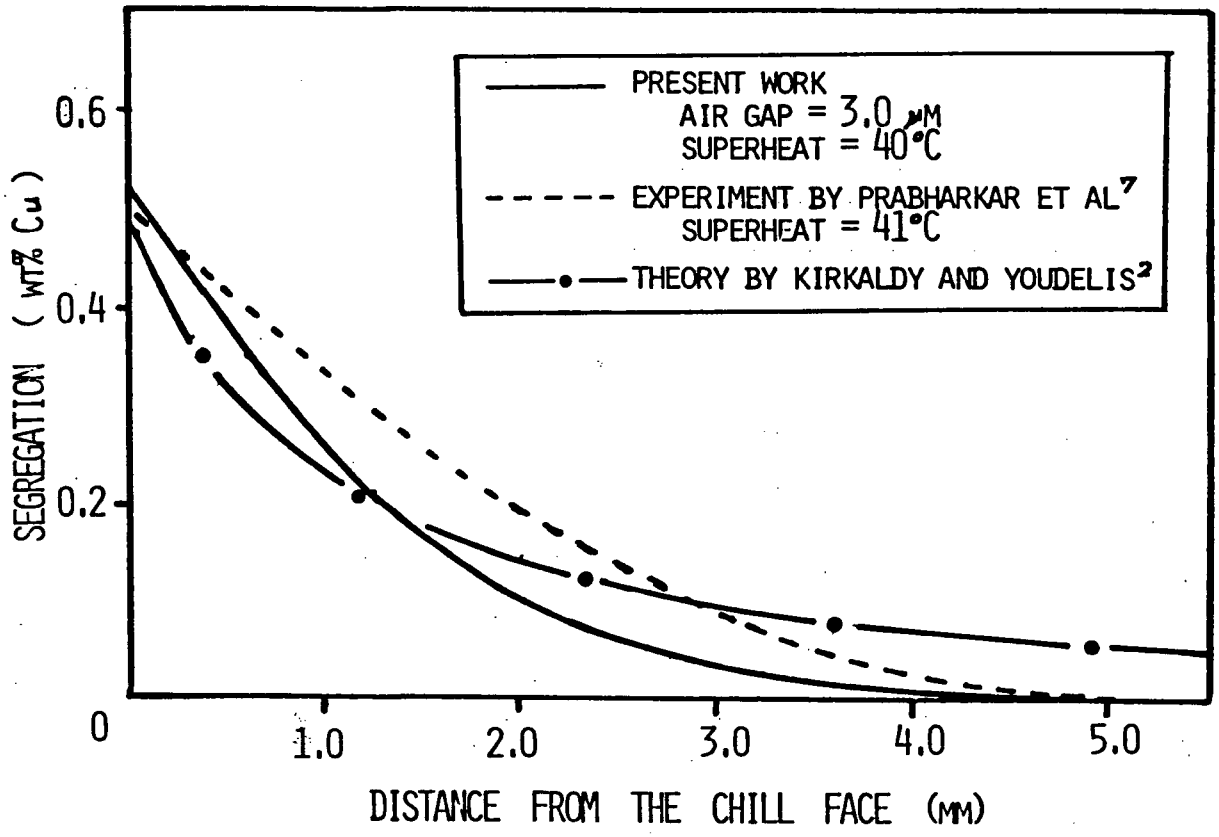

Figure 17 - Comparison of positional segregation for Al-10%Cu

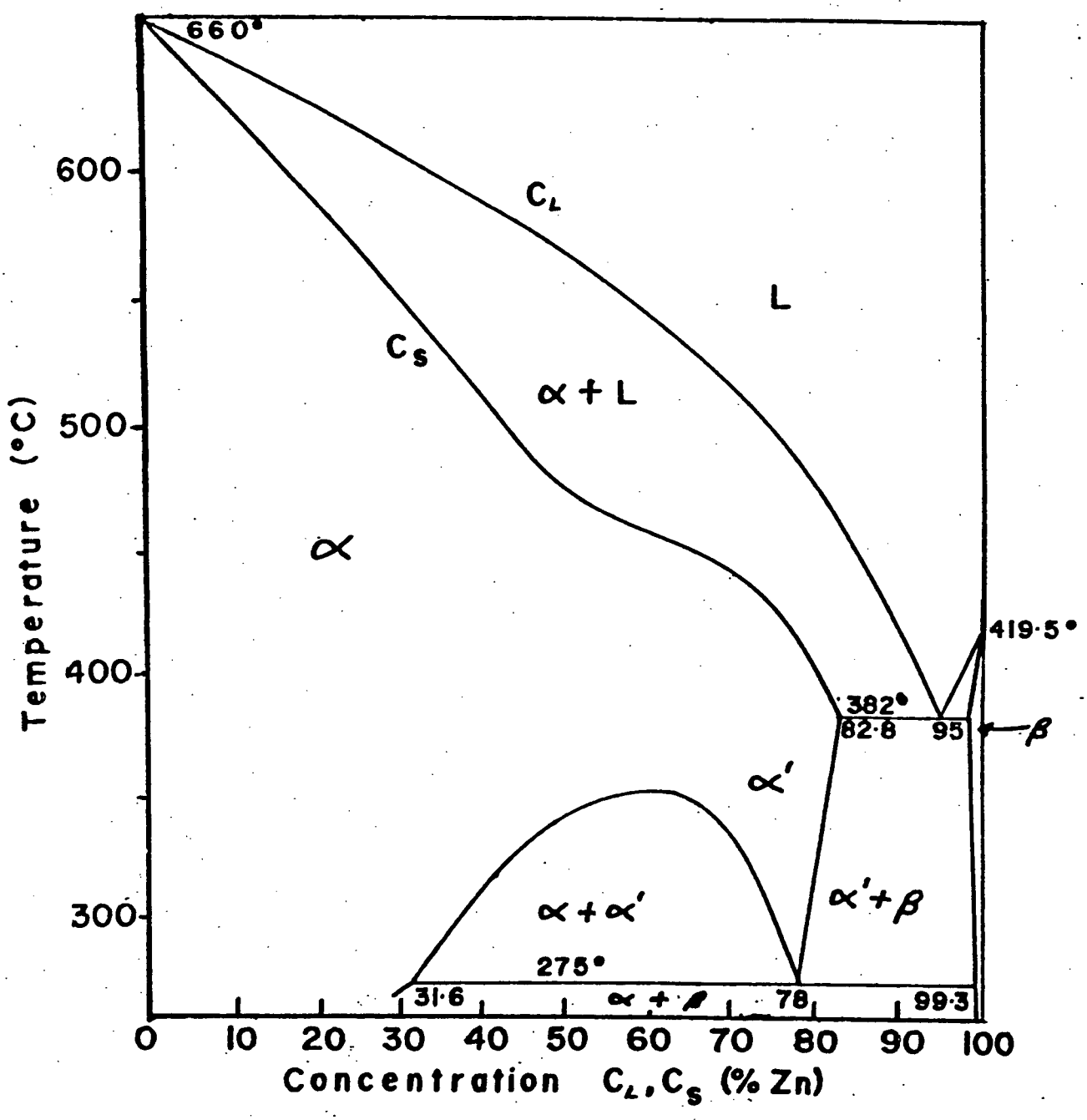

Figure 18 - Equilibrium phase diagram for Al-Zn alloys

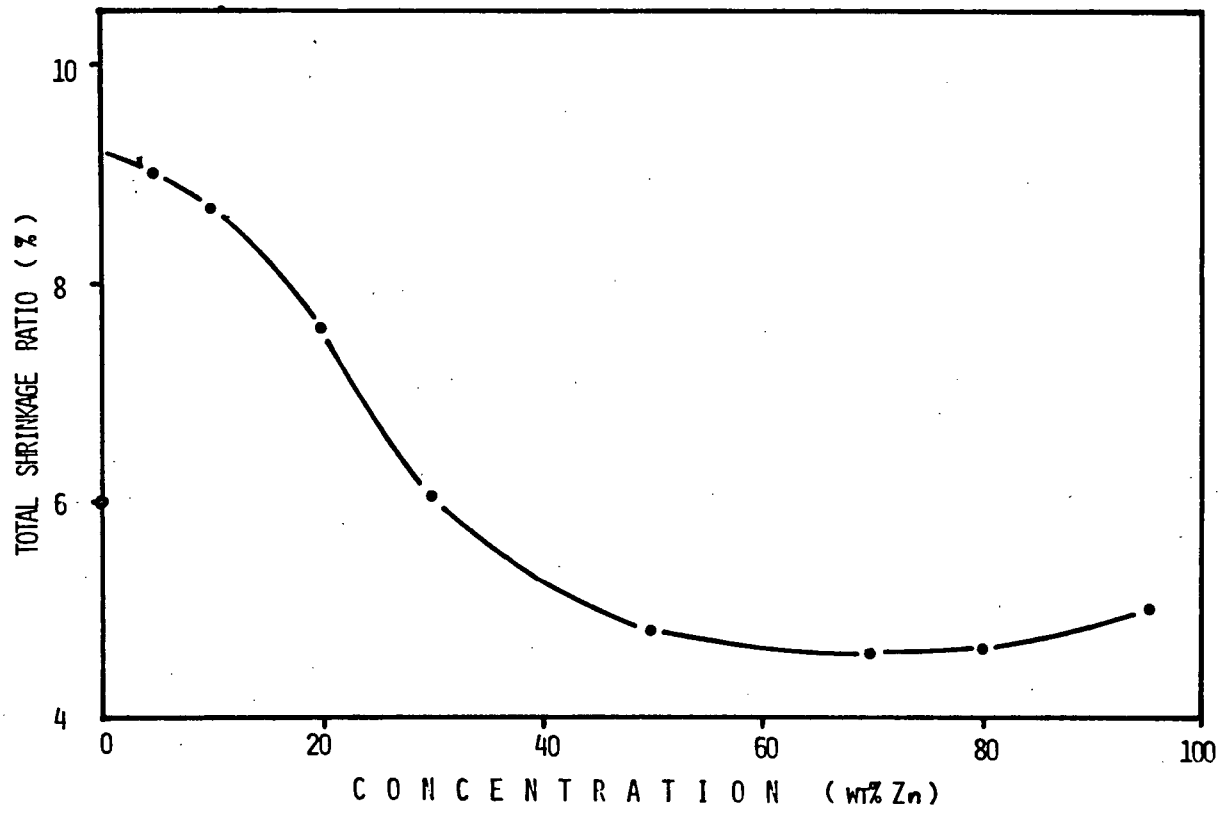

Figure 19 - Total shrinkage ratio vs composition for the Al-Zn alloys

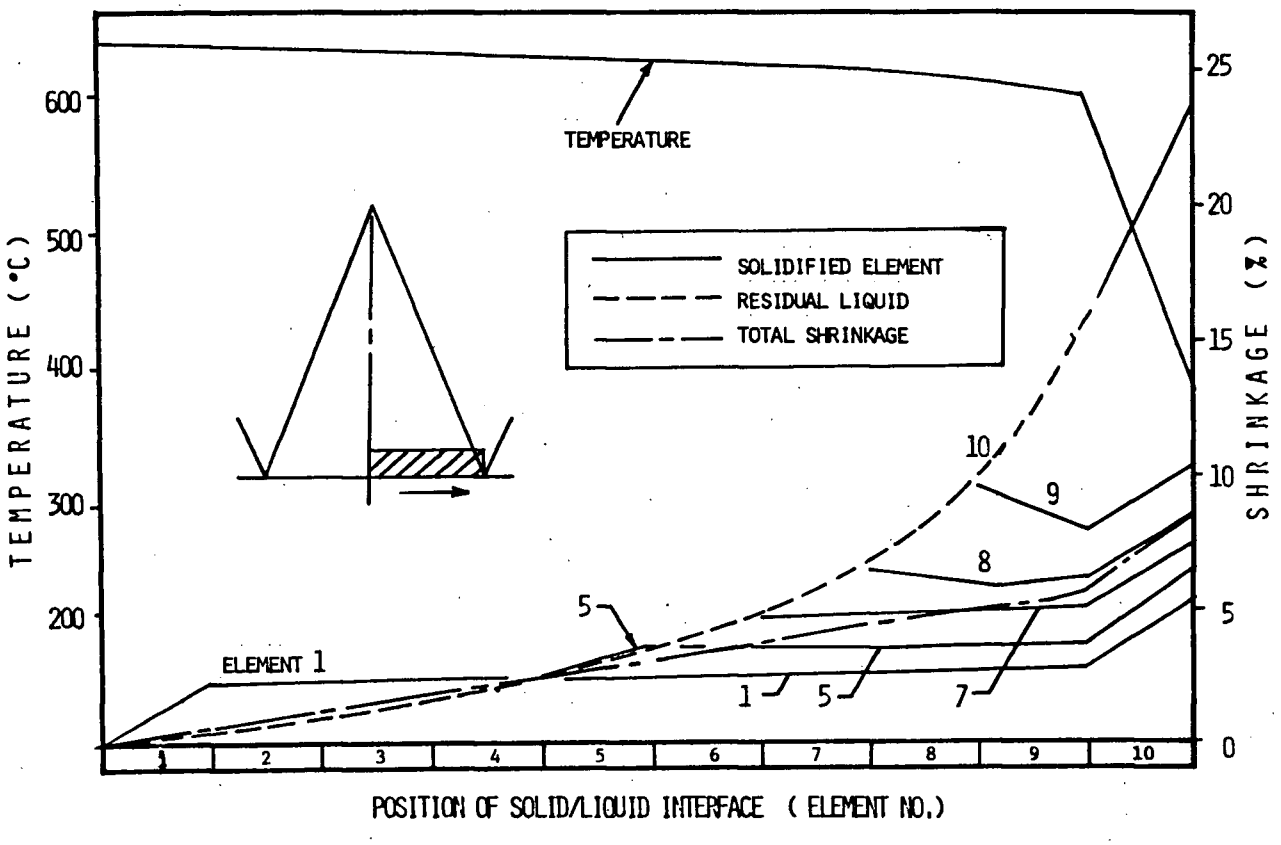

Figure 20 - Calculated volume change and temperature in the representative volume for Al-10%Zn. The number on the curve denotes each element solified.

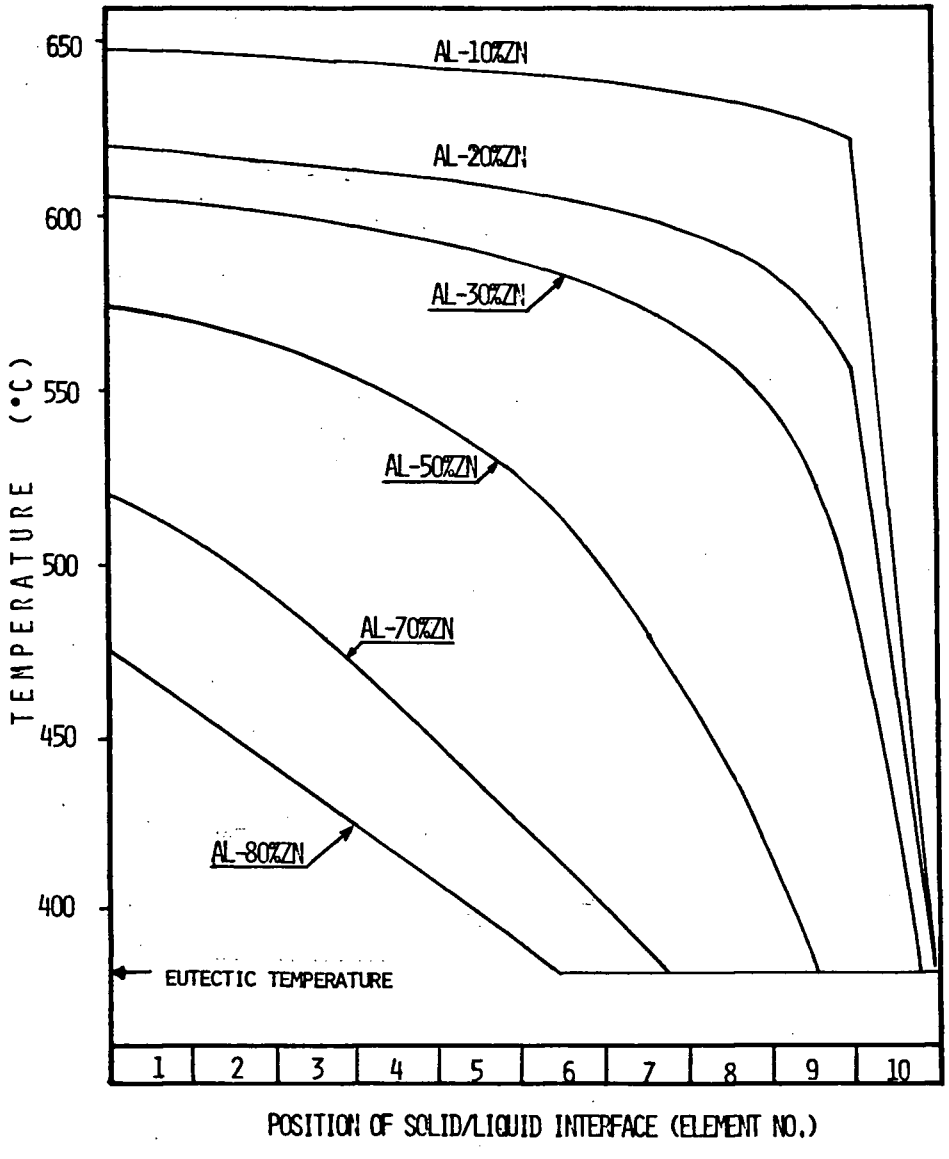

Figure 21 - Calculated profiles of temperature in the representative volume for various compositions of the Al-Zn alloys indicated.

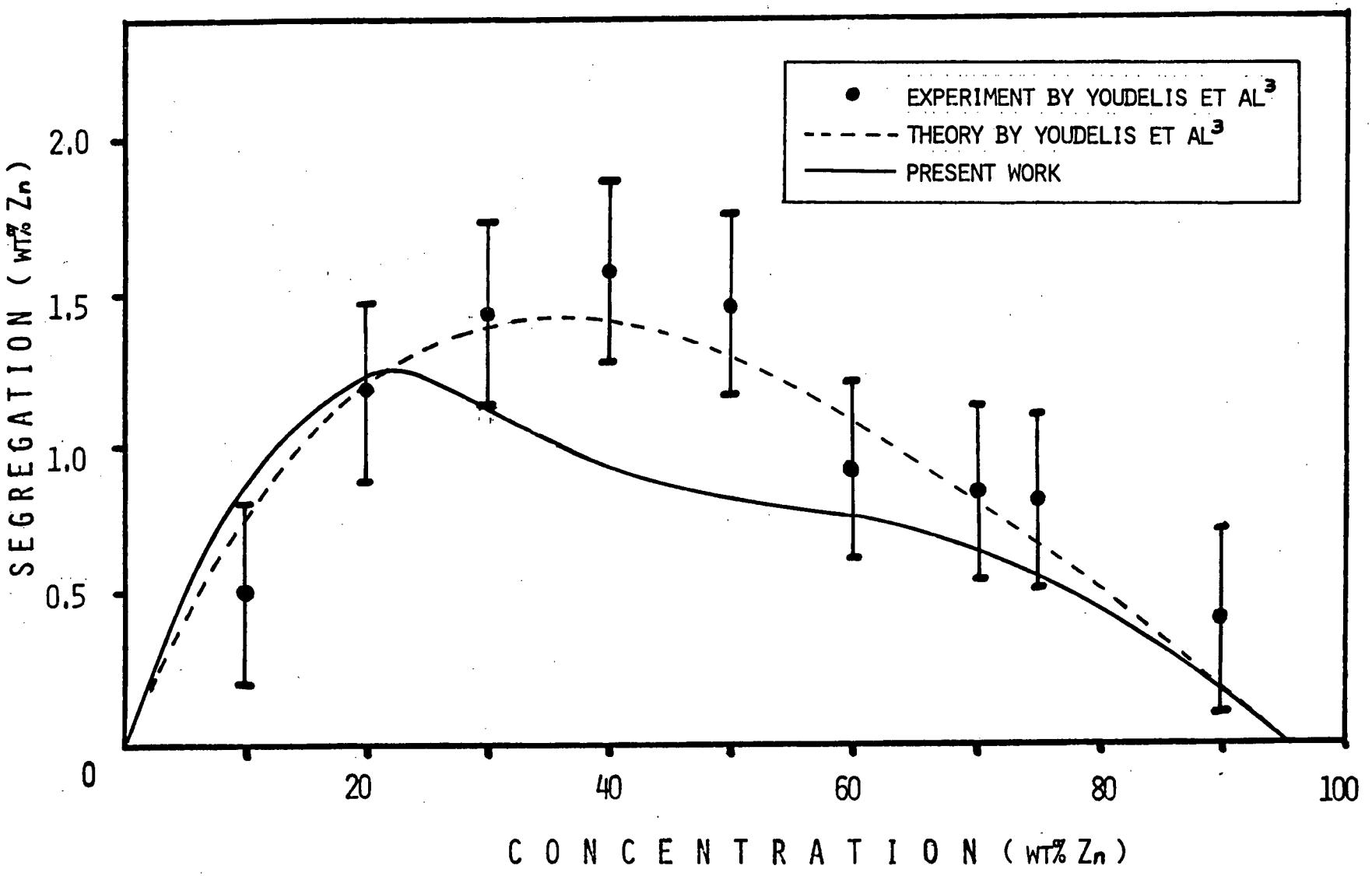

Figure 22 - Comparison of the inverse segregation at the chill face for the Al-Zn alloys

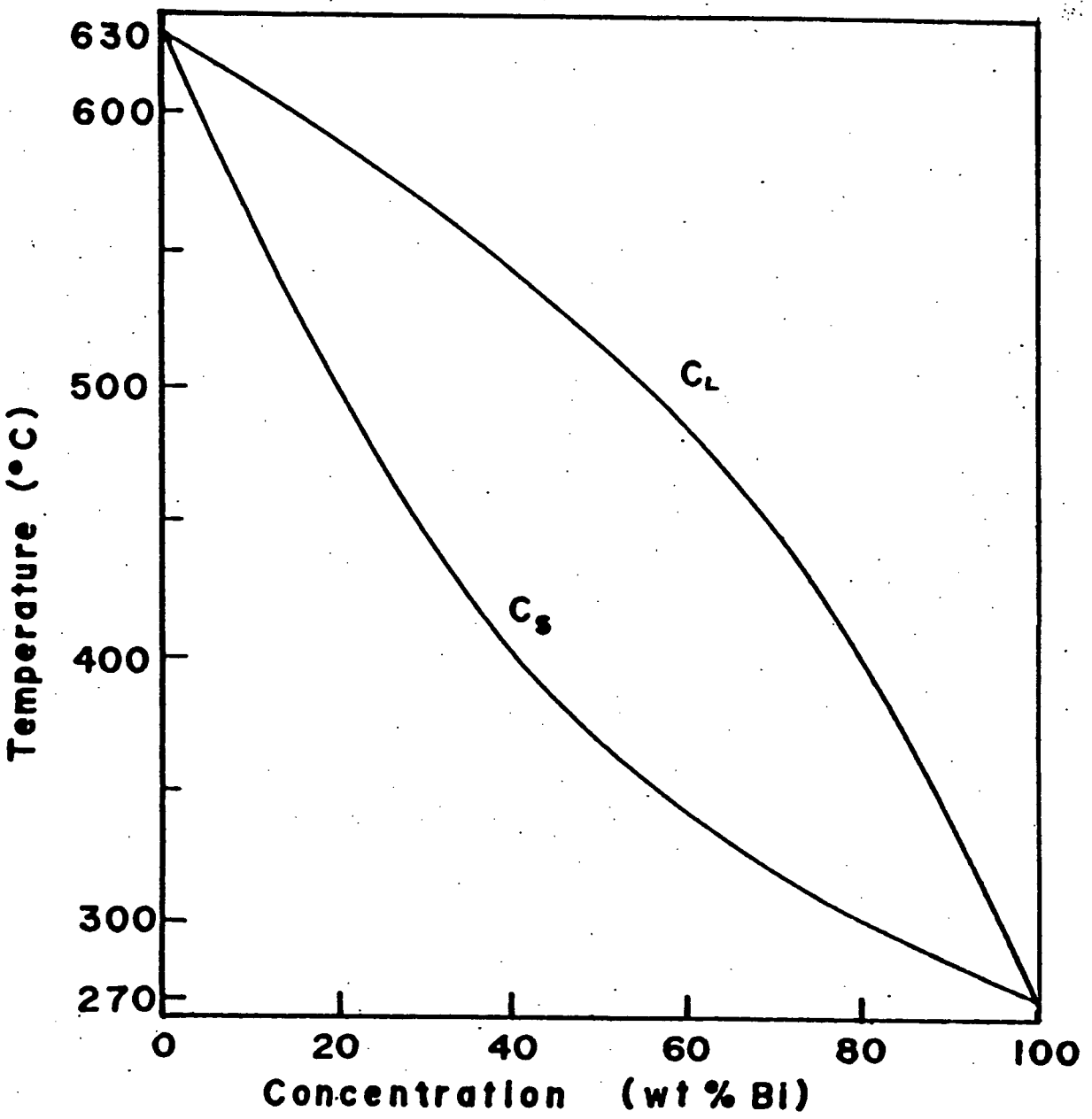

Figure 23 - Equilibrium phase diagram for Sb-Bi alloys

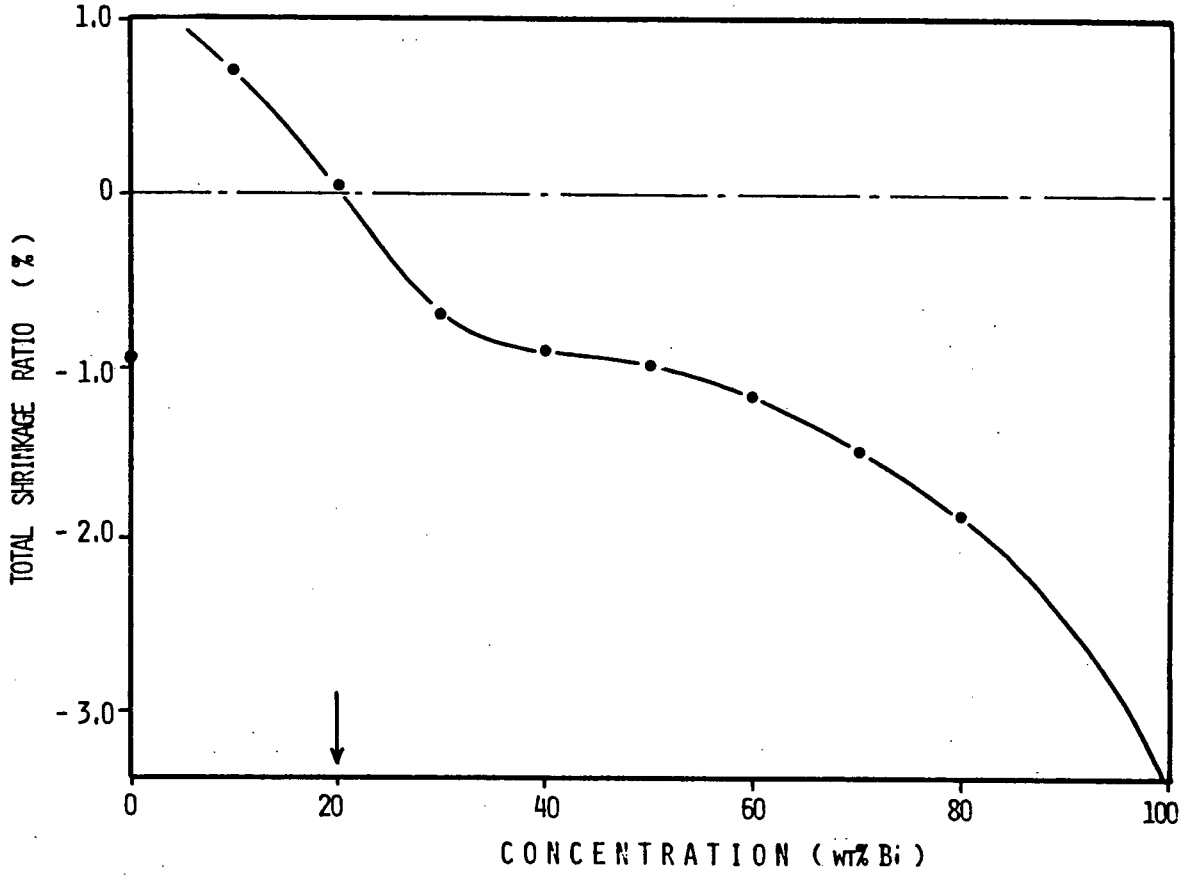

Figure 24 - Total shrinkage ratio vs composition for the Sb-Bi alloys

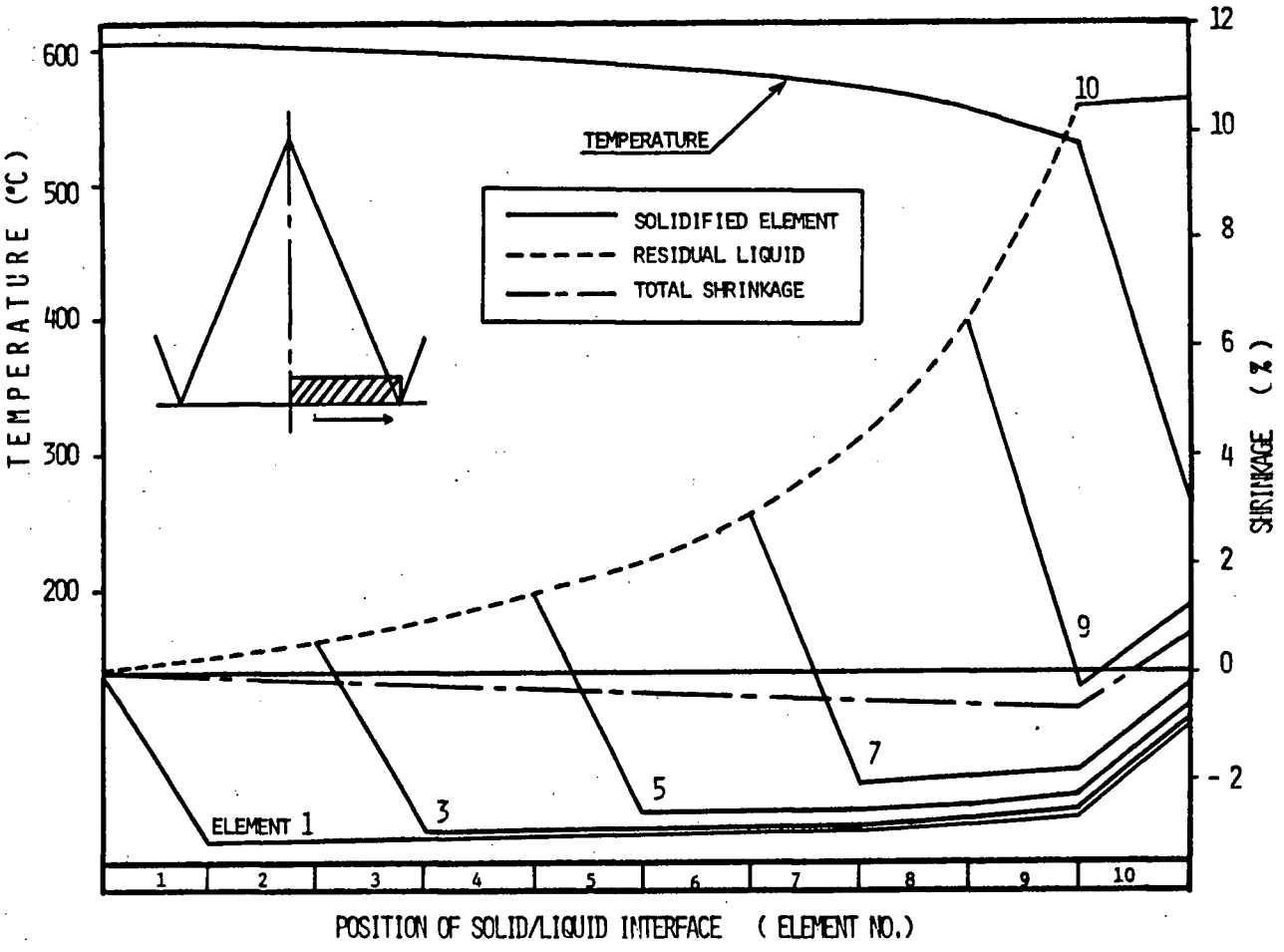

Figure 25 - Calculated volume change and temperature in the representative volume for Sb-10%Bi. The number on the curve denotes each element solidified.

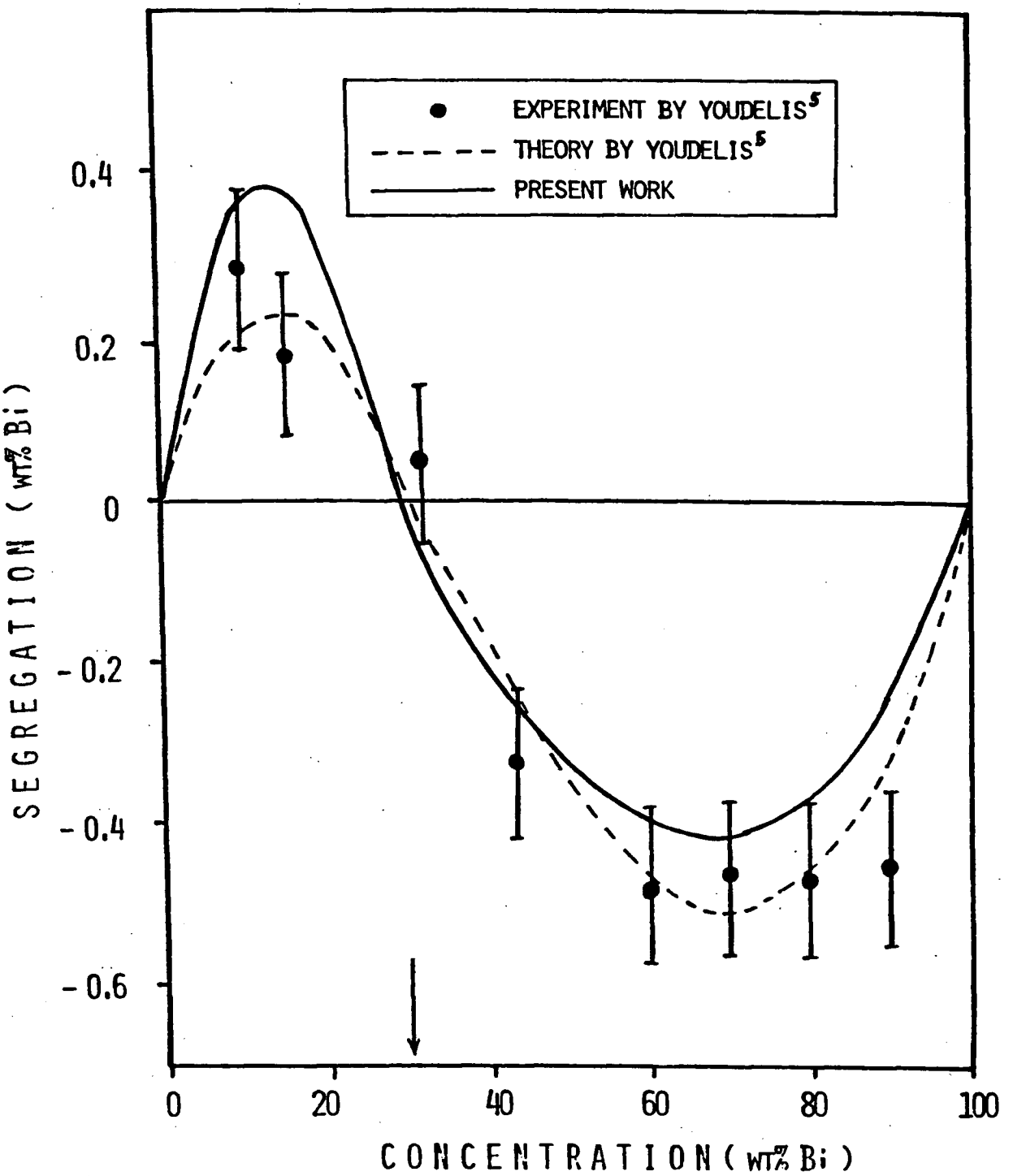

Figure 26 - Comparison of the inverse segregation at the chill face for the Sb-Bi alloys

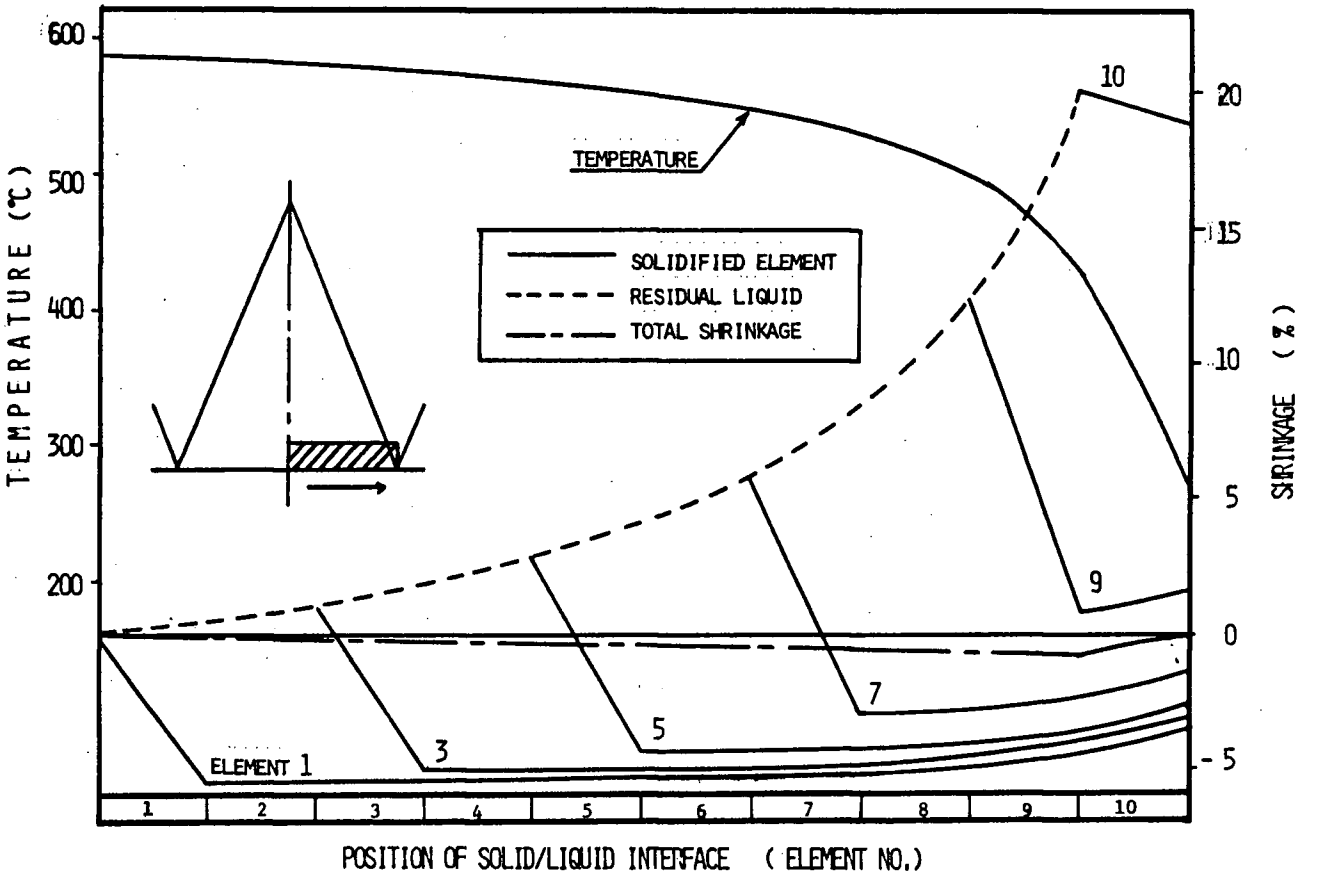

Figure 27 - Calculated volume change and temperature in the representative volume for Sb-20%Bi. The number on the curve denotes each element solidified.

PART - B

CENTERLINE SHRINKAGE IN STEEL PLATE CASTINGS

B-I. INTRODUCTION

A unique advantage of metal castings is that highly complex shapes can readily be fabricated. This inherent advantage of castings, however, is often lost because of the difficulty of controlling casting defects, among which shrinkage porosity is one of the major defects. Shrinkage porosity is controlled by proper design of the casting, using suitable gating and risering techniques and moulding materials. Since the casting process is complex, the design of these systems is only approximate and empirical so that porosity does occur in castings.

1.1 Gross Shrinkage

Recent development of the numerical simulation of the casting process[21-25] has enabled the solidification sequence of a simple casting to be calculated. Jeyarajan and Pehlke[26] applied a mathematical model to sand mold casting for the prediction of gross shrinkage in a rail wheel casting due to insufficient mass feeding. Comparing their numerical calculations with experimental observations it was found that the observed gross shrinkage cavity agreed very well with the calculations which predicted the shape and position of the last liquid to solidify. The remaining problem in predicting gross shrinkage in castings is to extend the Pehlke analysis to the

highly complex shapes used in normal foundry practice.

1.2 Centerline Shrinkage

Towards the end of solidification, the solidification shrinkage must be fed by liquid flowing down highly irregular narrow interdendritic channels. If complete back flow does not occur, small scattered interdendritic pores forms, called centerline porosity or centerline shrinkage. A heat transfer model gives isochronal solidification lines assuming simple heat flow patterns. In the later part of solidification the heat flow locally is complex and therefore uncertain when applied to the centerline porosity problem. In addition fluid flow of the interdendritic liquid must also be considered.

Pellini et al[27-30] carried out an extensive series of measurements in which the feeding distance of steel castings in green-sand moulds was determined. It was found for a plate casting, 2.5 to 5.0cm thick (Fig 28a), that:

1) the maximum plate length cast completely sound by one riser is 4.5s (s=plate thickness),
2) the length D of the end of the plate free of porosity is always 2.5s for the plate casting more than 4.5s long, and
3) the sound area due to riser effect is 2s.

Similarly the maximum length cast completely sound is 9.56 s and the sound region due to end effects is 1.5s-2s in square bar

castings with 5 to 20cm section size (Fig 28b). They also examined the effect of end chill on the feeding distance and found that chills contribute to increasing the sound region by 5cm and 1s in plate and square bar castings respectively.

Johnson and Loper[31] examined the centerline porosity of thin steel sections cast in green-sand mould. Sections studied included flat plates and square bars of thicknesses less than 2.5cm which is smaller than the range considered by Bishop et al[27,28]. They found that the maximum length which could be cast without porosity was given by $(16.1\sqrt{s}-14)$cm for plate castings and $(12.7\sqrt{s}-8.4)$cm for square bar castings.

Niyama et al[32] predicted centerline shrinkage on the bases of a numerical simulation of the process giving the isochronal contours during solidification. They showed that the temperature gradient at the end of solidification is a simple and effective parameter to predict porosity. However the critical value of the gradient in the prediction can only be determined empirically for each casting as shown by Pellini[30]. A further step was taken by Niyama et al[33] in proposing a new parameter $G/\sqrt{R}$ to predict porosity with the critical value of 1.0 $\sqrt{\text{min.}^\circ\text{C}}$/cm for this parameter, applicable to both gross and centerline porosities. This would be independent of the alloy composition and the size and shape of the steel casting considered. This has been challenged by Chijiiwa and Imafuku[34] who questioned the general applicability of this parameter. As an alternative they proposed that the gradient of fraction solid

at the end of solidification has the critical value of 0.25 per cm for centerline shrinkage. The three parameters proposed to predict porosity, G, $G/\sqrt{R}$ and the gradient of fraction solid, might be effective in predicting the formation of centerline shrinkage industrially. However, they are all effectively empirical parameters lacking a clear physical basis in which to establish a quantitative measure of the porosity in a casting.

1.3 Previous Models

Porosity is associated with feeding distance in the casting as well as the solidification structure. Feeding of liquid through interdendritic channels is considered by Davies[35] using numerical simulation. The capillary flow through a channel is given by:

$$\frac{dV}{dt} = \frac{\pi r^4}{8\mu} \frac{P}{l} \qquad \text{(B-1)}$$

The amount of liquid which must flow through the capillary to compensate for solidification contraction is:

$$\frac{dV}{dt} = v_s \pi r^2 \beta \qquad \text{(B-2)}$$

Combining equations (B-1) and (B-2), gives the capillary feeding distance, l_f,

$$l_f = \frac{Pr^2}{8\mu\beta v_s} \qquad \text{(B-3)}$$

Friction reduces the effective pressure, $P=P_o-\Delta P$, where, for

laminar flow (r<<l):

$$\Delta P = \frac{8v\mu l}{r^2} \tag{B-4}$$

The flow velocity is given by,

$$v = \beta v_s \tag{B-5}$$

Combining equations (B-3),(B-4) and (B-5) gives:

$$l_f = \frac{(P_o - \Delta P)r^2}{8\mu\beta v_s} = \frac{P_o r^2}{8\mu\beta v_s} - 1 \tag{B-6}$$

When shrinkage appears, $l=l_f$ and:

$$l_f = \frac{P_o r^2}{16\mu\beta v_s} \tag{B-7}$$

The capillary feeding distance was calculated using equation (B-7), incorporating an empirical correction factor B which includes the factors that are difficult to consider:

$$l_f = \frac{BYP_L r^2}{\mu\beta v_s} \tag{B-8}$$

The correction factor, B, was chosen to be 0.22 in order that the calculated feeding distance for a steel plate cast in green sand mould has a feeding distance equal to that empirically determined value of $4.5s^{30}$.

Based on the type of alloy, assumptions were made for the fraction solid at which porosity due to incomplete feeding would occur. For example, Davies[35] estimated that incomplete feeding could occur above solid fractions of 95%, for 0.6%C steels and 99.8%Al; above solid fraction of 90% for nodular cast iron and 99% for pure Al. The above model (Davies') was applied to a wide range of materials and good agreement was obtained between

the calculated results and the experimentally determined values.

Shortcomings in the Davies' model are that an empirical correction factor B is included in the model, and the assumption of when incomplete feeding starts which strongly influences the presence of centerline shrinkage. The value for B used in fitting the model to experimental results was derived from the experiments on cast steel. One would expect different values for B would be required for other materials since B in equation (B-8) involves a lot of factors not involved in his model.

Another theoretical model for porosity was proposed by Flemings[36] incorporating Darcy's Law for interdendritic fluid flow. Assuming that the mold/metal interface resistance is of overriding importance and that the mold, being infinite in extent, remains at its initial temperature (T_o), the rate of heat flow across this interface is:

$$q = -h(T-T_o) \tag{B-9}$$

The heat entering the mold comes nearly entirely from the heat of fusion of the solidifying metal. Thus:

$$q = (\rho_s H_s) \frac{V_c}{A_c} \frac{\partial g_L}{\partial t} \tag{B-10}$$

Combining equation (B-9) with (B-10) gives:

$$\frac{\partial g_L}{\partial t} = -c \tag{B-11}$$

where $\Delta T=T-T_o$ and c is a constant. Since the heat flow is controlled by the heat transfer coefficient h, there is no significant thermal gradient in the solidifying metal and $\partial g_L/\partial t$ is independent of position in the casting. Darcy's law is given

by:

$$\vec{v} = - \frac{K}{\mu g_L} (\nabla P + \rho_L g_r) \qquad \text{(B-12)}$$

For one dimensional fluid flow, equation (B-12) reduces to:

$$v_x = - \frac{K}{\mu g_L} \left(\frac{dP}{dx} + \rho_L g_r \right) \qquad \text{(B-13)}$$

Similarly, the mass balance equation in the volume element, equation (A-13), reduces to:

$$\frac{\partial \bar{\rho}}{\partial t} = - \frac{\partial}{\partial x} (\rho_L g_L v_x) \qquad \text{(B-14)}$$

where

$$\bar{\rho} = \rho_s g_s + \rho_L g_L \qquad \text{(B-15)}$$

Equation (B-15) is rearranged for constant densities in liquid and solid as:

$$\frac{\partial \bar{\rho}}{\partial t} = - (\rho_s - \rho_L) \frac{\partial g_L}{\partial t} \qquad \text{(B-16)}$$

Equations (B-11), (B-14) and (B-16) yield,

$$\frac{\partial}{\partial x} (g_L v_x) = - \frac{\beta}{1-\beta} c \qquad \text{(B-17)}$$

Since g_L is independent of position, integrating equation (B-17) gives the interdendritic flow velocity as a function of position;

$$v_x = - \frac{\beta}{1-\beta} \frac{cx}{g_L} \qquad \text{(B-18)}$$

Substituting equation (B-18) into equation (B-13)

and integrating yields the pressure at x;

$$P = P_a + \frac{\beta}{1-\beta}\frac{c\mu}{2K}(D^2 - x^2) + \rho_L g_r Y \qquad \text{(B-19)}$$

This expression is theoretically enough to describe the formation of centerline shrinkage, but is valid only for the system with homogeneous temperature all over the casting and without superheat, which is not satisfied under normal casting conditions.

1.4 Permeability

Towards the end of solidification when the fraction solid in the alloy is high, fluid flow to compensate for volume shrinkage occurs through narrow tortuous interdendritic channels. This flow is analogous to flow through packed beds and, if the flow occurs under low pressure conditions, the flow rate will obey the "Darcy's Law" expressed in equation (B-12). For one dimensional fluid flow without a metallostatic head, equation (B-12) reduces to:

$$v' = -\frac{K}{\mu}\frac{\Delta P}{l} \qquad \text{(B-20)}$$

where v' is superficial flow velocity and

$$v' = g_L v_x \qquad \text{(B-21)}$$

Flow velocities through a straight capillary tube are given by

Hargen-Poisulle's equation:

$$\frac{dV}{dt} = - \frac{\pi r^4}{8\mu} \frac{\Delta P}{1} \qquad \text{(B-22)}$$

Introducing a "tortuosity factor, τ" in the case where the capillary is not straight and for n capillaries per unit area:

$$v' = - \frac{n\pi r^4}{8\mu} \frac{\Delta P}{\tau 1} \qquad \text{(B-23)}$$

Equating equations (B-20) and (B-23):

$$K = \frac{n\pi r^4}{8\tau} \qquad \text{(B-24)}$$

and from geometry:

$$g_L = n\pi r^2 \tau \qquad \text{(B-25)}$$

rearranging gives:

$$r^4 = \frac{g_L^2}{n^2 \pi^2 \tau^2} \qquad \text{(B-26)}$$

Substituting equation (B-26) into (B-24) yields:

$$K = \frac{g_L^2}{8n\pi\tau^3} \qquad \text{(B-27)}$$

This shows that for a given dendrite morphology, the permeability is directly proportional to the square of the volume fraction liquid[37-39].

The verification of equation (B-27) was first attempted by Piwonka and Flemings[37] using Al-4.5%Cu porous media and molten lead. The theory predicts ln(K) is proportional to ln(g_L) for constant τ with a slope of 2. This was found to be the case experimentally when the fraction liquid was less than 0.3. Apelian, Flemings and Mehrabian[40] noted that the permeability in equation (B-27) is inversely proportional to the number of flow

channels per unit area. They compared K values of Al-4%Si with those of Al-4%Si-0.25%Ti, and found that the permeability is consistently lower for the grain refined alloy, the latter, which has more capillaries in a unit area.

Interdendritic fluid flow was carefully measured by Streat and Weinberg[39] in a partially solidfied columnar dendritic casting. Assuming the number of flow channels in the casting is equal to the number of channels between the columnar primary dendrite branches and the spacing between these channels equals the primary dendrite arm spacing, equation (B-27) is reduced to:

$$K = \frac{g_L^2 (DAS)^2}{8\pi\tau^3} \qquad \text{(B-28)}$$

Measurements of permeability for a wide range of dendrite arm spacing and a constant fraction liquid, 0.19, showed the permeability K obeys equation (B-28) during the early part of interdendritic flow. After flow has occured the flow rate changes due to the interaction of the flowing liquid with the dendrite which changes the size and configuration of the channels. However deviation from equation (B-28) in the system examined occured after a relatively long time period, in comparison with the solidification times associated with a normal casting.

Values of permeability as a function of fraction liquid reported in the literature are summarized in Fig 29. The results show that equation (B-27) is valid for interdendritic fluid flow under steady state conditions for volume liquid

fractions less than about 0.3.

1.5 Present Objectives

Even though shrinkage porosity is a major factor in the quality of a casting, no analytical method has been developed which clearly predicts whether centerline shrinkage will occur in a casting. This is primarily because the mechanism for centerline porosity is complex, governed by interdendritic fluid flow. To predict the formation of centerline shrinkage, a proper mathematical simulation is required combining a heat transfer model with an interdendritic fluid flow model.

B-II. MODELLING PROCEDURE

The formation of centerline shrinkage is associated with insufficient flow of interdendritic liquid to compensate for solidification shrinkage. The mathematical model, therefore, has to involve both heat transfer and fluid flow.

2.1 Mathematical Formulation

2.1.1 Temperature Calculations

The casting and sand mold geometry investigated is shown in Fig 30. The riser was chosen to be the same size as the one used in the experiments reported by Pellini et al[27,30], that is 3s wide and 5s high. This riser size is large enough to avoid gross shrinkages in the plate casting.

The basic mathematical relation used to calculate the temperature distribution in the system was the general equation that governs heat conduction in a solid;

$$\rho C_p \left(\frac{\partial T}{\partial t}\right) = \nabla \cdot (k \Delta T) \qquad \text{(B-29)}$$

For constant heat conductivity and two dimensional heat flow, equation (B-29)reduces to;

$$\frac{\partial T}{\partial t} = \alpha \left(\frac{\partial^2 T}{\partial x^2} + \frac{\partial^2 T}{\partial y^2}\right) \qquad \text{(B-30)}$$

Several key assumptions concerning the casting process are

required to adjust equation (B-30) to a form suitable for numerical solution;

1) The mold is instantaneously filled with liquid metal at the pouring temperature.
2) Once the mold is filled, the liquid metal is stagnant.
3) The thermal contact resistance at the sand/metal interface is negligible.
4) Segregation in the solid and solute enrichment in the liquid are negligible.
5) The latent heat of solidification is released uniformly between the liquidus and solidus temperatures.
6) Liquidus and solidus are linear functions of temperature so that the weight fraction solidified is given by,

$$f_s = \frac{T_L - T}{T_L - T_s} \tag{B-31}$$

The initial conditions at t=0 are,

$$T_M = T_p \tag{B-32}$$

$$T_s = T_o \tag{B-33}$$

The boundary condition at the vertical sand mold surface is:

$$-k_s\left(\frac{\partial T_s}{\partial x}\right) = h_s(T_s - T_a) \tag{B-34}$$

and at the horizontal mold surface is:

$$-k_s\left(\frac{\partial T_s}{\partial y}\right) = h_s(T_s - T_a) \tag{B-35}$$

and at metal surface is:

$$-k_M\left(\frac{\partial T_M}{\partial y}\right) = h_M(T_M - T_a) \tag{B-36}$$

Convective heat transfer from the metal to ambient air is

neglected giving

$$h_M = \sigma \varepsilon \frac{(T_M + 273)^4 - (T_a + 273)^4}{T_M - T_a} \qquad \text{(B-37)}$$

There is continuity of heat flux across the sand/metal interface, which is expressed at the vertical interface by

$$k_s \left(\frac{\partial T_s}{\partial x}\right) = k_M \left(\frac{\partial T_M}{\partial x}\right) \qquad \text{(B-38)}$$

and at the horizontal interface by;

$$k_s \left(\frac{\partial T_s}{\partial y}\right) = k_M \left(\frac{\partial T_M}{\partial y}\right) \qquad \text{(B-39)}$$

2.1.2 Pressure Required To Feed Shrinkage

It has been shown in the literature[38,40,41] that interdendritic fluid flow obeys Darcy's Law at steady state when the volume fraction liquid is less than 0.3. To calculate the pressure drop due to interdendritic fluid flow in solidifying casting, Darcy's Law was applied along the centerline of the plate on the assumptions that the Law is also valid for the flow through the media with higher liquid fraction than 0.3 and for a temperature gradient present in the alloy. The governing equation without a metallostatic head is,

$$v_x = - \frac{K}{\mu g_L} \frac{dP}{dx} \qquad \text{(B-40)}$$

rearranging gives,

$$dP = - \frac{\mu g_L dx}{K} v_x \qquad \text{(B-41)}$$

where μ is constant, K is given in Fig 29, and g_L can be calculated from,

$$g_L = \frac{(1-f_s)/\rho_L}{f_s/\rho_s + (1-f_s)/\rho_L} \qquad \text{(B-42)}$$

Equation (B-41) expresses a pressure drop within an infinitesimal element as a function of fluid velocity.

The boundary condition for equation (B-41) appears at solid/liquid interface where, if the shrinkage is fed by the liquid, the rate of pore formation is equal to the rate of fluid flow. This gives:

$$(v_s A g_L)\beta = -v_x A g_L \qquad \text{(B-43)}$$

yielding,

$$v_x = - v_s \beta \qquad \text{(B-44)}$$

and the continuity of fluid flow gives,

$$v_x g_L = \text{a constant} \qquad \text{(B-45)}$$

The total pressure drop, calculated by,

$$\Delta P = \sum_j \Delta P_j \qquad \text{(B-46)}$$

denotes the pressure required to feed the solidification shrinkage. Shrinkage porosity will form when the total pressure required to feed the shrinkage exceeds the pressure acting on the system, that is the atmospheric pressure plus the metallostatic head pressure.

2.2 Computer Programming

The explicit finite difference method is used for the solution of heat transfer equations since a small time step is required to calculate small changes during solidification. The derivation of the nodal equation is given in Appendix B. The calculation was first performed to determine the temperature distribution and then to determine the pressure drop. Values of permeability were taken from the Piwonka and Flemings[37] data in Fig 29 since they cover a wide range of liquid fraction, which is required in the present case.

The actual calculation sequence used is shown in the flow chart, Fig 31, and a sample of the Fortran program is given in Appendix C. The computer program also involves the calculation of temperature gradient and the solidification parameter, $G/\sqrt{R}$, at the end of solidification.

2.3 Validation Of The Heat Transfer Model

To validate the present model for calculating the temperature distribution in the casting, some calculations were performed and the results were compared to the experimental measurements of Bishop and Pellini[27]. Fig 32 shows typical calculated values for the temperature distributions along the centerline at different time intervals after pouring, for the

plate casting with 5cm thick and 33cm long. Also plotted in the figures are the temperature profiles determined experimentally. The measured liquidus and solidus temperatures for the low carbon steel, having the following composition Fe-0.34%C-0.68%Si-0.89%Mn were 1507°C and 1463°C respectively. Reasonable agreement can be observed between the model predictions and the experimental results over the entire length of the plate, except at positions close to the end surface and to the riser. The predicted temperatures are quite accurate especially in the region of the liquid/solid co-existing zone which is most relevant to the formation of centerline shrinkage. It will be noted from the curves in Fig 32 that the temperature gradients, established soon after solidification starts by heat flow into the plate from the riser and heat losses at the end of the plate, tend to progress toward each other during solidification.

The movement of the solidus temperature along the centerline is shown in Fig 33. The calculated values are in good agreement with the measured temperature profiles except for a small deviation. The freezing rate, given by the slope of the curve in Fig 33 is observed to be very rapid in the central region of the casting and relatively slow at either end.

Values of the physical properties used in the above calculations are listed in Table III together with other physical data for the calculation of pressure drop due to interdendritic fluid flow.

B-III. RESULTS AND DISCUSSION

The mathematical model described in the previous section was applied to a range of steel plates of different size, to predict the formation of centerline shrinkage. Calcuations were also carried out to evaluate the effect of the end chill on the casting soundness. Table IV lists the plates sizes considered.

3.1 Solidification Sequence

The temperature distribution along the centerline, Fig 32, can be divided into three parts. These are the riser end with a relatively steep temperature gradient, the centre with effectively zero temperature gradient and the plate end where the temperature gradient is again steep. The centerline shrinkage must form in the central region where directional solidification does not occur.

Typical contour lines during solidification determined from the model are shown in Fig 34. The vertical dotted lines indicate the critical points for the formation of centerline shrinkage determined experimentally by Bishop and Pellini[28]. At the intial stage of solidification (Fig 34a) contour line corresponding to 70% solid projects out along the centerline of the plate toward the solidus. The remaining liquid within the 70% solid region will contain interdendritic channels broad

enough to feed the solidification contraction at the bottom of solid/liquid region. At the middle stage of solidification (Fig 34b), the solidus still projects out along the centerline whereas the 70% and 90% contour lines move back toward the riser end of the casting. The region between 90% solid and the solidus contains little liquid making it very difficult for liquid to flow through the existing channel to feed volume shrinkage at the solidus along the centerline. The bottom of the solid/liquid region is located in the area where centerline shrinkage was found experimentally[27]. Near the end of solidification the solidus and 70% solid contour line approach each other (Fig 34c). Thus, the shape and position of the solidification contour lines indicate whether centerline porosity is likely to occur. However the contour line configuration cannot quantitatively predict the region along the centerline where shrinkage porosity will occur.

3.2 Prediction Of Centerline Shrinkage

The calculated pressure required to feed the shrinkage along the centerline for a 5cm thick plate casting is shown in Fig 35. The pressure acting on the system is defined as the sum of atmospheric pressure and the metallostatic head pressure. When the pressure required to feed the shrinkage formed at the end of solidification is greater than the pressure acting on the system, the shrinkage will not be fed completely.

The pressure required to feed a 4.6s(23cm) long casting is always less than that acting on the system. The pressure required to feed long castings, greater than 4.8s(24cm) is greater than the acting pressure. The maximum length which can be cast completely sound using one riser, determined from the model, is 4.7s for 5cm thick plate. This value agrees well with the experimentally determined value of 4.5s[30]. In Fig 35 the sound region determined experimentally adjacent to the free end of the plate is shown for castings greater than 4.8s in length. The length free of porosity shown in the figure ranges from 2.35s to 2.7s, which agrees well with the experimental value of 2.5s[30]. Of particular interest is that the maximum required pressure increases exponentially with casting length. If the casting was subjected to 2 atmosphere pressure during solidification, for example, the effect would be small, increasing the region free of porosity by 0.2s(1cm).

Calculated profiles of the pressure required to feed shrinkage along the centerline of 2.5 and 0.5cm thick plate castings are shown in Figs 36 and 37, respectively. The pressure profiles for both plate thickness are similar to those in Fig 35. It is found for 2.5cm thick plate that the maximum casting length which is free of porosity is 4.6s and that the sound region at the free end of the plate is 2.5s to 2.7s. These values agree with experimental data, 4.5s and 2.5s respectively. For 0.5cm thick casting (Fig 37), the maximum sound length is also 4.6s. There is no indication that the maximum feeding distance to thickness ratio decreases with a

decrease in plate thickness in the region less than 2.5cm, as Johnson and Loper reported[31].

Predicted maximum feeding distances are plotted against plate thickness in Fig 38. Experimental results of the maximum feeding distances are also plotted in the figure[27,31]. For plates which are thicker than 2cm the agreement between the calculated and measured values is excellent. For the plates thinner than 2cm the experimental values of the feeding distances are less than those predicted. This can be accounted for by the large drop in temperature of the liquid metal at the free end of the plate as the liquid metal is filling the mold during pouring. This temperature drop is not considered in the present model. The rapid cooling at the end lowers the effective superheat of the melt and effectively reduces the feeding distance.

9.3 The Effect of an End Chill on the Length of the Porosity Free Region

The contribution of an end chill to increasing the sound region in a plate casting was also examined by applying a steel chill at the casting end of a 5cm thick plate. The chill size, 5cm thick, was chosen since it is reported by Myscowski et al[29] that 1s chills are of sufficient thickness for plate castings when its cross section is the same as that of the castings (Fig 30).

The calculated pressures for the casting with an end chill as a function of distance from the edge along the centerline is shown in Fig 39. Comparing this figure to Fig 35, the maximum pressure in this case is shifted towards the riser because of the chill. The maximum length of the plate cast sound is 5.7s and the sound region due to end and chill effect is approximately 3.5s. This shows that the end chill increases the sound region by 1s (5cm) which coincides with the value, 5cm determined experimentally. This distance is relatively small, indicating that end chills will not signficantly improve the soundness of plates cast in sand molds.

3.4 Proposed Solidification Parameters Defining the Transition from Porous to Nonporous Castings

As described in the previous section three solidification parameters have been proposed to define when centerline porosity will occur in a casting. These are the temperature gradient (G)[30], the temperature gradient divided by the square root of cooling rate $(G/\sqrt{R})$[33] and the gradient of fraction solid (P_{II})[35]. These parameters were calculated in the present computer program (Fig 31) and the critical values for centerline shrinkage were obtained as the values at the position corresponding to the boundary for centerline shrinkage predicted by the present model. The critical values for each parameter are listed in Table V for each plate thickness. The critical

values of both G and P_{II} are observed to change with plate thickness. The proposed values are not applicable generally. On the other hand, the critical values for $(G/\sqrt{R})$ are very close to the proposed value, unity, independent of casting size in the range examined. Accordingly, the parameter $G/\sqrt{R}$ is a simple and effective parameter to predict roughly the location of centreline shrinkage in a plate casting.

B-IV. CONCLUSIONS

The location of centreline porosity in the plates cast in sand molds has been examined using calculated values of the thermal field during solidification and Darcy's Law to define the interdendritic fluid flow. The calculations were compared with experimental results reported in the literature from which the following conclusions may be made.

1) There is good agreement between the calculated and observed values of centreline porosity. This clearly indicates the centreline shrinkage can be attributed to insufficient interdendritic fluid flow to feed the volume contraction during solidification.
2) Darcy's Law can be used to calculate the interdendritic fluid flow in a casting even though the system is not at steady state during flow.
3) The pressure required to produce a sound plate casting increases exponentially as the casting length is increased. As a result casting under pressure will not appreciably reduce centreline porosity.

Table III - Physical data employed in calculations

	Steel	Mold
specific heat, Cp (cal/g°C)	0.20	0.25
density of liquid, ρl (g/cm^3)	7.10	
density of solid, ρs (g/cm^3)	7.50	1.65
thermal conductivity, k (cal/cm.s.°C)	0.074	0.0037
heat transfer coefficient, hs (cal/cm^2.s.°C)		$5.0X10^{-4}$
latent heat of solidification, Hs (cal/g)	65.0	
solidification shrinkage ratio, β	0.03	
liquidus temperature, Tl (°C)	1507	
solidus temperature, Ts (°C)	1463	
pouring temperature, Tp (°C)	1595	
initial temperature, To (°C)		20
emissivity, ϵ	0.45	
viscosity of liquid, μ (poise)	0.05	
ambient temperature, Ta (°C)	20	

Table IV- Dimenstion of the steel plate casting examined

thickness(cm)	length (cm)
s=5.0	4.6s, 4.8s, 5.0s, 6.6s, 9.0s, 12.0s
2.5	4.4s, 4.6s, 4.8s, 5.0s, 6.6s
1.25	4.4s, 4.6s, 5.0s, 6.6s,
0.5	4.0s, 4.4s, 4.6s, 4.8s, 5.8s
5.0[1]	5.6s, 5.8s, 6.6s, 9.0s

Note: 1. end chilled by 5cm thick steel

Table V - Comparison of the critical values of solidfication parameters for centerline shrinkage

parameters	proposed value	obtained values for each plate thickness			
		5cm	2.5cm	1.25cm	0.5cm
G(°C/cm)	0.22-0.44[31]	1.8-2.2	3.6-4.4	6.6-8.0	14.6-19.7
P_I ($\sqrt{min}$°C/cm)	1.0[34]	0.92-1.10	0.93-1.08	0.83-0.98	0.94-1.07
P_{II} (1/cm)	0.25[35]	0.037-0.042	0.072-0.082	0.12-0.14	0.37-0.41

Note: $P_I = G/\sqrt{R}$

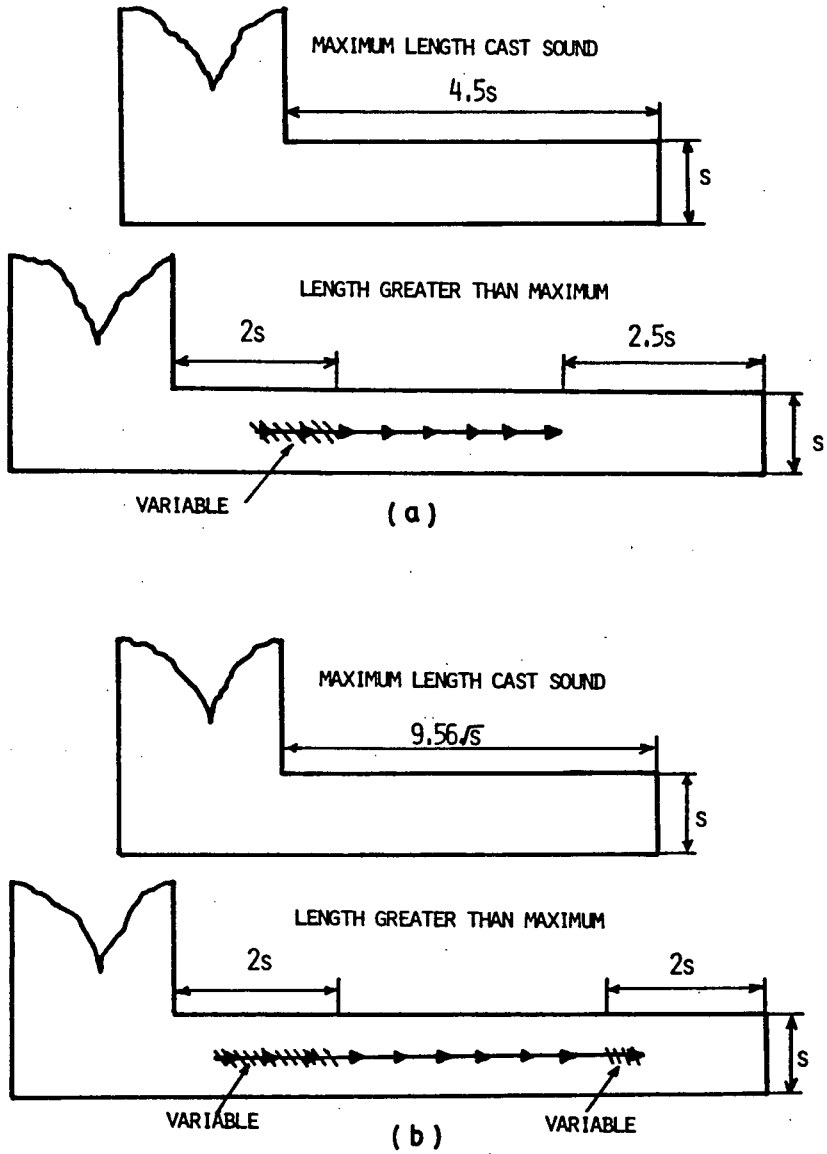

Figure 28 - Feeding relationship determined experimentally in the steel castings; (a) Plates[30], and (b) Square bars[31]

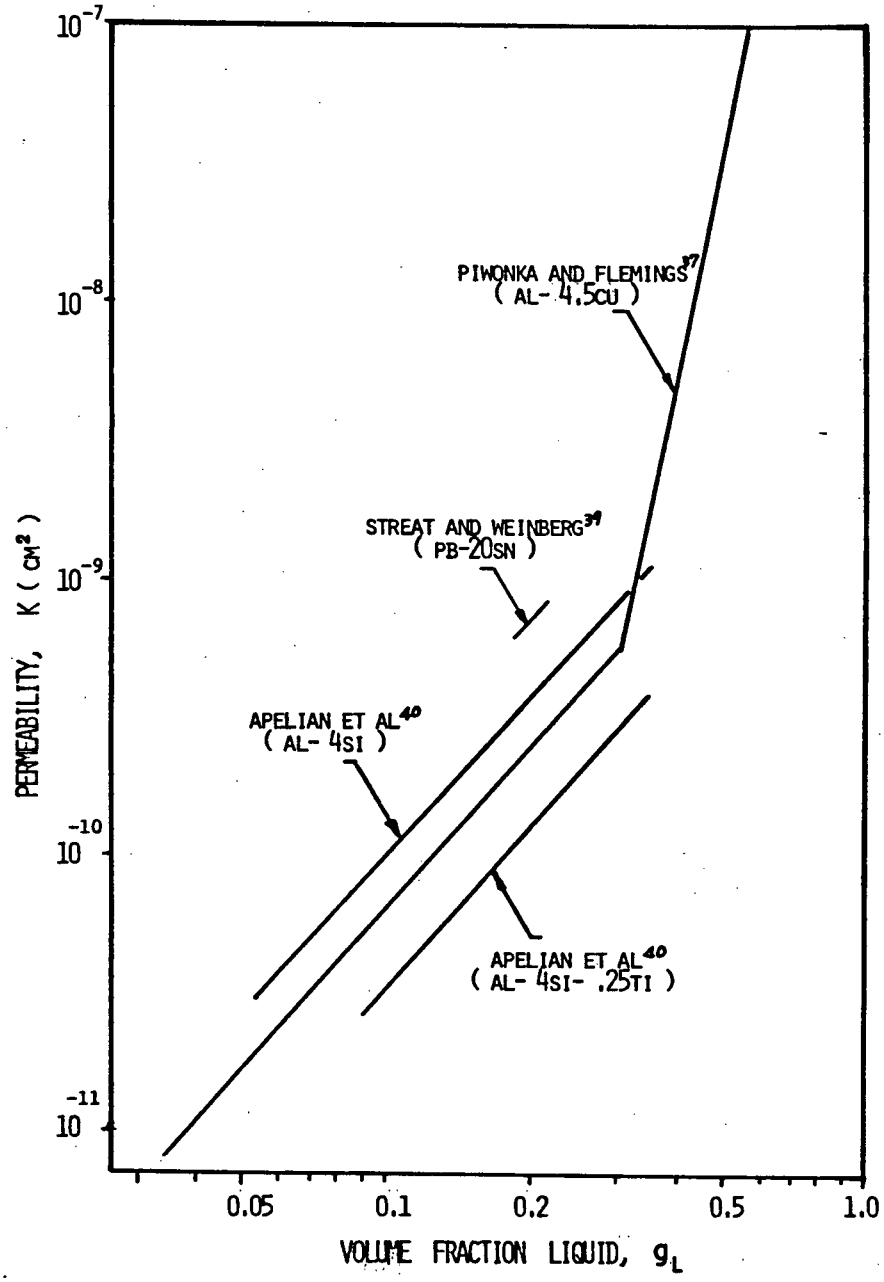

Figure 29 - Comparison of measured permeabilities vs volume fraction liquid

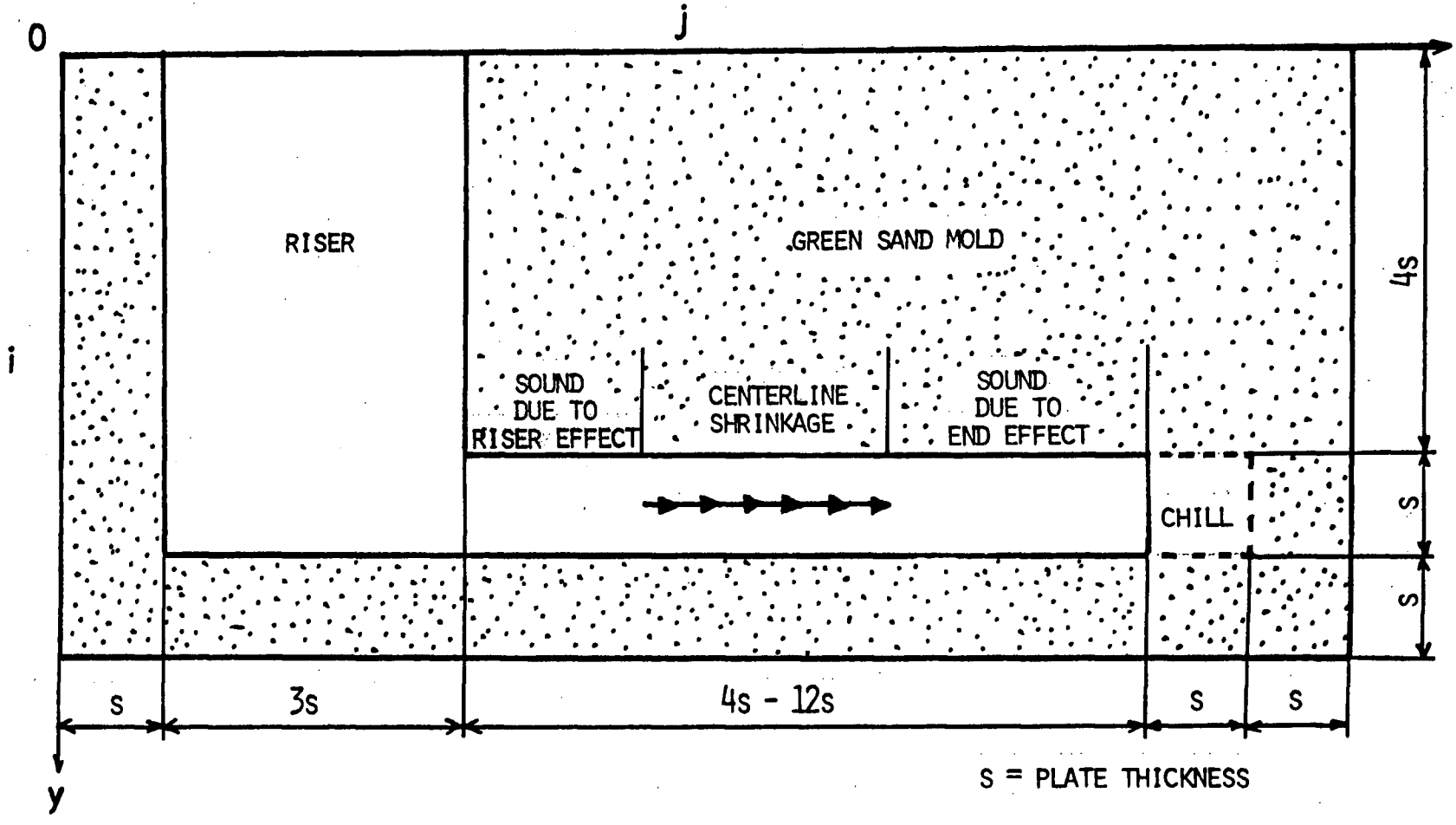

Figure 30 - Configuration of the system investigated

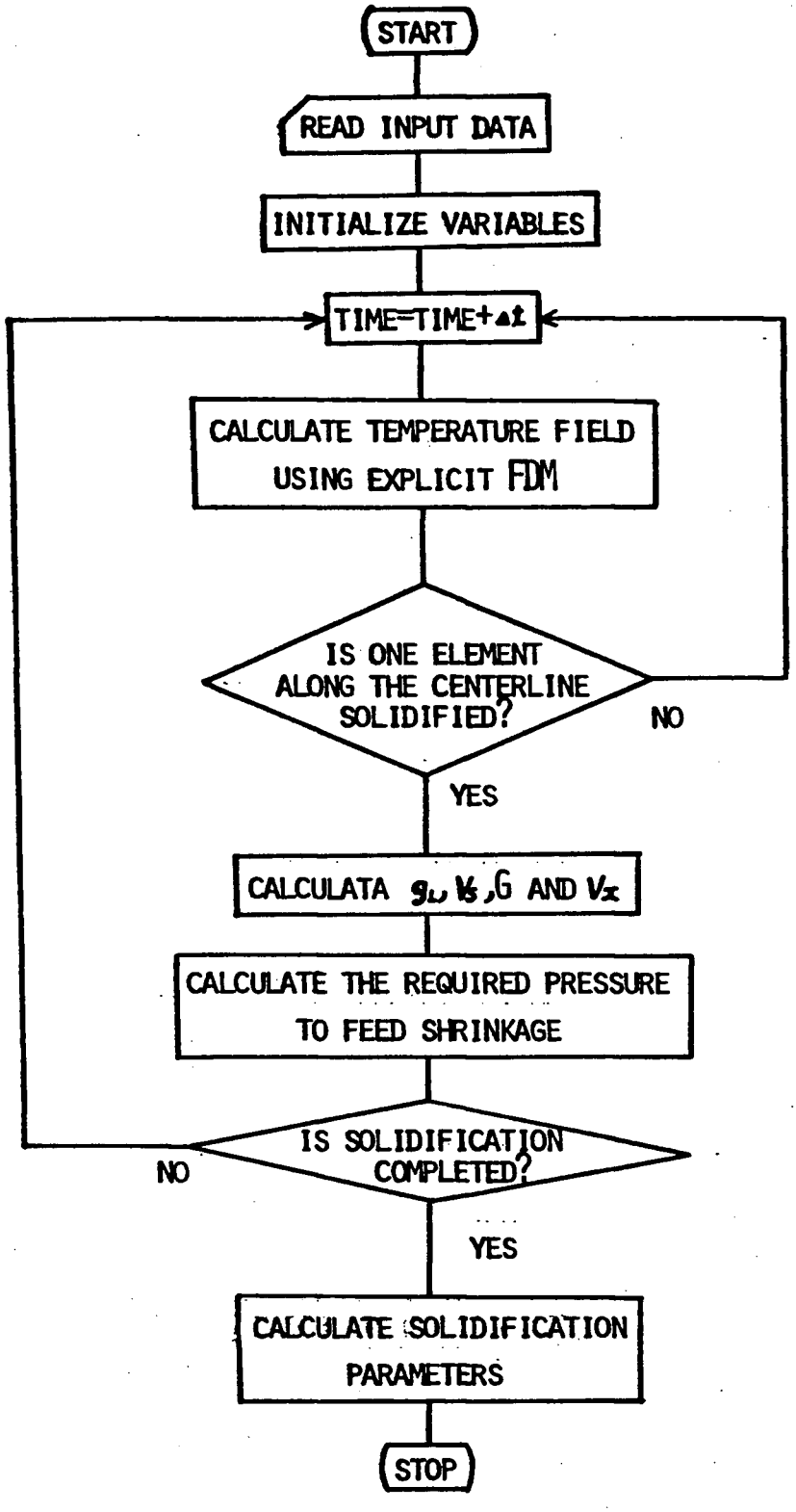

Figure 31 - Flow chart of the computer program for the prediction of centerline shrinkage

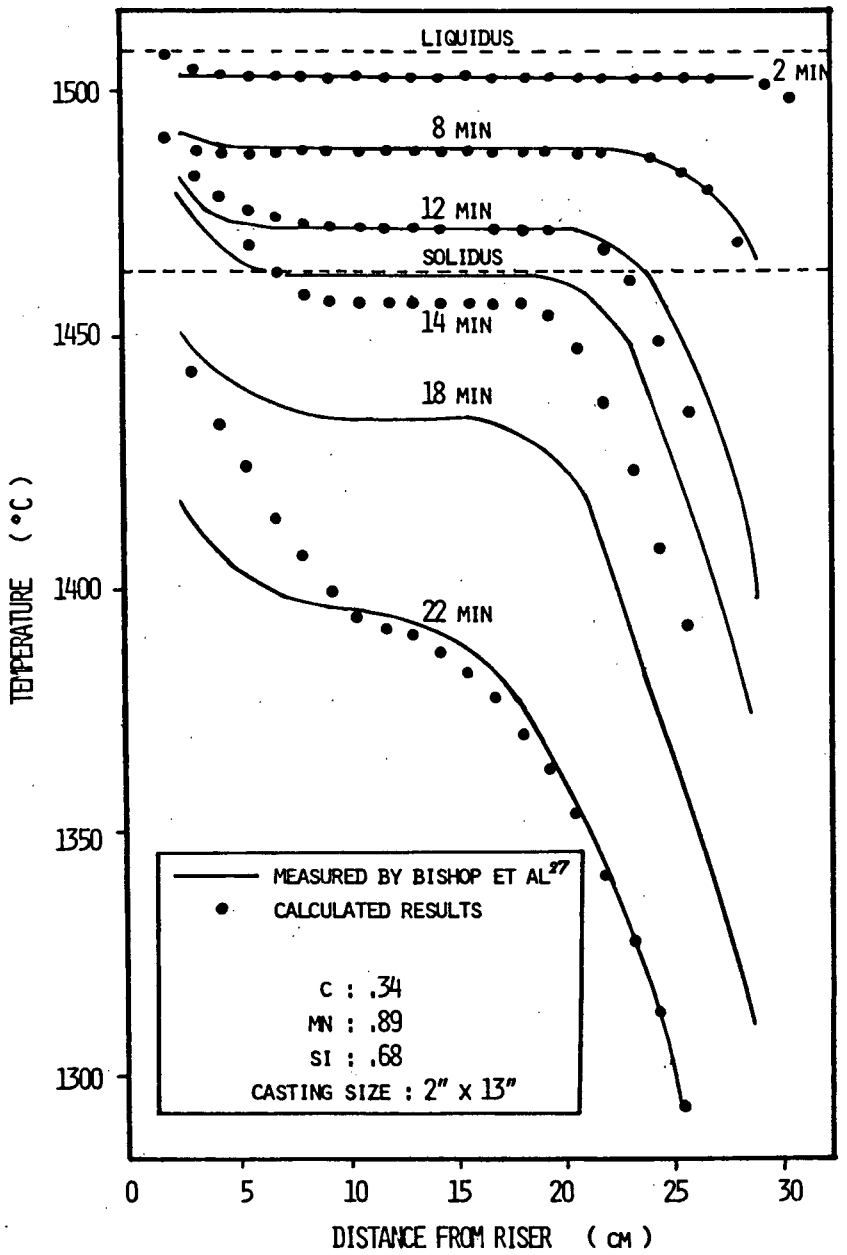

Figure 32 - Temperature distribution along the centerline of the plate casting

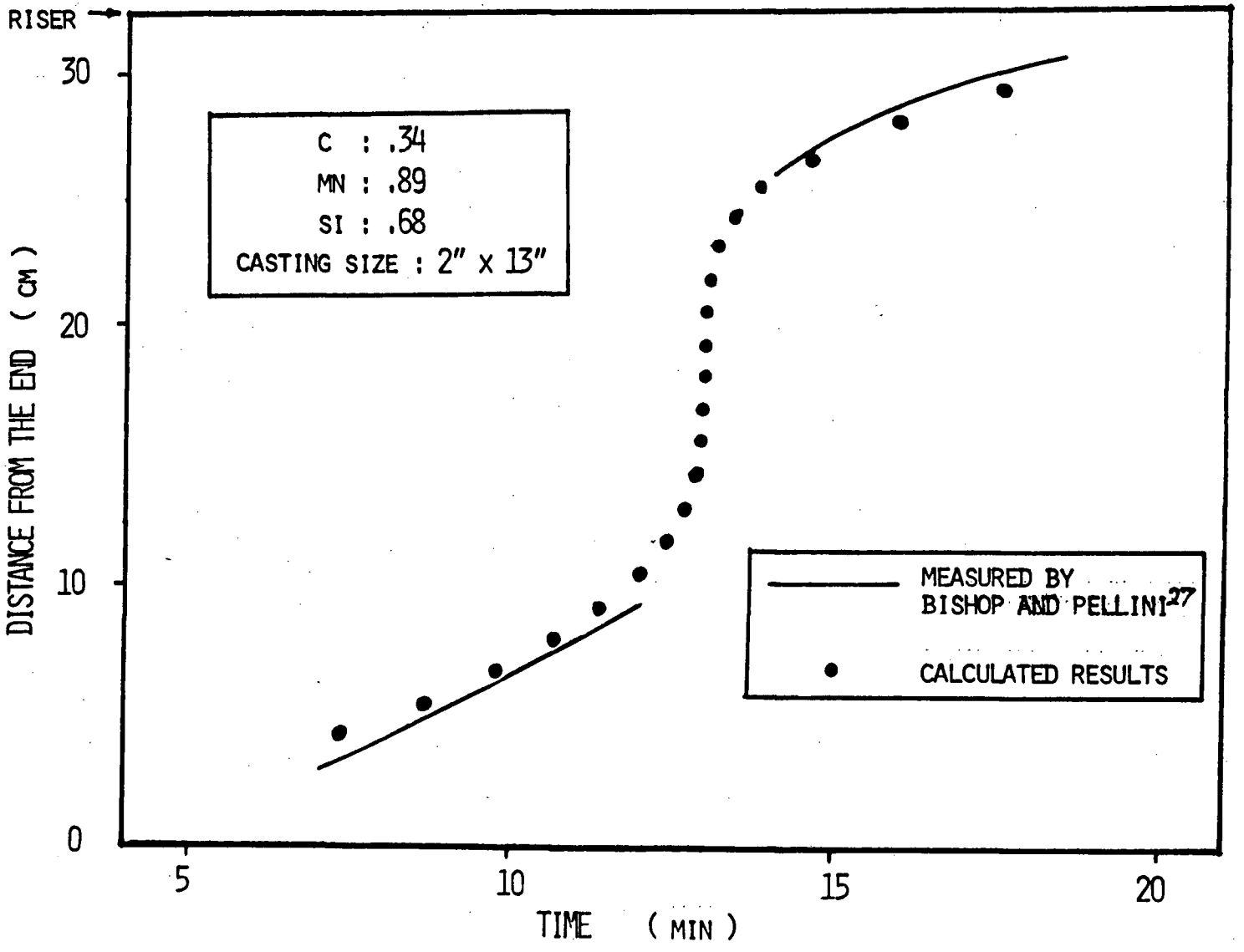

Figure 33 - Solidus movement along the centerline of plate casting

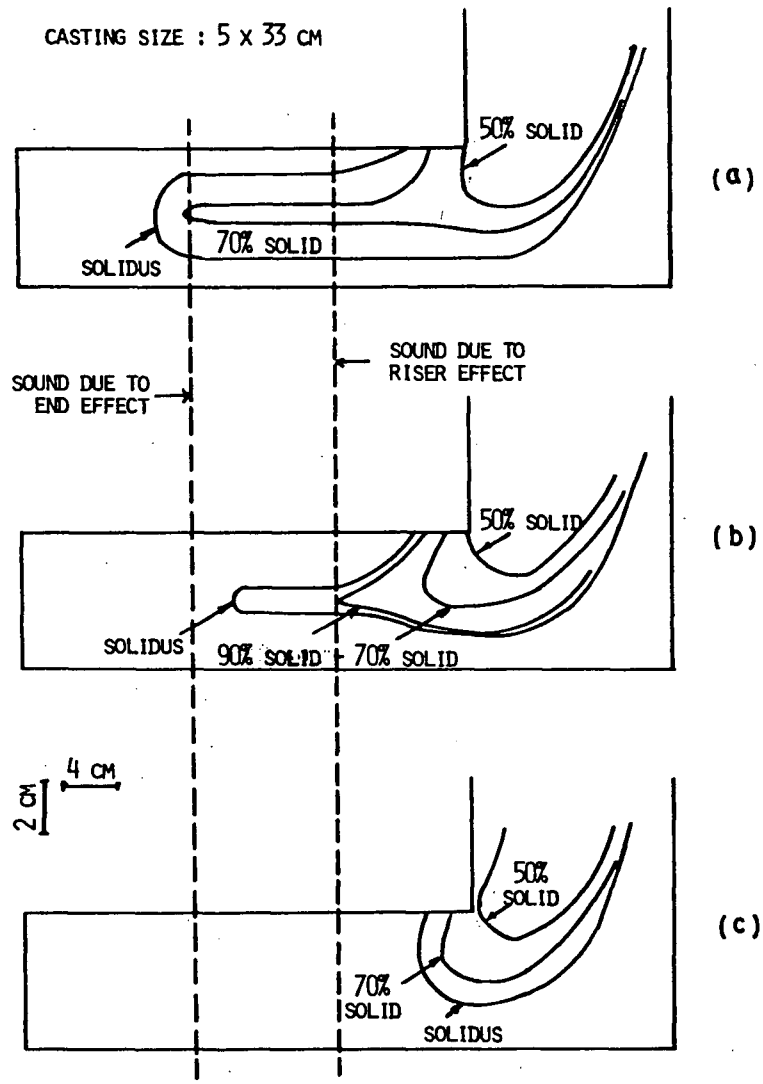

Figure 34 - The distribution of solidification contour lines at the (a)initial, (b) middle and (c) last stages of solidification

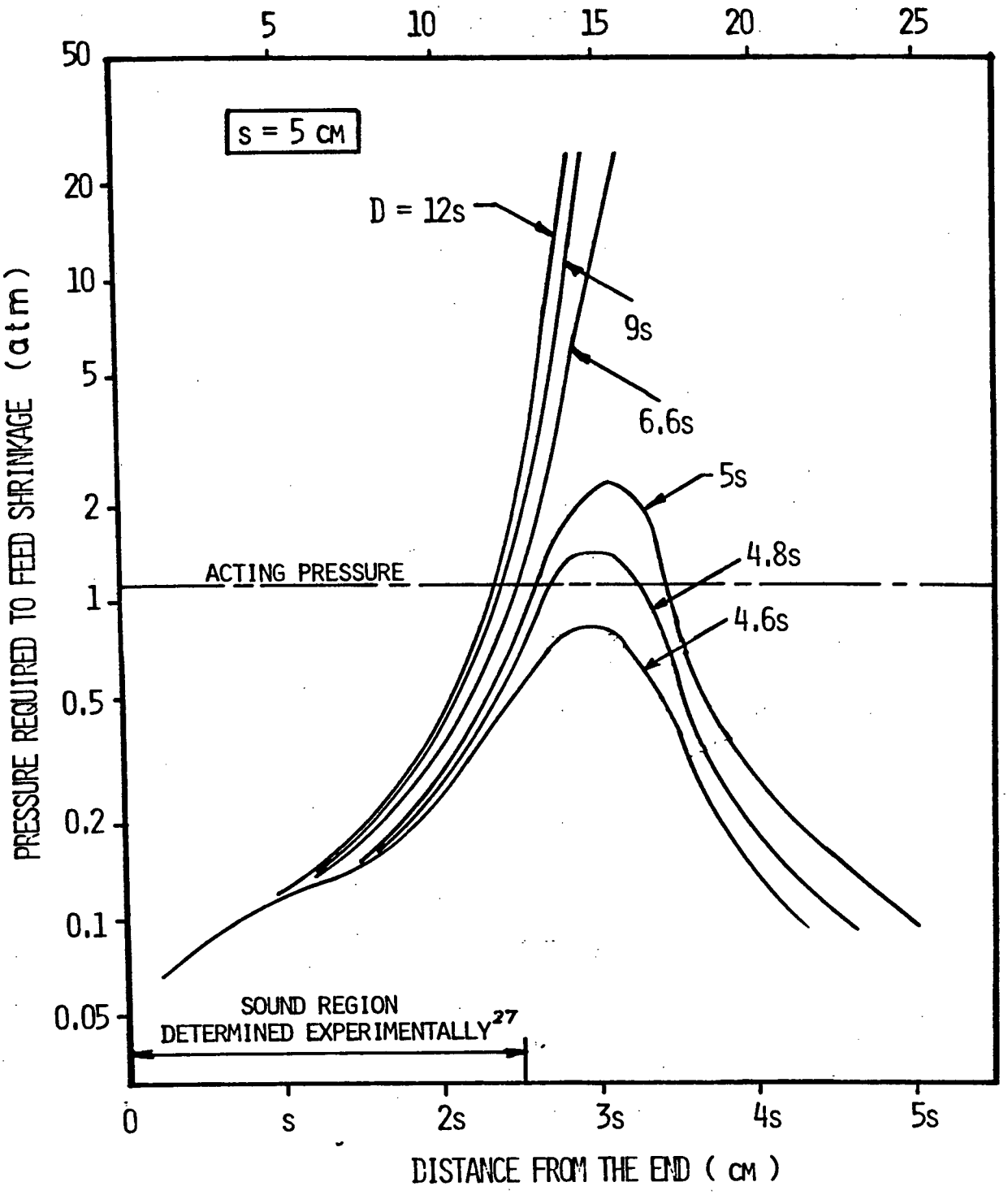

Figure 35 - Distribution of the pressure required to feed shrinkage at the end of solidification (s=5cm)

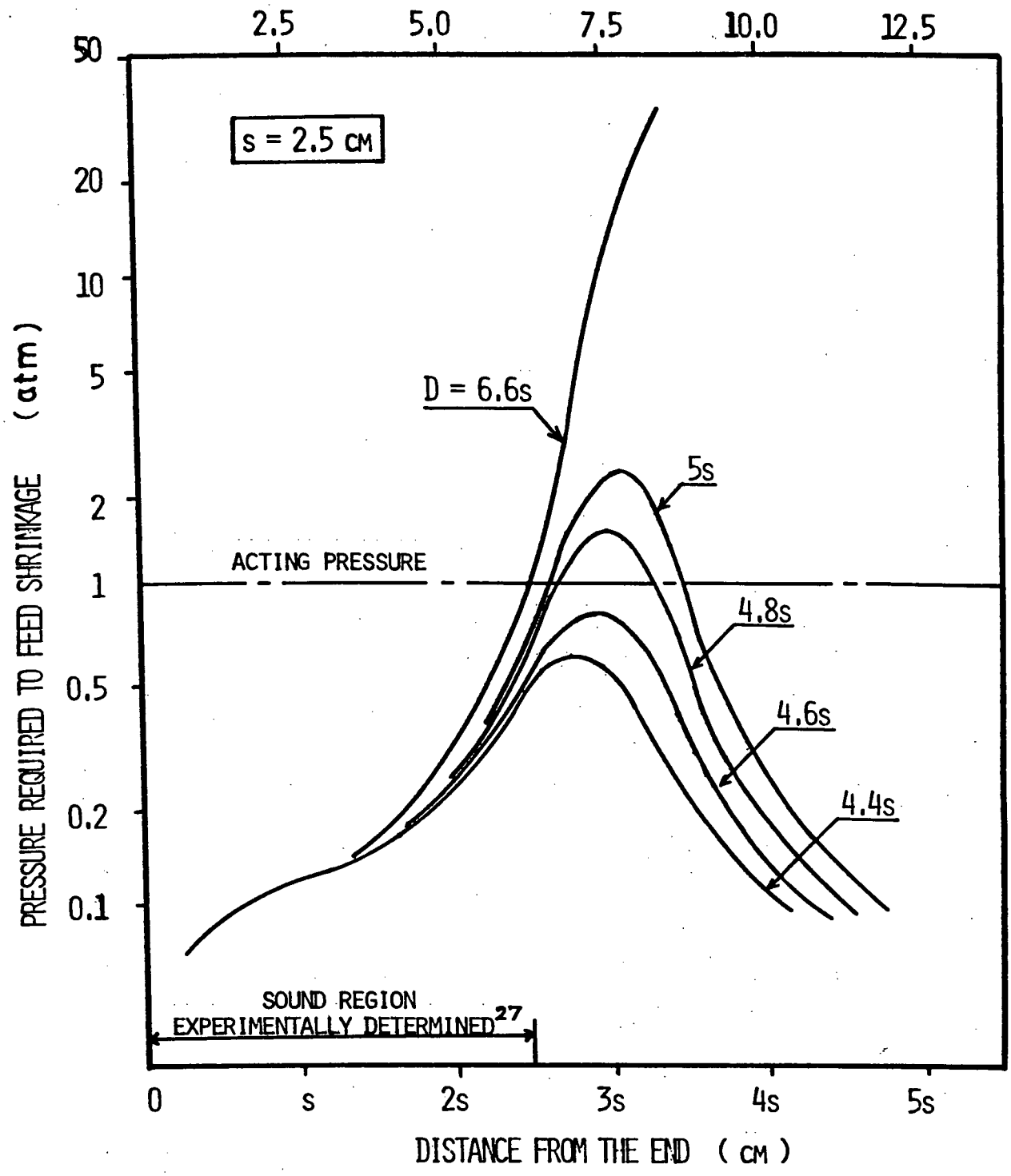

Figure 36 - Distribution of the pressure required to feed shrinkage at the end of solidification (s=2.5cm)

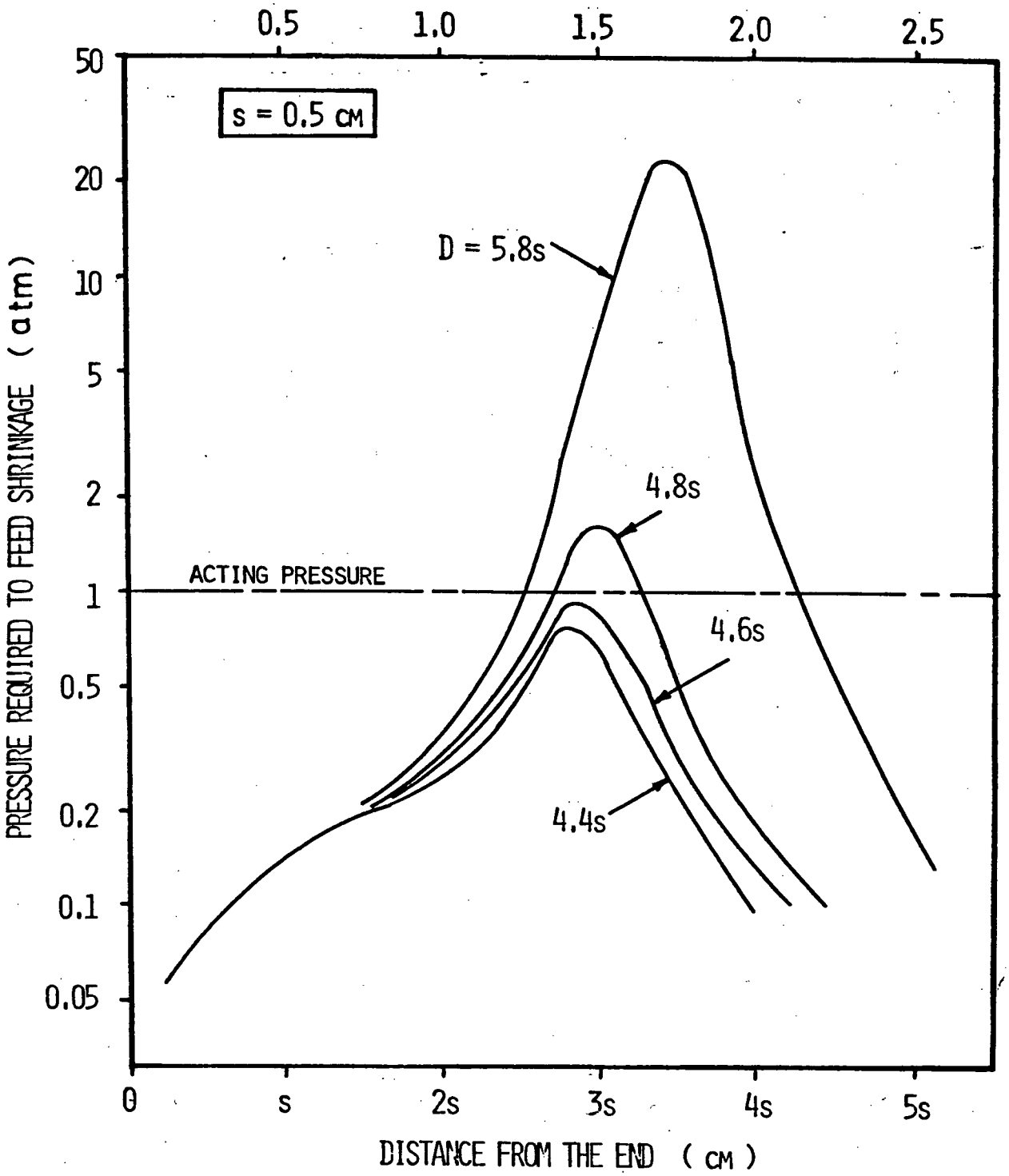

Figure 37 - Distribution of the pressure required to feed shrinkage at the end of solidification (s=0.5cm)

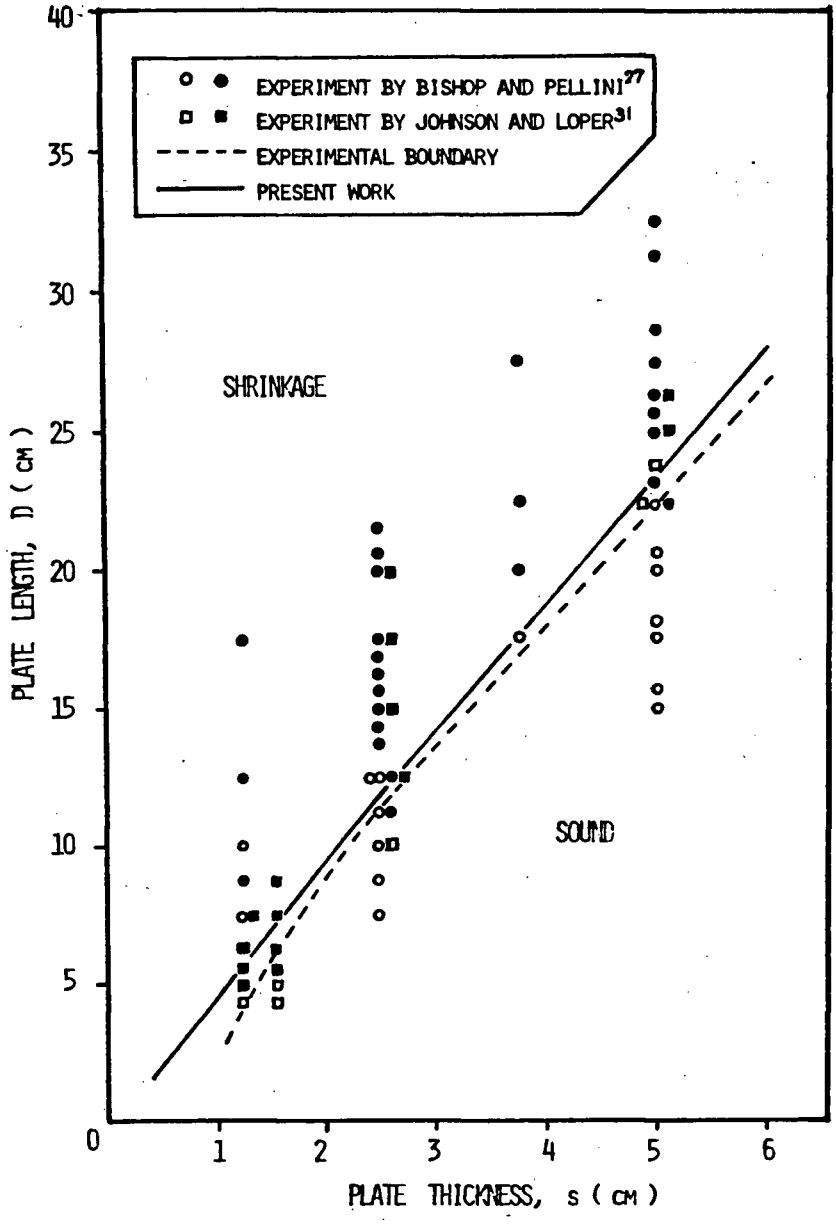

Figure 38 - Soundness of steel plate castings

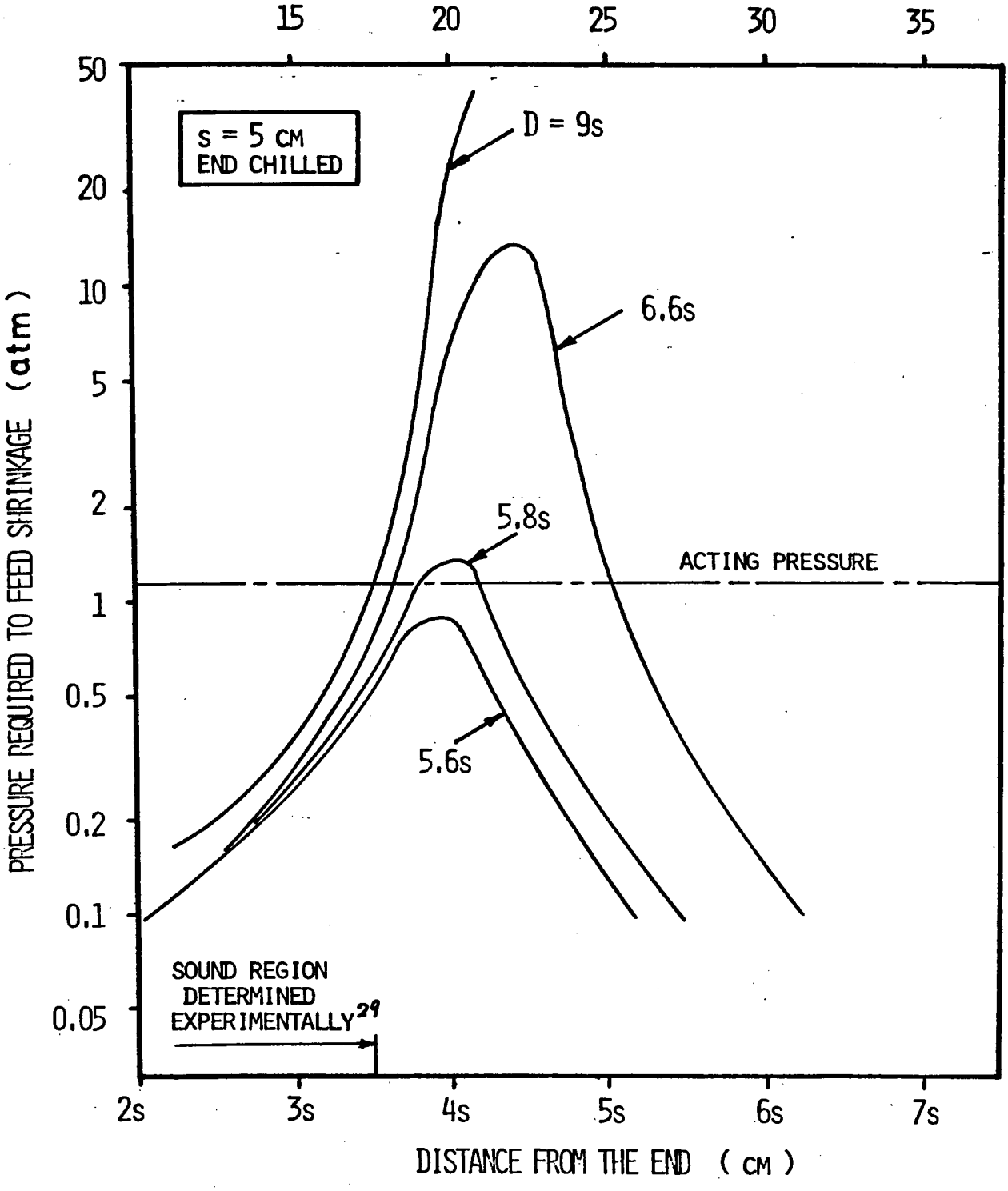

Figure 39 - Distribution of the pressure required to feed shrinkage at the end of solidification -end chilled casting

BIBLIOGRAPHY

1. E.Scheil; Metallforschung, 2 (1947), p69.

2. J.Kirkaldy and W.V.Youdelis; Trans. AIME, 212 (1958), p833.

3. F.Sauerwald; Metallwirschaft, 22 (1943), p543.

4. W.V.Youdelis and D.R.Colton; Trans. AIME, 218 (1960), p809.

5. W.V.Youdelis; "The Solidification of Metals" (Brighton Conference), The Iron and Steel Inst. London (1967), p112.

6. E.Plezel and Z.Schneider; Z. Metallkunde, 35 (1943), p121.

7. B.Prabhakar and F.Weinberg; Met. Trans. ASM, 9B (1978), p150.

8. M.C.Flemings and G.E.Nereo; Trans. AIME, 239 (1967), p1449.

9. M.C.Flemings, R.Mehrabian and G.E.Nereo; ibid, 242 (1968), p41.

10. M.C.Flemings and G.E.Nereo; ibid, 242 (1968), p50.

11. R.Mehrabian, M.A.Keane and M.C.Flemings; Met Trans. ASM, 1 (1970), p3238

12. E.Scheil; Z.Metallkunde, 34 (1942), p70.

13. W.G.Pfann; Trans. AIME, 194 (1952), p747.

14. H.D.Brody and M.C.Flemings; ibid, 236 (1966), p615.

15. T.F.Bower, H.D.Brody and M.C.Flemings; ibid, 236 (1966), p624.

16. C.J.Smithells; "Metals Reference Book" 4th Ed., Butterworths, London (1967), p685.

17. J.F.Elliot and M.Gleiser; "Thermochemistry of Steelmaking", Addison-Wesley Pub. Co. (1960).

18. K.Bornemann and F.Sauerwald; Z.Metallkunde, 14 (1922), p10.

19. K.Bornemann and F.Sauerwald; ibid, 14 (1922), p154.

20. H.R.Thresh, A.F.Crawley and D.W.G.White; Trans. AIME, 242 (1968), p819.

21. R.E.Morrone, J.O.Wilkes and R.D.Pehlke; AFS Cast Metals Research Journal, Dec (1970), p184.

22. R.E.Morrone, J.O.Wilkes and R.D.Pehlke; ibid, Dec (1970), p188.

23. G.Sciama; ibid, Mar (1972), p20.

24. G.Sciama; ibid, Dec (1972), p145

25. I.Ohnaka, Y.Yashima and T.Fukusako; Imono, 52 (1980), No 1, p10.

26. A.Jeyarajan and R.D.Pehlke; AFS Trans. 86 (1978), p457.

27. H.F.Bishop and W.S.Pellini; AFS Trans. 58 (1950), p185.

28. H.F.Bishop, E.T.Myskowski and W.S.Pellini; ibid, 59 (1951), p171.

29. E.T.Myskowski, H.F.Bishop and W.S.Pellini; ibid, 60 (1952), p389.

30. W.S.Pellini; ibid, 61 (1953), p61.

31. S.B.Johnson and C.R.Loper,Jr; ibid, 77 (1969), p360.

32. E.Niyama, T.Uchida, M.Morioka and S.Saito; AFS International Cast Metals Journal; 6 (1981), No.2, p16.

33. E.Niyama, T.Uchida, M.Morioka and S.Saito; ibid, 7 (1982), No.3, p52.

34. K.Chijiiwa and I.Imafuku; Imono, 55 (1983), No.5, p271.

35. V.L.Davies; AFS Cast Metals Research Journal, Jun (1975), p33.

36. M.C.Flemings; "Solidification Processing", McGraw-Hill Inc. (1974), p234.

37. T.S.Piwonka and M.C.Flemings; Trans. AIME, 236 (1966), p1157.

38. R.Mehrabian, M.Kreane and M.C.Flemings; Met. Trans. ASM, 1 (1970), p1209.

39. N.Streat and F.Weinberg; Met. Trans. ASM, 7B (1976), p417.

40. D.Apelian, M.C.Flemings and R.Mehrabian; Met. Trans.

ASM, 5 (1974), p2533.

APPENDIX A - RECALCULATION OF THE SCHEIL-YOUDELIS MODEL PREDICTIONS

The Scheil-Youdelis' model predictions have been recalculated for the Al-Cu, Al-Zn and Sb-Bi systems and are shown in Figs 40, 41 and 42, respectively. Calculations from this investigation plus calculations published and the experimental results reported are included. For the Al-Cu alloys Fig 40 the recalculated values are significantly lower than the curve published by Scheil and Kirkaldy et al[2], although the general shape of the curve is the same. It is not clear why the recalculated curve differs from the published one. In the Al-Zn and Sb-Bi alloys there are very large differences between the recalculated curves and those reported in the literature, in particular at the low alloy compositions.

APPENDIX B - DERIVATION OF NODAL EQUATIONS

The partial differential equation for two dimensional transient problem (equation (B-30)) and boundary equations (equations B-34 to B-36) were solved explicitly using finite difference method. Fig 43 shows types of nodes appearing in the model examined. The nodal difference equations were derived by applying heat balance for each element as followings;

Interior nodes (node type 10)

$$k\frac{T_{i,j-1}-T_{i,j}}{\Delta x}\Delta y + k\frac{T_{i,j+1}-T_{i,j}}{\Delta x}\Delta y + k\frac{T_{i-1,j}-T_{i,j}}{\Delta y}\Delta x + k\frac{T_{i+1,j}-T_{i,j}}{\Delta y}\Delta x = \Delta x\Delta y\rho C_p\frac{T^*_{i,j}-T_{i,j}}{\Delta t} \quad (1)$$

$$T^*_{i,j} = Fo_x(T_{i,j-1}+T_{i,j+1}) + Fo_y(T_{i-1,j}+T_{i+1,j}) + (1-2Fo_x-2Fo_y)T_{i,j} \quad (1)'$$

Corner node in the mold (node type 1)

$$T^*_{i,j} = 2Fo_xT_{i,j+1}+2Fo_yT_{i+1,j}+2(Fo_xBi_x+Fo_yBi_y)T_a + (1-2Fo_x-2Fo_y-2Fo_xBi_x-2Fo_yBi_y)T_{i,j} \quad (2)$$

Surface nodes in the mold (node type 2)

$$T^*_{i,j} = Fo_x(T_{i,j-1}+T_{i,j+1}) + 2Fo_yT_{i+1,j}+2Fo_yBi_yT_a + (1-2Fo_x-2Fo_y-2Fo_yBi_y)T_{i,j} \quad (3)$$

Boundary node in the mold (node type 4)

$$\frac{1}{\frac{\frac{1}{2}\Delta x}{k_S}+\frac{\frac{1}{2}\Delta x}{k_M}}(T_{i,j-1}-T_{i,j})\Delta y + k_S\frac{T_{i,j+1}-T_{i,j}}{\Delta x}\Delta y + k_S\frac{T_{i-1,j}-T_{i,j}}{\Delta y}\Delta x$$

$$+ k_S\frac{T_{i+1,j}-T_{i,j}}{\Delta y}\Delta x = \Delta x\Delta y\rho C_p\frac{T^*_{i,j}-T_{i,j}}{\Delta t} \qquad (4)$$

$$T^*_{i,j} = \frac{2k_M}{k_S+k_M}Fo_x T_{i,j-1} + Fo_x T_{i,j+1} + Fo_y(T_{i-1,j}+T_{i+1,j})$$

$$+ \left(1 - \frac{2k_M}{k_S+k_M}Fo_x - Fo_x - 2Fo_y\right)T_{i,j} \qquad (4)'$$

Surface boundary nodes in the metal (node type 6)

$$\frac{1}{\frac{\frac{1}{2}\Delta x}{k_S}+\frac{\frac{1}{2}\Delta x}{k_M}}(T_{i,j-1}-T_{i,j})\frac{\Delta y}{2} + k_M\frac{T_{i,j+1}-T_{i,j}}{\Delta x}\frac{\Delta y}{2} + h(T_a-T_{i,j})\Delta x$$

$$+ k_M\frac{T_{i+1,j}-T_{i,j}}{\Delta y}\Delta x = \Delta x\frac{\Delta y}{2}\rho C_p\frac{T^*_{i,j}-T_{i,j}}{\Delta t} \qquad (5)$$

$$T^*_{i,j} = \frac{2k_S}{k_S+k_M}Fo_x T_{i,j-1} + Fo_x T_{i,j+1} + 2Fo_y T_{i+1,j} + 2Fo_y Bi_y T_a$$

$$+ \left(1 - \frac{2k_S}{k_S+k_M}Fo_x - Fo_x - 2Fo_y - 2Fo_y Bi_y\right)T_{i,j} \qquad (5)'$$

Corner nodes in the metal (node type 9)

$$T^*_{i,j} = \frac{2k_S}{k_S+k_M}(Fo_x T_{i,j-1} + Fo_y T_{i+1,j}) + Fo_x T_{i,j+1} + Fo_y T_{i-1,j}$$

$$+ \left\{1 - \left(1 + \frac{2k_S}{k_S+k_M}\right)(Fo_x + Fo_y)\right\}T_{i,j} \qquad (6)$$

APPENDIX C - FORTRAN PROGRAM FOR THE PREDICTION OF CENTRELINE SHRINKAGE

```
C
C
C     ***************************************************************
C
C       FILE NAME : CENT091     CALC. OF SOLIDUS PRESSURE AT GL=
C
C          FEEDING DISTANCE DETERMINATION OF HORIZONTAL PLATE CA
C          MOLD BY NUMERICAL SIMULATION.(APPLICATION OF 1-D DARC
C          2-D UNSTEADY-STATE PROBLEM.
C          HANDLING OF LATENT HEAT = EQUIVALLENT SPECIFIC HEAT M
C
C          ASSUMPTIONS; 1)CONST.SPECIFIC HEAT,CONDUCTIVITY Δ DEN
C                       2)LINEAR SOLIDUS Δ LIQUIDUS
C                       3)NO H.T.RESISTANCE AT S/M INTERFACE
C                       4)THE MOLD IS INSTANTANEOUSLY FILLED WIT
C                         METAL WHICH IS STAGNANT
C          SYMBOLS; DX =GRID DISTANCE          DY =GRID DISTANCE
C                   DT =TIME STEP              H  =HEAT TRANSF.COE
C                   TA =AMBIENT TEMP.          TO =INITIAL TEMP.OF
C                   TP =POURING TEMP.          N  =NO.OF NODES(Y)
C                   M  =NO.OF NODES(X)         OTI=OUTPUT TIME INT
C                   OT =OUTPUT TIME            CPM=SPECIFIC HEAT O
C                   CPS=SPECIFIC HEAT OF SAN   DM =DENSITY OF META
C                   DS =DENSITY OF SAND        KM =CONDUCTIVITY OF
C                   KS =CONDUCTIVITY OF SAND   TL =LIQUIDUS TEMP.
C                   TS =SOLIDUS TEMP.          HS =LATENT HEAT OF
C                   TM =TIME                   TMS=SOLIDN.START TI
C                   TM7=70% SOLIDN.TIME        TM9=90% SOLIDN. TIM
C                   TMF=SOLIDN.COMPLETE TIME   TMLS=LOCAL SOLIDN.T
C                   CR =MEAN COOLING RATE      GR =TEMP.GRADIENT
C                   P  =SOLIDN.PARAMETER
C                   AM,AS  =THERMAL DIFFUSIVITY
C                   FMX,FMY=FOURIER NO.OF METAL
C                   FSX,FSY=FOURIER NO.OF SAND
C                   BSX,BSY=BIOT NO IN SAND
C                   DDX,DDY=1/DX**2,1/DY**2
C                   A1,A2  =2*(KS,KM)/(KS+KM)
C                   CPME   =EQUIVALLENT SPECIFIC HEAT OF METAL
C                   T,TB   =NEW Δ OLD TEMP.
C                   VSX=SOLIDUS VELOCITY       VX =FLUID VELOCITY
C                   VXI,VXO=IN- Δ OUT-FLOW VELOCITY
C                   GL,GLB =NEW Δ OLD VOLUME FRACTION LIQUID
C                   TA =ATOM. PRESSURE         AK =PERMEABILITY
C                   DP =PRESSURE DROP          PR =PRESSURE AT SOL
C                   B  =CONTRACTION RATIO
C
C     ***************************************************************
C
C
      REAL KM,KS
      DIMENSION T(100,100),TB(100,100),AM(100,100),FMX(100,100),
```

```
     1CP(100,100),TMS(100,100),PRR(100,100),
     2TM98(100,100),            GR(100,100),P(100,100),
     3FMY(100,100),TMF(100,100),VSX(100,100),VX(100,100),
     4GL(100,100),GLB(100,100),DP(100,100),PR(100,100)
C
C
C      ***** DATA INPUT
       READ(5,1000) N,LC,DX,DY,DT,OTI
 1000  FORMAT(//,2I12,4F12.5)
       READ(5,1020) CPM,DM,KM,HS,B
       READ(5,1020) TL,TS,TP,TA,TO
 1020  FORMAT(/,5F12.5)
       READ(5,1030) CPS,DS,KS,H1,E,VIS
 1030  FORMAT(/,6F12.5)
C
       M=25+LC
       MM5=M-5
       MM6=M-6
C
C      ***** DETERMINATION OF INITIAL VALUES
       DO 20 J=1,M
       DO 10 I=1,N
    10 TB(I,J)=TO
    20 CONTINUE
C
       DO 40 J=6,20
       DO 30 I=1,25
       GLB(I,J)=1.0
    30 TB(I,J)=TP
    40 CONTINUE
C
       DO 60 J=21,MM5
       DO 50 I=21,25
       GLB(I,J)=1.0
    50 TB(I,J)=TP
    60 CONTINUE
C
       TM=0.0
       OT=OTI
       JF=MM6
C
C      ***** ITERATION START
    70 TM=TM+DT/60.0
C
C      ***** CHECK OF SPECIFIC HEAT OF METAL
       CALL CPCHK(MM5,TB,TL,TS,CP,CPM,CPME,HS)
C
C      ***** CALCULATION OF CONSTANTS
       DDX=1/(DX**2)
       DDY=1/(DY**2)
       A1=2.0*KM/(KS+KM)
       A2=2.0*KS/(KS+KM)
C
       DO 130 J=6,20
```

```
      DO 120 I=1,25
      AM(I,J)=KM/(DM*CP(I,J))
      FMX(I,J)=AM(I,J)*DT*DDX
  120 FMY(I,J)=AM(I,J)*DT*DDY
  130 CONTINUE
C
      DO 150 J=21,MM5
      DO 140 I=21,25
      AM(I,J)=KM/(DM*CP(I,J))
      FMX(I,J)=AM(I,J)*DT*DDX
  140 FMY(I,J)=AM(I,J)*DT*DDY
  150 CONTINUE
C
      AS=KS/(DS*CPS)
      FSX=AS*DT*DDX
      FSY=AS*DT*DDY
      BSX=H1*DX/KS
      BSY=H1*DY/KS
      PA=1.013E+06
      G=981.0
C
C
C     ***** CALCULATION OF T'S AT TIME=TM
      CALL TCALC(N,M,T,TB,TA,FSX,FSY,FMX,FMY,BSX,BSY,E,DY,KM,A1,A
C
C     ***** CALCULATION OF SOLIDIFICATION TIMES
      CALL TMSOL(TL,TS,MM5,T,TB,TM,TMS,        TM98,TMF)
C
C     ***** CALC. OF FLUID VELOCITY
C     IF(JF.LT.21) GO TO 235
      I=23
      DO 165 J=21,JF
      IF(T(I,J).GT.TL) GO TO 155
      IF(T(I,J).LT.TS) GO TO 160
      FS=(TL-T(I,J))/(TL-TS)
      GL(I,J)=((1.0-FS)/7.1)/(FS/7.5+(1.0-FS)/7.1)
      GO TO 165
  155 GL(I,J)=1.0
      GO TO 165
  160 GL(I,J)=0.0
  165 CONTINUE
C
C
  185 IF(GL(23,JF).GT.0.02) GO TO 228
      DO 190 L=1,30
      IF((TM98(23,JF)-TM98(23,JF+L)).LE.0.0) GO TO 190
      VSX(23,JF)=DX*L/  ((TM98(23,JF)-TM98(23,JF+L))*60.0)
      GO TO 195
  190 CONTINUE
C
  195 VX(23,JF)=B*VSX(23,JF)
      IF(JF.LE.21) GO TO 220
      DO 200 L=1,50
      VX(23,JF-L)=VX(23,JF)*GLB(23,JF)/GLB(23,JF-L)
```

```
      IF((JF-L).EQ.21) GO TO 220
  200 CONTINUE
C
C     ***** APPLICATION OF DARCY'S LAW
  220 DPTX=0.0
      I=23
      IF(GL(I,21).LE.0.02) GO TO 235
      DO 225 J=21,JF
       IF(GLB(I,J).GT.0.3) GO TO 222
       AK=6.89E-09*GLB(I,J)**2
       GO TO 223
  222  AK=1.0E-05*GLB(I,J)**8
  223  DP(I,J)=VIS*GLB(I,J)      *VX(I,J)*DX/AK
       DPTX=DPTX+DP(I,J)
  225 CONTINUE
C
      PR(23,JF)=DPTX
      PRR(23,JF)=PR(23,JF)/PA
      WRITE(6,1032) JF,TM
 1032 FORMAT(//,'(23,',I2,') IS SOLIDIFIED AT',F10.5,' (MIN)',/)
      WRITE(6,1033) (T(23,J),J=21,MM5)
 1033 FORMAT(20F6.0)
      WRITE(6,1034)
 1034 FORMAT(/,'NO',5X,'T',7X,'GL',9X,'Vf',7X,'P.DROP')
      WRITE(6,1035)
 1035 FORMAT(7X,'C',16X,'cm/sec',5X,'dyn/cm2',/)
      WRITE(6,1036) (J,T(23,J),GLB(23,J),VX(23,J),DP(23,J),J=21,J
 1036 FORMAT(I2,F2.1,F3.4,F11.5,E12.4)
      WRITE(6,1040) PRR(23,JF)
 1040 FORMAT(/,5X,'PRESSURE REQUIRED =',F11.4,'  atm',//)
C     WRITE(6,1032) JF,TM
C1032 FORMAT(//,'(23,',I2,') IS SOLIDIFIED AT',F10.5,' (MIN)',/)
C     WRITE(6,1034) (VX(23,J),J=21,JF)
C1034 FORMAT(10E10.3,'  cm/sec')
C     WRITE(6,1036) (DP(23,J),J=21,JF)
C1036 FORMAT(10E10.3,'  dyn/cm2')
C     WRITE(6,1038)       DPTX,PR(23,JF)
C1038 FORMAT(/,5X, E12.4,'   PRESSURE =',E12.4,' (dyn/cm2)')
C
      JF=JF-1
      IF(JF.LT.21) GO TO 235
C
      IF(GL(23,JF).LE.0.02) GO TO 185

C
  228 I=23
      DO 229 J=21,JF
  229 GLB(I,J)=GL(I,J)
C
C     ***** CALCULATION OF TEMP.GRADIENTS
  235 CALL TGR(MM5,T,TB,TS,DX,DY,GR)
C
C     ***** CHECK OF COMPLETE SOLIDIFICATION
      IF(T(23,21).GT.TS) GO TO 239
```

```
C
C      ***** SOLIDN. PARAMETERS
       I=23
       DO 237 J=21,MM6
       TMLS      =TMF(I,J)-TMS(I,J)
       CR      =(TL-TS)/(TMLS      *60.0)
  237  P(I,J)=GR(I,J)/SQRT(CR)
C
C      ***** OUTPUT OF T'S  AT COMPLETE SOLIDIFICATION
       WRITE(6,1050) TM
 1050  FORMAT(////,'TEMP DISTRIBUTION AT',F10.4,'  MIN ',//)
       WRITE(6,1080) ((T(I,J),I=16,N),J=1,M)
 1080  FORMAT(15F5.0)
C
       WRITE(6,1170)
 1170  FORMAT(////,'COMPLETE SOLIDN. TIME : TMF (MIN)',//)
       WRITE(6,1180) ((TMF(I,J),I=21,25),J=21,MM5)
 1180  FORMAT(5F10.3)
C
       WRITE(6,1190)
 1190  FORMAT(////,'NO',6X,'T.GRAD',8X,'P',7X,'V(SOLID.M)',2X,
      1'PRESSURE',7X,'PR/PA',
      2/,9X,'C/cm',19X,'cm/sec',5X,'dyn/cm',9X,'atm',/)
       I=23
       WRITE(6,1200) (J,GR(I,J),P(I,J),VSX(I,J),PR(I,J),PRR(I,J),
      1J=21,MM6)
 1200  FORMAT(I2,3F12.4,E12.3,F12.4)
C
C
       STOP
C
C
C      ***** OUTPUT TIME CHECK DURING ITERATION
  239  IF(TM.LT.OT) GO TO 240
C
C      ***** OUTPUT OF T'S
       WRITE(6,1245) TM
 1245  FORMAT(////,'TEMP. DISTRIBUTION AT',F10.4,'MIN ',//)
       WRITE(6,1246) ((T(I,J),I=16,N),J=1,M)
 1246  FORMAT(15F5.0)
C
       OT=OT+OTI
C
C
C      ***** SUBSTITUTION OF TEMP. Δ ITERATION
  240  DO 260 J=1,M
       DO 250 I=1,N
  250  TB(I,J)=T(I,J)
  260  CONTINUE
C
       GO TO 70
C
       END
C
```

```
C
C
C
C
C       ************************************************************
C
      SUBROUTINE CPCHK(MM5,TB,TL,TS,CP,CPM,CPME,HS)
C
C        ASSIGN THE EQUIVALLENT SPECIFIC HEAT TO METAL IN THE RAN
C
C       ************************************************************
C
C
      DIMENSION TB(100,100),CP(100,100)
C
C     TLS=(TL+TS)/2.0
      DO 30 J=6,20
      DO 20 I=1,25
      IF(TB(I,J).GT.TL.OR.TB(I,J).LT.TS) GO TO 10
C     IF(TB(I,J).GT.TLS) GO TO 5
C     CP(I,J)=CPM+(TB(I,J)-TS)*(4.0*HS/(TL-TS)**2)
C     GO TO 20
C   5 CP(I,J)=CPM+(TL-TB(I,J))*(4.0*HS/(TL-TS)**2)
    5 CP(I,J)=CPM+HS/(TL-TS)
      GO TO 20
   10 CP(I,J)=CPM
   20 CONTINUE
   30 CONTINUE
C
      DO 60 J=21,MM5
      DO 50 I=21,25
      IF(TB(I,J).GT.TL.OR.TB(I,J).LT.TS) GO TO 40
C     IF(TB(I,J).GT.TLS) GO TO 35
C     CP(I,J)=CPM+(TB(I,J)-TS)*(4.0*HS/(TL-TS)**2)
C     GO TO 50
C  35 CP(I,J)=CPM+(TL-TB(I,J))*(4.0*HS/(TL-TS)**2)
   35 CP(I,J)=CPM+HS/(TL-TS)
      GO TO 50
   40 CP(I,J)=CPM
   50 CONTINUE
   60 CONTINUE
C
      RETURN
      END
C
C
C
C
C
C     ************************************************************
C
      SUBROUTINE TCALC(N,M,T,TB,TA,FSX,FSY,FMX,FMY,BSX,BSY,E,DY,K
     1A1,A2)
C
```

```
C         CALCULATION NODES' TEMPS. BY EXPLICIT FINITE DIFFERENCE
C
C     ************************************************************
C
C
      REAL KM
      DIMENSION T(100,100),TB(100,100),FMX(100,100),FMY(100,100)
      MM1=M-1
      MM2=M-2
      MM3=M-3
      MM4=M-4
      MM5=M-5
      MM6=M-6
C
C     ***** TEMPS. IN SAND
C
C    NODE 1
      DO 15 J=2,4
      DO 10 I=2,26
   10 T(I,J)=FSX*(TB(I,J-1)+TB(I,J+1))+FSY*(TB(I-1,J)+TB(I+1,J))
     1       +(1.0-2.0*FSX-2.0*FSY)*TB(I,J)
   15 CONTINUE
C
      I=26
      J=5
   20 T(I,J)=FSX*(TB(I,J-1)+TB(I,J+1))+FSY*(TB(I-1,J)+TB(I+1,J))
     1       +(1.0-2.0*FSX-2.0*FSY)*TB(I,J)
C
      DO 40 I=27,29
      DO 30 J=2,MM1
   30 T(I,J)=FSX*(TB(I,J-1)+TB(I,J+1))+FSY*(TB(I-1,J)+TB(I+1,J))
     1       +(1.0-2.0*FSX-2.0*FSY)*TB(I,J)
   40 CONTINUE
C
      DO 45 I=2,19
      DO 42 J=22,MM1
   42 T(I,J)=FSX*(TB(I,J-1)+TB(I,J+1))+FSY*(TB(I-1,J)+TB(I+1,J))
     1       +(1.0-2.0*FSX-2.0*FSY)*TB(I,J)
   45 CONTINUE
C
      I=20
      J=MM4
   50 T(I,J)=FSX*(TB(I,J-1)+TB(I,J+1))+FSY*(TB(I-1,J)+TB(I+1,J))
     1       +(1.0-2.0*FSX-2.0*FSY)*TB(I,J)
C
      I=26
      J=MM4
   55 T(I,J)=FSX*(TB(I,J-1)+TB(I,J+1))+FSY*(TB(I-1,J)+TB(I+1,J))
     1       +(1.0-2.0*FSX-2.0*FSY)*TB(I,J)
C
      DO 70 I=20,26
      DO 60 J=MM3,MM1
   60 T(I,J)=FSX*(TB(I,J-1)+TB(I,J+1))+FSY*(TB(I-1,J)+TB(I+1,J))
     1       +(1.0-2.0*FSX-2.0*FSY)*TB(I,J)
```

```
   70 CONTINUE
C
C     NODE 2
       I=1
       J=1
  100 T(I,J)=FSX*TB(I,J+1)+FSY*TB(I+1,J)+(FSX*BSX+FSY*BSY)*TA
     1       +(1.0-FSX-FSY-FSX*BSX-FSY*BSY)*TB(I,J)
C
C     NODE 3
                I=1
       DO 110 J=2,4
  110 T(I,J)=FSX*(TB(I,J-1)+TB(I,J+1))+FSY*TB(I+1,J)+FSY*BSY*TA
     1       +(1.0-2.0*FSX-FSY-FSY*BSY)*TB(I,J)
C
                I=1
       DO 115 J=22,MM1
  115 T(I,J)=FSX*(TB(I,J-1)+TB(I,J+1))+FSY*TB(I+1,J)+FSY*BSY*TA
     1       +(1.0-2.0*FSX-FSY-FSY*BSY)*TB(I,J)
C
C     NODE 4
       I=1
       J=5
  120 T(I,J)=FSX*TB(I,J-1)+FSY*TB(I+1,J)+A1*FSX*TB(I,J+1)+FSY*BSY
     1       +(1.0-FSX-FSY-A1*FSX-FSY*BSY)*TB(I,J)
C
C     NODE 5
       I=1
       J=21
  125 T(I,J)=FSX*TB(I,J+1)+FSY*TB(I+1,J)+A1*FSX*TB(I,J-1)+FSY*BSY
     1       +(1.0-FSX-FSY-A1*FSX-FSY*BSY)*TB(I,J)
C
C     NODE 6
       I=1
       J=M
  128 T(I,J)=FSX*TB(I,J-1)+FSY*TB(I+1,J)+(FSX*BSX+FSY*BSY)*TA
     1       +(1.0-FSX-FSY-FSX*BSX-FSY*BSY)*TB(I,J)
C
C     NODE 7
                J=1
       DO 130 I=2,29
  130 T(I,J)=FSY*(TB(I-1,J)+TB(I+1,J))+FSX*TB(I,J+1)+FSX*BSX*TA
     1       +(1.0-FSX-2.0*FSY-FSX*BSX)*TB(I,J)
C
C     NODE 8
                J=5
       DO 180 I=2,25
  180 T(I,J)=FSY*(TB(I-1,J)+TB(I+1,J))+FSX*TB(I,J-1)+A1*FSX*TB(I,
     1       +(1.0-2.0*FSY-FSX-A1*FSX)*TB(I,J)
C
C     NODE 9
                J=21
       DO 185 I=2,19
  185 T(I,J)=FSY*(TB(I-1,J)+TB(I+1,J))+FSX*TB(I,J+1)+A1*FSX*TB(I,
     1       +(1.0-2.0*FSY-FSX-A1*FSX)*TB(I,J)
```

```
C
            J=MM4
      DO 187 I=21,25
  187 T(I,J)=FSY*(TB(I-1,J)+TB(I+1,J))+FSX*TB(I,J+1)+A1*FSX*TB(I,
     1        +(1.0-2.0*FSY-FSX-A1*FSX)*TB(I,J)
C
C     NODE 10
            J=M
      DO 190 I=2,29
  190 T(I,J)=FSY*(TB(I-1,J)+TB(I+1,J))+FSX*TB(I,J-1)+FSX*BSX*TA
     1        +(1.0-FSX-2.0*FSY-FSX*BSX)*TB(I,J)
C
C     NODE 11
      I=20
      J=21
  220 T(I,J)=FSX*TB(I,J+1)+FSY*TB(I-1,J)+A1*FSX*TB(I,J-1)
     1    +A1*FSY*TB(I+1,J)+(1.0-FSX-FSY-A1*(FSX+FSY))*TB(I,J)
C
C     NODE 12
            I=20
      DO 225 J=22,MM5
  225 T(I,J)=FSX*(TB(I,J-1)+TB(I,J+1))+FSY*TB(I-1,J)+A1*FSY*TB(I+
     1        +(1.0-2.0*FSX-FSY-A1*FSY)*TB(I,J)
C
C     NODE 13
            I=26
      DO 230 J=6,MM5
  230 T(I,J)=FSX*(TB(I,J-1)+TB(I,J+1))+FSY*TB(I+1,J)+A1*FSY*TB(I-
     1        +(1.0-2.0*FSX-FSY-A1*FSY)*TB(I,J)
C
C     NODE 14
      I=30
      J=1
  240 T(I,J)=FSX*TB(I,J+1)+FSY*TB(I-1,J)+(FSX*BSX+FSY*BSY)*TA
     1        +(1.0-FSX-FSY-FSX*BSX-FSY*BSY)*TB(I,J)
C
C     NODE 15
            I=30
      DO 250 J=2,MM1
  250 T(I,J)=FSX*(TB(I,J-1)+TB(I,J+1))+FSY*TB(I-1,J)+FSY*BSY*TA
     1        +(1.0-2.0*FSX-FSY-FSY*BSY)*TB(I,J)
C
C     NODE 16
      I=30
      J=M
  260 T(I,J)=FSX*TB(I,J-1)+FSY*TB(I-1,J)+(FSX*BSX+FSY*BSY)*TA
     1        +(1.0-FSX-FSY-FSX*BSX-FSY*BSY)*TB(I,J)
C
C
C      ***** TEMPS. IN METAL
C
C     NODE 17
      DO 280 I=2,24
      DO 270 J=7,19
```

```
  270 T(I,J)=FMX(I,J)*(TB(I,J-1)+TB(I,J+1))+FMY(I,J)*(TB(I-1,J)
     1     +TB(I+1,J))+(1.0-2.0*FMX(I,J)-2.0*FMY(I,J))*TB(I,J)
  280 CONTINUE
C
      I=21
      J=20
  290 T(I,J)=FMX(I,J)*(TB(I,J-1)+TB(I,J+1))+FMY(I,J)*(TB(I-1,J)
     1     +TB(I+1,J))+(1.0-2.0*FMX(I,J)-2.0*FMY(I,J))*TB(I,J)
C
      DO 310 I=22,24
      DO 300 J=20,MM5
  300 T(I,J)=FMX(I,J)*(TB(I,J-1)+TB(I,J+1))+FMY(I,J)*(TB(I-1,J)+T
     1     (I+1,J))+(1.0-2.0*FMX(I,J)-2.0*FMY(I,J))*TB(I,J)
  310 CONTINUE
C
C     NODE 18
      I=1
      J=6
      H=1.37E-12*E*((TB(I,J)+273.0)**4-(TA+273.0)**4)/(TB(I,J)-TA
      BMY=H*DY/KM
  320 T(I,J)=FMX(I,J)*TB(I,J+1)+FMY(I,J)*TB(I+1,J)+A2*FMX(I,J)*TB
     1     (I,J-1)+FMY(I,J)*BMY*TA+(1.0-FMX(I,J)-FMY(I,J)-A2*FMX(I
     2     -BMY*FMY(I,J))*TB(I,J)
C
C     NODE 19
            I=1
      DO 330 J=7,19
      H=1.37E-12*E*((TB(I,J)+273.0)**4-(TA+273.0)**4)/(TB(I,J)-TA
      BMY=H*DY/KM
  330 T(I,J)=FMX(I,J)*(TB(I,J-1)+TB(I,J+1))+FMY(I,J)*TB(I+1,J)
     1        +BMY*FMY(I,J)*TA
     2        +(1.0-2.0*FMX(I,J)-(1.0+BMY)*FMY(I,J))*TB(I,J)
C
C     NODE 20
      I=1
      J=20
      H=1.37E-12*E*((TB(I,J)+273.0)**4-(TA+273.0)**4)/(TB(I,J)-TA
      BMY=H*DY/KM
  340 T(I,J)=FMX(I,J)*TB(I,J-1)+FMY(I,J)*TB(I+1,J)+A2*FMX(I,J)*TB
     1     (I,J+1)+FMY(I,J)*BMY*TA+(1.0-FMX(I,J)-FMY(I,J)-A2*FMX(I
     2     -BMY*FMY(I,J))*TB(I,J)
C
C     NODE 21
           J=6
      DO 350 I=2,24
  350 T(I,J)=FMX(I,J)*TB(I,J+1)+FMY(I,J)*(TB(I-1,J)+TB(I+1,J))
     1        +A2*FMX(I,J)*TB(I,J-1)
     2        +(1.0-2.0*FMY(I,J)-(1.0+A2)*FMX(I,J))*TB(I,J)
C
C     NODE 22
           J=20
      DO 355 I=2,20
  355 T(I,J)=FMX(I,J)*TB(I,J-1)+FMY(I,J)*(TB(I-1,J)+TB(I+1,J))
     1        +A2*FMX(I,J)*TB(I,J+1)
```

```
     2        +(1.0-2.0*FMY(I,J)-(1.0+A2)*FMX(I,J))*TB(I,J)
C
           J=MM5
      DO 360 I=22,24
  360 T(I,J)=FMX(I,J)*TB(I,J-1)+FMY(I,J)*(TB(I-1,J)+TB(I+1,J))
     1        +A2*FMX(I,J)*TB(I,J+1)
     2        +(1.0-2.0*FMY(I,J)-(1.0+A2)*FMX(I,J))*TB(I,J)
C
C    NODE 23
           I=21
      DO 370 J=21,MM6
  370 T(I,J)=FMY(I,J)*TB(I+1,J)+FMX(I,J)*(TB(I,J-1)+TB(I,J+1))
     1        +A2*FMY(I,J)*TB(I-1,J)
     2        +(1.0-2.0*FMX(I,J)-(1.0+A2)*FMY(I,J))*TB(I,J)
C
C    NODE 24
      I=21
      J=MM5
  380 T(I,J)=FMX(I,J)*TB(I,J-1)+FMY(I,J)*TB(I+1,J)
     1        +A2*FMX(I,J)*TB(I,J+1)+A2*FMY(I,J)*TB(I-1,J)
     2        +(1.0-(1.0+A2)*(FMX(I,J)+FMY(I,J)))*TB(I,J)
C
C    NODE 25
      I=25
      J=6
  390 T(I,J)=FMX(I,J)*TB(I,J+1)+FMY(I,J)*TB(I-1,J)
     1        +A2*FMX(I,J)*TB(I,J-1)+A2*FMY(I,J)*TB(I+1,J)
     2        +(1.0-(1.0+A2)*(FMX(I,J)+FMY(I,J)))*TB(I,J)
C
C    NODE 26
           I=25
      DO 400 J=7,MM6
  400 T(I,J)=FMX(I,J)*(TB(I,J-1)+TB(I,J+1))+FMY(I,J)*TB(I-1,J)
     1        +A2*FMY(I,J)*TB(I+1,J)
     2        +(1.0-2.0*FMX(I,J)-(1.0+A2)*FMY(I,J))*TB(I,J)
C
C    NODE 27
      I=25
      J=MM5
  410 T(I,J)=FMX(I,J)*TB(I,J-1)+FMY(I,J)*TB(I-1,J)
     1        +A2*FMX(I,J)*TB(I,J+1)+A2*FMY(I,J)*TB(I+1,J)
     2        +(1.0-(1.0+A2)*(FMX(I,J)+FMY(I,J)))*TB(I,J)
C
      RETURN
      END
C
C
C
C
C     ************************************************************
C
      SUBROUTINE TMSOL(TL,TS,MM5,T,TB,TM,TMS,          TM98,TMF)
C
C        CALCULATION OF SOLIDN. TIMES
```

```
C        SYMBOLS : TMS=START  AT TL      TM7=70%       AT T7
C                  TM9=90%    AT T9      TMF=COMPLETE  AT TS
C                  TM95=95%   AT T95     TM98=98%     AT T98
C                  TM99=99%   AT T99
C
C     ***************************************************************
C
C
      DIMENSION T(100,100),TB(100,100),TMS(100,100),
     1          TMF(100,100),TM98(100,100)
C
      T98=TL-0.98*(TL-TS)
C
      DO 60 J=21,MM5
      DO 50 I=21,25
C
      IF(T(I,J).GT.TL.OR.TB(I,J).LE.TL) GO TO 34
      TMS(I,J)=TM
   34 IF(T(I,J).GT.T98.OR.TB(I,J).LE.T98) GO TO 40
      TM98(I,J)=TM
   40 IF(T(I,J).GT.TS.OR.TB(I,J).LE.TS) GO TO 50
      TMF(I,J)=TM
   50 CONTINUE
   60 CONTINUE
C
      RETURN
      END
C
C
C
C
C     ***************************************************************
C
      SUBROUTINE TGR(MM5,T,TB,TS,DX,DY,GR)
C
C        CALC. OF TEMP. GRADIENTS(GR) AT THE END OF SOLIDN.
C        GR IS DEFINED AS THE MAXIMUM POSITIVE VALUE AMONG THE GR
C        FROM THE CENTER NODE TO THE 8 SURROUNDING NODES.
C
C     ***************************************************************
C
C
      DIMENSION T(100,100),TB(100,100),GR(100,100)
C
      DO 20 J=21,MM5
      DO 10 I=22,24
C
      IF(T(I,J).GT.TS.OR.TB(I,J).LE.TS) GO TO 10
      G1      =(T(I-1,J-1)-T(I,J))/SQRT(DX**2+DY**2)
      G2      =(T(I,J-1)-T(I,J))/DX
      G3      =(T(I+1,J-1)-T(I,J))/SQRT(DX**2+DY**2)
      G4      =(T(I-1,J)-T(I,J))/DY
      G5      =(T(I+1,J)-T(I,J))/DY
      G6      =(T(I-1,J+1)-T(I,J))/SQRT(DX**2+DY**2)
```

```
      G7      =(T(I,J+1)-T(I,J))/DX
      G8      =(T(I+1,J+1)-T(I,J))/SQRT(DX**2+DY**2)
    5 GR(I,J)=AMAX1(G1,G2,G3,G4,G5,G6,G7,G8)
   10 CONTINUE
   20 CONTINUE
C
      RETURN
      END
```

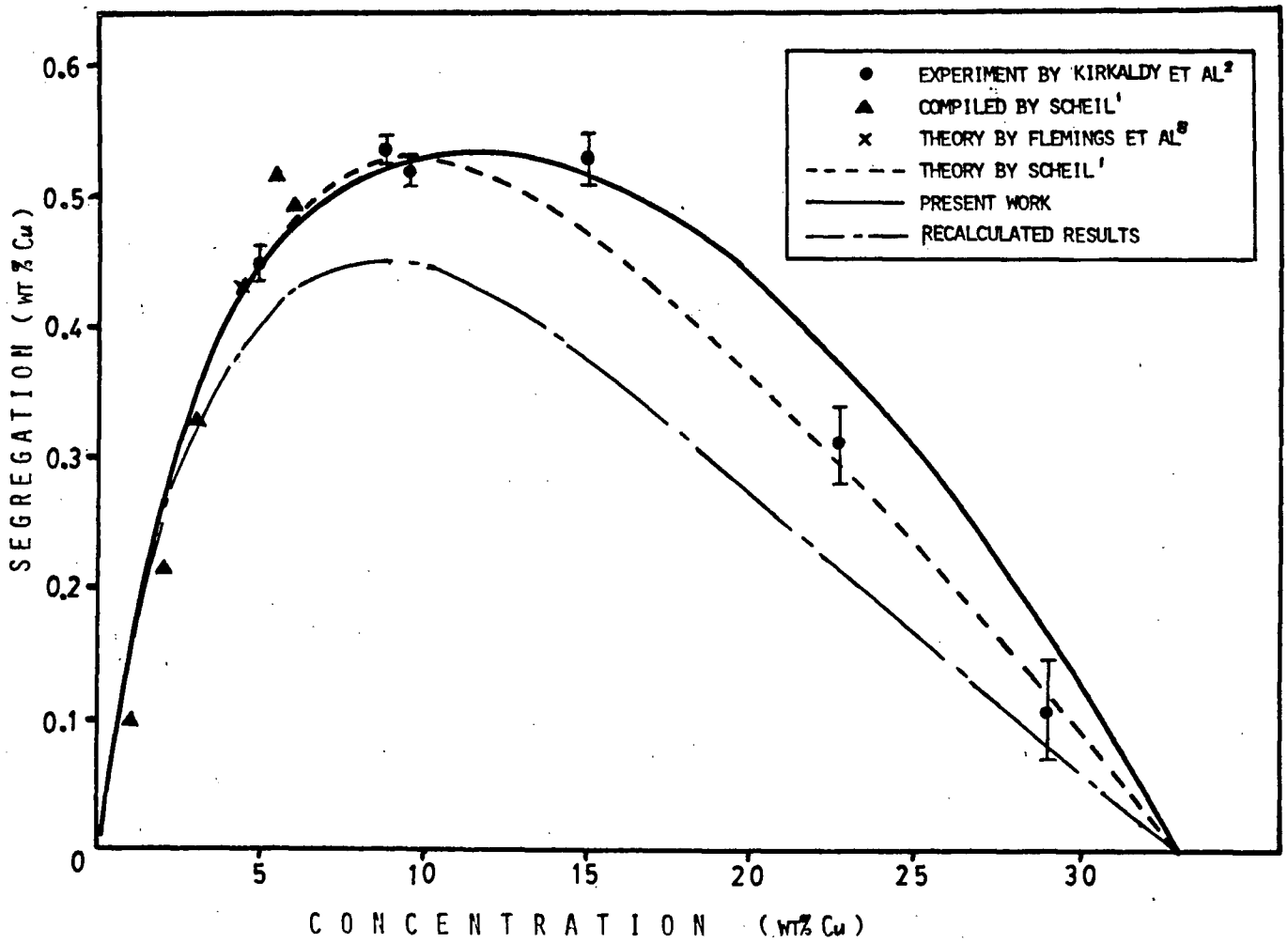

Figure 40 - Comparison of the inverse segregation at the chill face for the Al-Cu alloys

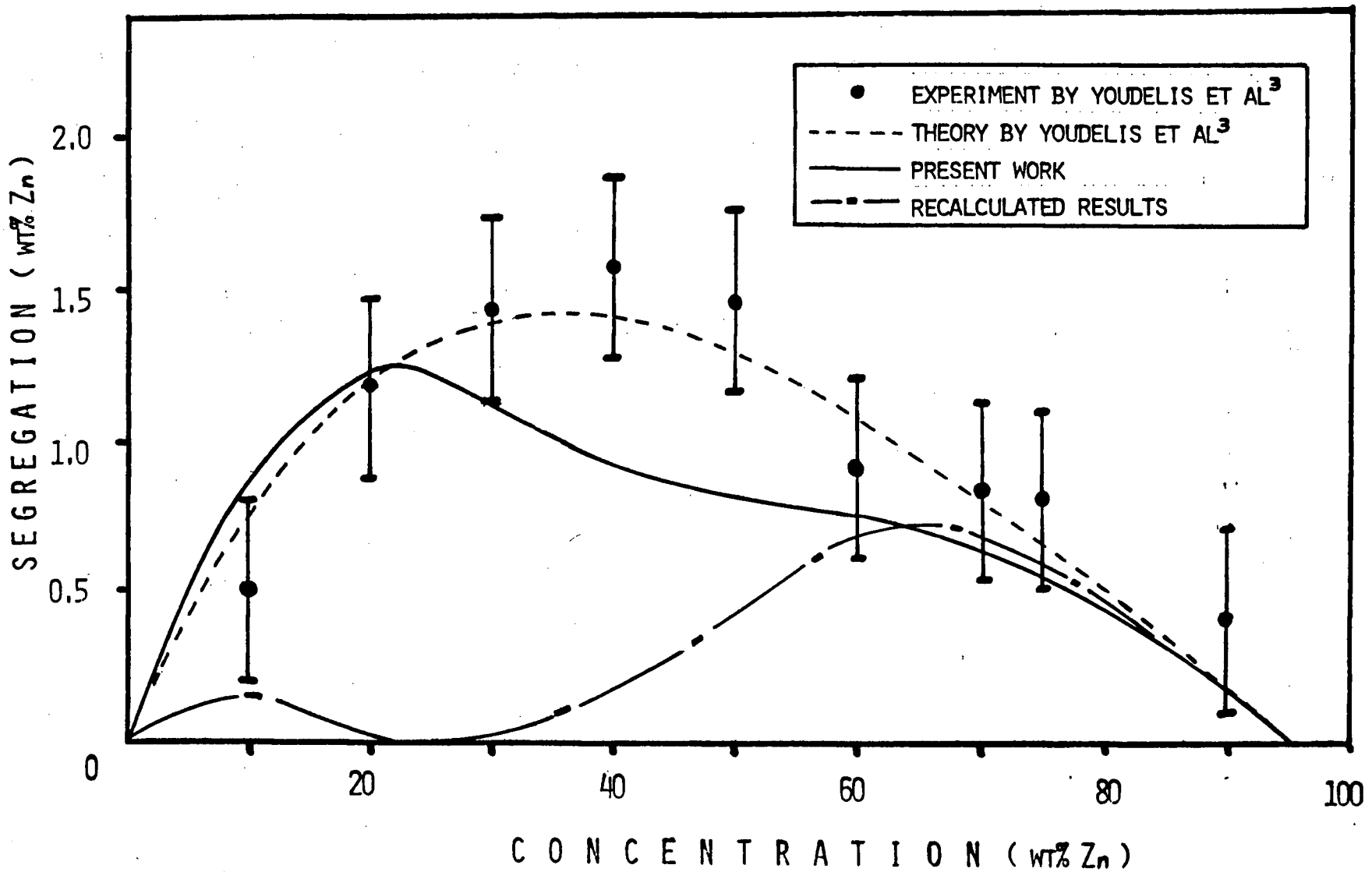

Figure 41 - Comparison of the inverse segregation at the chill face for the Al-Zn alloys

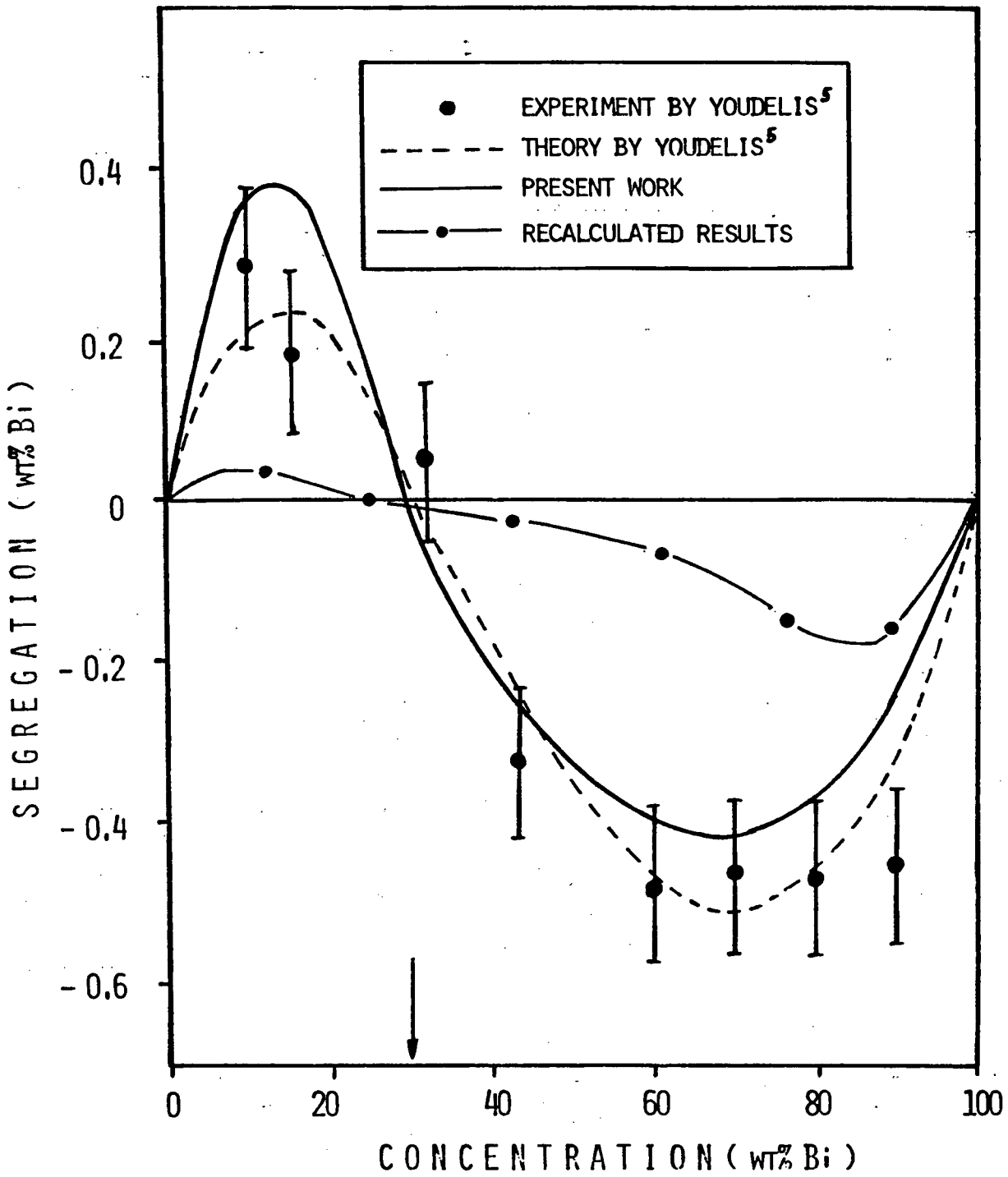

Figure 42 - Comparison of the inverse segregation at the chill face for the Sb-Bi alloys

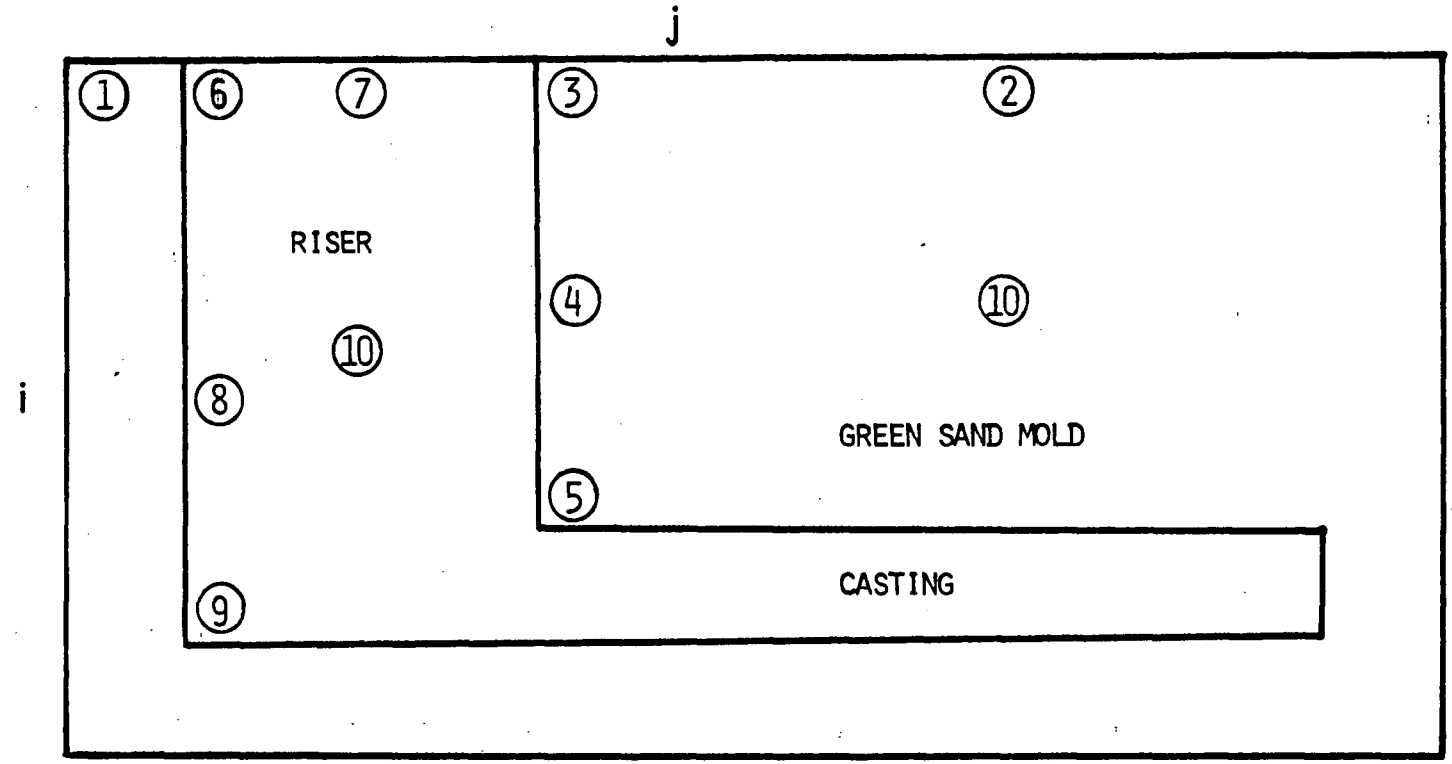

Figure 43 - Different types of nodes in the model investigated